

DESIGN AND FABRICATION OF SELF-PACKAGED, FLEXIBLE MEMS
ACCELEROMETER AND ALUMINUM NITRIDE TACTILE SENSORS

By

Md Sohel Mahmood

Presented to the Faculty of the Graduate School of
The University of Texas at Arlington in Partial Fulfillment
of the Requirements
for the Degree of

DOCTOR OF PHILOSOPHY

THE UNIVERSITY OF TEXAS AT ARLINGTON

April 2018

Copyright © by Md Sohel Mahmood, 2018

All Rights Reserved

Acknowledgements

First and foremost, I would like to thank my advisor Dr. Zeynep Celik-Butler, distinguished university professor of the department of electrical engineering of University of Texas at Arlington, for her continuous support throughout my graduate life. Her guidance has helped me to understand and carryout my research projects. Whenever I was stuck in any problem related to design, fabrication or characterization of the devices, her clear direction led me towards the best possible solution. I am also grateful to her for the unconditional help towards writing this dissertation.

I would like to thank my PhD proposal committee member Dr. Donald P. Butler for sharing his insights at several stages of my flexible MEMS accelerometer project. I would like to thank my other committee members Dr. Michael Vasilyev, Dr. Dereje Agonafer, Dr. Weidong Zhou, Dr. Yuze Sun and Dr. Sameer Iqbal for their valuable time and effort to review my research work.

I am also obliged to several Nanotechnology Research Center staff including manager of the facility Dr. Nader Hozhabri, Dennis Bueno, Richard K. Chambers and Huan Nguyen. I appreciate their time and effort for providing training on clean room equipment. I also express my gratitude to my fellow colleagues Dr. Moinuddin Ahmed, Dr. Yi Li, Dr. Sajeeb Rayhan, Sk Rubayiat Tousif and Ashfiqul Hamid for extending their helping hands at several stages of my PhD life.

I am eternally indebted to my parents, late A. K. M. Ziaul Haider and Roushan Ara Begum and my beloved wife Samia Jannat for their inspiration and prayer. Thanks to my brother Md Sakib Mahmood and other family members for their prayer too. Without their support, it would never be possible to complete my PhD endeavor.

April 13, 2018

Abstract

DESIGN AND FABRICATION OF SELF-PACKAGED, FLEXIBLE MEMS ACCELEROMETER AND ALUMINUM NITRIDE TACTILE SENSORS

Md Sohel Mahmood, PhD

The University of Texas at Arlington, 2018

Supervising professor: Dr. Zeynep Celik-Butler

The work presented in this dissertation describes the design, fabrication and characterization of a Micro Electro Mechanical System (MEMS) capacitive accelerometer on a flexible substrate. To facilitate the bending of the accelerometers and make them mountable on a curved surface, polyimide was used as a flexible substrate. Considering its high glass transition temperature and low thermal expansion coefficient, PI5878G was chosen as the underlying flexible substrate. Three different sizes of accelerometers were designed in CoventorWare[®] software which utilizes Finite Element Method (FEM) to numerically perform various analyses. Capacitance simulation under acceleration, modal analysis, stress and pull-in study were performed in CoventorWare[®]. A double layer UV-LIGA technique was deployed to electroplate the proof mass for increased sensitivity. The proof mass of the accelerometers was perforated to lower the damping force as well as to facilitate the ashing process of the underlying sacrificial layer. Three different sizes of accelerometers were fabricated and subsequently characterized. The largest accelerometer demonstrated a sensitivity of 187 fF/g at its resonant frequency of 800 Hz. It also showed excellent noise performance with a signal to noise ratio (SNR) of 100:1. The accelerometers were also placed on curved surfaces having radii of 3.8 cm, 2.5 cm and 2.0 cm for flexibility analysis. The sensitivity of the largest device was obtained to be 168 fF/g on a curved surface of 2.0 cm radius. The radii of robotic index and thumb fingertips are 1.0 cm and 3.5 cm, respectively. Therefore, these accelerometers are fully compatible with robotics as well as prosthetics.

The accelerometers were later encapsulated by Kapton[®] superstrate in vacuum environment. Kapton[®] is a polyimide film which possesses similar glass transition temperature and thermal expansion coefficient to that of the underlying substrate PI5878G. The thickness of the superstrate was optimized to place the intermediate accelerometer on a plane of zero stress. The Kapton[®] films were pre-etched before bonding to the device wafer, thus avoiding spin-coating a photoresist layer at high rpm and possibly damaging the already released micro-accelerometers in the device wafer. The packaged accelerometers were characterized in the same way the open accelerometers were characterized on both flat and curved surfaces. After encapsulation, the sensitivity of the largest accelerometer on a flat and a curved surface with 2.0 cm radius were obtained to be 195 fF/g and 174 fF/f, respectively. All three accelerometers demonstrated outstanding noise performance after vacuum packaging with an SNR of 100:1. Further analysis showed that the contribution from the readout circuitry is the most dominant noise component followed by the Brownian noise of the accelerometers. The developed stresses in different layers of the accelerometers upon bending the substrates were analyzed. The stresses in all cases were below the yield strength of the respective layer materials.

AlN cantilevers as tactile sensors were also fabricated and characterized on a flexible substrate. Ti was utilized as the bottom and the top electrode for its smaller lattice mismatch to AlN compared to Pt and Al. The piezoelectric layer of AlN was annealed after sputtering which resulted in excellent crystalline orientation. The XRD peak corresponding to AlN (002) plane was obtained at 36.54°. The fabricated AlN cantilevers were capable of sensing pressures from 100 kPa to 850 kPa which includes soft touching of human index finger and grasping of an object. The sensitivities of the cantilevers were between 1.90×10^{-4} V/kPa and 2.04×10^{-4} V/kPa. The stresses inside the AlN and Ti layer, developed upon full bending, were below the yield strength of the respective layer materials.

Table of Contents

Acknowledgements.....	iii
Abstract.....	iv
List of illustrations	xi
List of Tables	xix
List of Symbols.....	xx
Chapter 1 Introduction.....	1
1.1 Overview of flexible MEMS technology.....	1
1.1.1 Performance of flexible MEMS materials	2
1.1.2 Strategies to achieve flexibility.....	4
1.1.2.1 Intrinsic flexibility	5
1.1.2.2 Geometry	5
1.2 Sensor transduction methods	6
1.2.1 Capacitive	6
1.2.2 Piezoresistive	7
1.2.3 Piezoelectric.....	7
1.3 Applications of flexible sensors.....	7
1.3.1 Prosthetics and robotics	7
1.3.2 Kinesiology.....	9
1.3.3 Sports medicine.....	9
1.3.4 Automobile industry	9
1.4 Dissertation layout	10

1.5 Summary	11
Chapter 2 MEMS accelerometer	12
2.1 MEMS accelerometer types	12
2.2 Theory	12
2.2.1 Spring constant	14
2.2.2 Damping force	15
2.2.2.1 Slide film damping	16
2.2.2.2 Squeeze film damping	17
2.3 State-of-the-art MEMS accelerometers	20
2.4 Summary	22
Chapter 3 Piezoelectric effect	24
3.1 Piezoelectric effect	24
3.2 What causes piezoelectricity?	24
3.3 State-of-the-art piezoelectric materials	27
3.4 Significance of AlN	30
3.5 Summary	31
Chapter 4 Flexible substrate and superstrate	32
4.1 Flexible polyimides	32
4.2 Requirements for polyimides	34
4.3 Summary	39
Chapter 5 MEMS capacitive accelerometers on a polyimide substrate	40

5.1 Introduction.....	40
5.2 Design.....	40
5.2.1 Requirements	40
5.2.2 Process flow.....	41
5.2.3 Accelerometer geometry.....	43
5.3 Performance simulations.....	46
5.3.1 Sensitivity	46
5.3.2 Spring constant	51
5.3.3 Resonant frequency.....	52
5.3.4 Bending and stress	54
5.3.5 Pull-in analysis.....	57
5.4 Fabrication	57
5.5 Performance characterization.....	66
5.5.1 Characterization setup.....	66
5.5.2 Accelerometer on a flat surface	66
5.5.2.1 Sensitivity	66
5.5.2.2 Frequency response.....	68
5.5.3 Accelerometer on a curved surface.....	69
5.5.3.1 Sensitivity	69
5.5.3.2 Frequency response.....	70
5.6 Noise analysis	71

5.7 Pull-in analysis.....	74
5.8 Summary.....	75
Chapter 6 Encapsulation of flexible MEMS accelerometers	76
6.1 Introduction.....	76
6.2 Design requirements	78
6.3 Encapsulation.....	78
6.4 Stress simulation	86
6.5 Characterization.....	87
6.5.1 Sensitivity	88
6.5.2 Flexibility performance.....	88
6.5.3 Noise performance	88
6.6 Effect of encapsulation on accelerometers.....	90
6.7 Summary.....	93
Chapter 7 Ultra-thin AlN cantilevers on flexible substrate.....	94
7.1 Introduction.....	94
7.2 Review of the state-of-the-art AlN cantilevers	94
7.3 Design.....	96
7.4 Simulation.....	98
7.5 Fabrication	100
7.6 EDX and XRD.....	104
7.7 Characterization.....	105

7.7.1 Setup	105
7.7.2 Sensitivity	106
7.7.3 Frequency response.....	108
7.8 Summary	110
Chapter 8 Conclusion.....	111
8.1 Choice of flexible substrate	111
8.2 Novel design of flexible accelerometer	111
8.3 Flexible packaging of accelerometers.....	112
8.4 AlN tactile sensors	112
8.5 Applications	113
Appendix A Accelerometer mask layouts	114
Appendix B CoSolveEM settings for accelerometers capacitance simulation	116
Appendix C Modal and pull-in simulation settings for accelerometers.....	121
Appendix D Simulation setting for banding of accelerometers	124
Appendix E Calculations of ROC.....	126
Appendix F AlN pressure sensor simulation settings	128
References.....	130

List of Illustrations

Figure 1-1 Flexible and stretchable Ag microelectrodes. From [9]. Reprinted with permission from AAAS.....	2
Figure 1-2 (a) Stretched PDMS substrate holding an array of organic transistors interconnected by elastic conductors and (b) curvilinear configuration. From [25]. Reprinted with permission from AAAS.....	3
Figure 1-3 (a) CNTs–PDMS composite capacitive-type sensors showing high linear response during stretching and releasing. Reprinted with permission from [40]. Copyright (2013) Nature Publishing Group and (b) hysteresis from AuNWs–latex rubber composite resistive-type strain sensor. Reprinted with permission from [41]. Copyright 2015, John Wiley and Sons.....	4
Figure 1-4 Stretchable interconnects on elastic polymer surface. Reprinted with permission from [24] © [2005] IEEE.	5
Figure 1-5 Flexible and bendable accelerometer on a human fingertip [8].	8
Figure 2-1 Mass-spring-damper system.....	12
Figure 2-2 Spring connected to the proof-mass.	14
Figure 2-3 Relative motion between plates causing slide film damping.	16
Figure 2-4 Squeeze film damping between two parallel plate.....	18
Figure 2-5 Cross section of accelerometer fabricated on flexible substrate and encapsulated by flexible superstrate	21
Figure 3-1 Directions of polarization of piezoelectric material	25
Figure 4-1 Silicon islands formed on a flexible membrane. Reprinted from [2]. Copyright (2000) with permission from Elsevier.	32

Figure 4-2 PMMA used as release layer and dissolved in solvent for final release. From [3]. Reprinted with permission from AAAS.	33
Figure 4-3 (a) Melting temperature of a crystalline polymer and (b) glass transition temperature of an amorphous polymer. Redrawn with permission from Polymer Science Learning Center (http://pslc.ws/macrog/tg.htm)	34
Figure 4-4 Illustration of an accelerometer on flexible substrate encapsulated by Kapton® superstrate. ...	39
Figure 5-1 Process flow in CoventorWare® for fabrication of flexible accelerometers.	42
Figure 5-2 Thickness of the proof mass and the spring	43
Figure 5-3 Layout of a capacitive MEMS accelerometer	43
Figure 5-4 Proof mass and anchor dimensions of an accelerometer and (b) perforation and pitch size on the accelerometer	44
Figure 5- 5 Change in capacitance vs. acceleration for device (a) A640. (b) A720 and (c) A960 for both simulation and calculation	47
Figure 5-6 Total force vs displacement for (a) A460, (b) A720 and (c) A960	52
Figure 5-7 Six modes of the accelerometer A640. (a) Mode 1 displaying desired vertical movement and (b)-(f) other high frequency vibration modes.	53
Figure 5-8 Modal displacements for (a) A640, (b) A720 and (c) A960 devices	54
Figure 5-9 A960 bent down to 2.5 cm ROC upon application of 4.4 μm displacement on one side of the substrate	55
Figure 5-10 Maximum stress location of Au seed layer of A960.....	56
Figure 5-11 Maximum stress location of Ni proof mass layer of A960	56

Figure 5-12 The complete fabrication process flow of the accelerometers on flexible substrate utilizing double UV-LIGA process. (Not to scale).	58
Figure 5-13 Bottom electrode patterning (a) modeled and (b) fabricated.....	59
Figure 5-14 Backside alignment mark under the device wafer.....	60
Figure 5-15 Backside alignment mark under the device wafer.....	60
Figure 5-16 Patterns after first Ni electroplating and mold resist removal (a) modeled and (b) fabricated	61
Figure 5-17 Pattern after seconds Ni electroplating and mold resist removal (a) modeled and (b) fabricated.....	62
Figure 5-18 Proof mass after Au etching (a) modeled and (b) fabricated.....	62
Figure 5-19 EDX completed inside the holes (a) after Au etching and (b) after ashing.....	63
Figure 5-20 Accelerometers (a) A640, (b) A720 and (c) A960 after complete ashing of the sacrificial layer	64
Figure 5-21 SEM images of A720, tilted at 45 °angle, illustrating bowing of the proof-mass due to residual stress. Left and right photos show the respective edges of the proof-mass connecting to the springs while the center photo is taken at the center of the proof mass. Although the average gap was ~7 m as designed, it varied from ~6.4 to 10 m for each accelerometer from the springs to the proof mass center.....	64
Figure 5-22 Block diagram of the setup for characterization	65
Figure 5-23 Functional block diagram of the MS 3110 readout circuit (redrawn with the permission from Irvine Sensors)	65
Figure 5-24 Time domain response of (a) A640 at 1080 Hz, (b) A720 at 1020 Hz and (c)A960 at 800 Hz.	67

Figure 5-25 Voltage response and change in capacitance for (a) A640 at 1080 Hz, (b) A720 at 1020 Hz and (c) A960 at 800 Hz	67
Figure 5-26 Frequency response from the accelerometers (a) A640, (b) A720 and (c) A960.....	68
Figure 5-27 Experimental setup for characterization of the accelerometers on curved surface	69
Figure 5-28 Contour plot for sensitivity of accelerometers (a) A640, (b) A720 and (c) A960. against frequency and radius of curvature of the surface the device was mounted. Flat surface is denoted by $ROC = \infty$	70
Figure 5-29 Output voltage spectral density along with the read-out circuitry noise and Brownian noise components for device A640 shaken at 1080 Hz. The measured noise floor is dominated by noise originating from the readout circuit.	71
Figure 5-30 Decrease in the gap of A640 between the bottom and suspended electrodes due to the deformation of the proof-mass resulting from electrostatic force.....	72
Figure 5-31 Pull-in analysis carried out in the deformed state of the proof mass and the springs	73
Figure 6-1 Layout of cavity size of accelerometers of geometries (a) A640, (b) A720 and (c) A960	79
Figure 6-2 Step-by-step (a)–(j) encapsulation process flow showing the schematics and device cross section. (Not to scale)	80
Figure 6-3 (a) Pattern on Kapton [®] after Si ₃ N ₄ lift-off and (b) after flipping and bonding.....	81
Figure 6-4 Pattern on Kapton [®] after 2nd Si ₃ N ₄ lift-off	82
Figure 6-5 Completely etched Kapton [®] sheet.....	83
Figure 6-6 HD4110 patterning for forming cavity for accelerometer.....	84
Figure 6-7 Complete etching of the sidewall polyimide.....	85

Figure 6-8. Kapton [®] lifted-off to observe the encapsulated accelerometer	85
Figure 6-9 Accelerometer A960 bent down to 2.5 cm ROC. Z-axis is exaggerated 4 times.....	86
Figure 6-10 Maximum layer stress of (a) Au seed layer, (b) Ni springs, (c) HD 4110 sidewall and (d) Kapton [®] superstrate of A960. ROC = 2.5 cm.....	86
Figure 6-11 Capacitance change of the accelerometers at their resonant frequencies: (a) A640 at 1050 Hz, (b) A720 at 1010 Hz and (c) A960 at 800 Hz when subjected to acceleration. Accelerometers were mounted both on flat and curved surfaces with ROC = 3.8 cm, 2.5 cm and 2 cm.....	89
Figure 6-12 Contour plot for sensitivity of accelerometers (a) A640, (b) A720 and (c) A960 after encapsulation (d) A640, (e) A720 and (f) A960 before encapsulation against frequency and radius of curvature of the surface the device was mounted. Flat surface is denoted by ROC = ∞. The vibration frequency at which the maximum sensitivity is observed is marked for each case	91
Figure 6-13 Noise spectrum of the accelerometers (a) A640, (b) A720 and (c) A960 plotted with the environmental noise when the shaker is turned off and when the shaker is on but the device is off the shaker. The time domain responses of the accelerometers are shown in inset. Also shown are the Brownian noise and the read-out circuitry noise. The peaks are observed at 1050 Hz, 1010 Hz and 800 Hz for A640, A720 and A960 respectively, corresponding to shaker vibration frequency for each case.....	92
Figure 7-1 Process flow for AlN cantilever fabrication.....	96
Figure 7-2 Cantilever layout in CoventorWare [®]	97
Figure 7-3 Cantilever solid model in CoventorWare [®]	97
Figure 7-4 Simulated displacement vs pressure plot of the 60 μm × 12 μm × 0.25 μm cantilever of the cantilever.....	99

Figure 7-5 Simulated displacement upon application of 850 kPa pressure on cantilever tip. The tip displaced 2 μm downward which is equal to the sacrificial layer thickness.....	99
Figure 7-6 Simulated stress at (a) bottom Ti (b) top Ti and (c) AlN layer	100
Figure 7-7 Connection pads are defined after developing the NR9-1500PY photoresist.....	101
Figure 7-8 Cantilever locations are defined and ready for the tri-layer deposition	101
Figure 7-9 Bottom Ti layer deposition.....	102
Figure 7-10 AlN and top Ti layer deposition.....	102
Figure 7-11 Tri layer lift-off.....	103
Figure 7-12 SEM images of completely ashed cantilevers	103
Figure 7-13 Results of the EDX analysis done on the fabricated cantilever	104
Figure 7-14 XRD on AlN cantilever revealing crystal orientation of AlN along 36.54° and Ti along 38.51°	105
Figure 7-15 Block diagram of the measurement setup	105
Figure 7-16 PZT E-665 front panel displaying the required voltage for 2 μm displacement	106
Figure 7-17 Cantilever output voltage plotted against cantilever displacement.....	107
Figure 7-18 Cantilever output voltage plotted against applied pressure on cantilever	107
Figure 7-19 (a) Input voltage at the frequency of 3 Hz to E-665 PZT and (b) output voltage at the frequency of 3 Hz from cantilever	108
Figure 7-20 Power spectral density of the output voltage from Figure. 7-19 (b)	108
Figure 7-21 Output voltages from the cantilever for the input voltages of (a) 5 Hz, (b) 8 Hz, (c) 10 Hz and (d) 15 Hz.....	109

Figure A-1 Layout for A640 (a) bottom electrode, (b) bond pad, (c) sacrificial layer, (d) Au seed layer	114
Figure B-1 Mesher settings for splitting planes	116
Figure B-2 Mesher settings for the accelerometers.....	117
Figure B-3 (a) Solid model of quarter size of accelerometer A640 and (b) after generating mesh	117
Figure B-4 CoSolveEM settings	118
Figure B-5 MemMech settings	119
Figure B-6 MemElectro settings	119
Figure B-7 50 mV applied to the proof mass with respect to the bottom electrode.....	120
Figure B-8 The bottom surface of the anchor is fixed in all direction in SurfaceBCs settings box.....	120
Figure B-9 Acceleration applied on the proof mass in VolumeBCs settings box	120
Figure C-1 MemMech settings for modal analysis.....	121
Figure C-2 CoSolveEM settings for pull-in analysis	122
Figure C-3 Voltage trajectory settings box	122
Figure D-1 Cross section of the solid model of A960 showing the fixed surfaces and the direction of applied displacement. Z-axis exaggerated 10 times.....	124
Figure D-2 Boundary conditions in SurfaceBCs settings box	125
Figure D-3 Acceleration applied in VolumeBCs settings box.....	125
Figure D-4 (a) Displacement and (b) stress in visualizer.....	125
Figure E-1 (a) A960 bent down to 2.5 cm ROC and (b) the bottom electrode coming closer to the proof mass	126

Figure E-2 ROC calculation (a) without Kapton[®] and (b) with Kapton[®] 127

Figure F-1 Fixing the anchor of the cantilever in all directions and applying pressure on the cantilever tip
..... 128

Figure F-2 Solid model after meshing. Z-axis exaggerated 5 times 129

Figure F-3 Fixing the anchor of the cantilever in all directions and applying pressure on the cantilever tip
..... 129

List of Tables

Table 3-1 Curie temperature and limitations comparison among piezoelectric materials	29
Table 4-1 Glass transition temperature for different substrate materials	36
Table 4-2 Young’s modulus and coefficient of thermal expansion (CTE) of the material of different substrates	37
Table 5-1 Simulated sensitivity of A640	48
Table 5-2 Simulated sensitivity of A720	48
Table 5-3 Simulated sensitivity of A960	48
Table 5-4 Calculated sensitivity of A640	49
Table 5-5 Calculated sensitivity of A720	49
Table 5-6 Calculated sensitivity of A960	49
Table 5-7 Trade –off Between Nonlinearity and Sensitivity in Simulated Capacitance Change	50
Table 5-8 Modal frequencies for different accelerometers	52
Table 5-9 Maximum stress at the seed layer and the springs for different accelerometers	55
Table 5-10 Sensitivity comparisons among the accelerometers when mounted on flat and curved surfaces	69
Table 5-11 Comparison between simulated and experimental pull-in voltages considering bowing of the proof mass due to residual stress.....	74
Table 6-1 Sensitivity comparison among the accelerometers on surfaces of different ROCs before and after encapsulation	87
Table 7-1 Comparison among peak output voltages from the cantilever at different frequencies	110

List of Symbols

Symbols	Stand for
a	Acceleration on mass of a mass-spring-damper system (m/s ²)
∂a	Change in applied acceleration (m/s ²)
A	Conversion factor between the input capacitance and the output voltage (V/pF)
A_{eff}	Effective overlapping area between the perforated proof mass and the bottom electrode of the device (m ²)
A_{plate}	Area of each plate of a parallel plate capacitor (m ²)
b	Coefficient of damping (Ns/m)
C_0	Rest capacitance of the accelerometer (F)
C_f	Feedback capacitor of the readout circuit (F)
C_n	Input referred capacitor of MS3110 readout circuit (F)
C_{S1}	Balance capacitor at terminal 1 of the readout circuit (F)
C_{S2}	Balance capacitor at terminal 2 of the readout circuit (F)
C_{S1IN}	Input capacitance at terminal 1 of the readout circuit (F)
C_{S2IN}	Input capacitance at terminal 2 of the readout circuit (F)
C_{S1T}	Total capacitance at terminal 1 of the readout circuit (F)
C_{S2T}	Total capacitance at terminal 2 of the readout circuit (F)
ΔC	Change in capacitance between the proof mass and the bottom electrode (F)
ΔC_T	Capacitance difference between the terminals of the readout circuit (F)
d	Gap between the plates of a parallel plate capacitor (m)
d_{ij}	Induced polarization in i - direction per unit applied stress in j -direction (C/N)
D_i	Electric displacement in i -direction (C/m ²)
E	Young's modulus (Pa)

E_k	Electric field in k -direction (V/m)
F_v	Viscous force between of fluid (N)
F_e	Electrostatic force between plates when voltage is applied (N)
Δf	Signal bandwidth (Hz)
F_{ext}	Force on mass of a mass-spring-damper system (N)
g	Gravitational acceleration (m/s ²)
h	Polyimide film thickness (m)
k	Spring constant (N/m)
k_{ij}^2	Electromechanical coupling coefficient of piezoelectric material
k_B	Boltzmann constant (JK ⁻¹)
k_n	Knudsen number
L	Length of spring (m)
L_c	Length travelled by the damping fluid (m)
L_{pm}	Length of proof-mass (m)
L_t	Length of spring at truss region (m)
m	Mass of the proof mass (kg)
P_a	Ambient pressure (Pa)
p	Damping fluid pressure (Pa)
Q	Relative flow rate coefficient of damping fluid
Re	Reynold's number
R_{out}	SR560 source resistance (Ω)
S_{cap}	Calculated accelerometer sensitivity (fF/g)
S_{meas}	Measured accelerometer sensitivity (fF/g)
S_p	Mechanical strain in p -direction

Mechanical compliance for stress in p - direction and strain in q - direction at

S_{pq}^E	constant electric field E (m^2/N)
t	Time (s)
t_s	Spring thickness (μm)
t_{sac}	Sacrificial layer thickness (μm)
T	Temperature (K)
T_g	Glass transition temperature (K)
$T_g(\text{bulk})$	Bulk glass transition temperature (K)
T_q	Mechanical stress in q -direction (Pa)
v	Damping fluid velocity (m/s^2)
v_x	x-component of damping fluid velocity (m/s^2)
v_y	y-component of damping fluid velocity (m/s^2)
v_z	z-component of damping fluid velocity (m/s^2)
V	Applied voltage between plates (V)
V_{2P25}	Reference test point for MS3110 circuit (V)
v_n	Total noise voltage (V)
v_{Br}	Brownian noise voltage (V)
v_{MS3110}	MS3110 readout circuit noise voltage (V)
V_{out}	Output voltage from the accelerometer (V)
V_{pi}	Pull-in voltage of the accelerometer (V)
V_{ref}	Reference voltage of the readout circuit (V)
v_{SR560}	SR560 amplifier noise voltage (V)
w	Width of spring (m)
w_d	Extended fluid width considering border effect (m)

w_{d0}	Fluid width without considering border effect (m)
w_{pm}	Width of proof-mass (m)
w_t	Width of spring at truss region (m)
x	General displacement of the proof mass (m)
z	Displacement of the proof mass along z-direction (m)
ϵ_0	Permittivity of vacuum (F/m)
ϵ_{air}	Permittivity of air (F/m)
ϵ_r	Relative permittivity of the dielectric material (F/m)
ϵ_{ik}^T	Dielectric constant for dielectric displacement in i -direction and electric field in k -direction under constant stress T (F/m)
μ	Viscosity of the damping medium ($\mu\text{Pa}\cdot\text{s}$)
ν	Poisson's ratio
ζ	Damping ratio
ρ	Density of damping fluid (kg/m^3)
σ_p	Viscous slip coefficient
ω_0	Resonant frequency of the device (rad/s)
ω_c	Cut-off frequency of parallel plate system (rad/s)
λ	Empirical parameter of measuring T_g
λ_m	Mean free path of the damping fluid (m)
δ	Empirical parameter of measuring T_g
δ_{eff}	Effective decay distance (m)
∇	Differential operator

Chapter 1

Introduction

1.1 Overview of flexible MEMS technology

Micro-Electro-Mechanical System (MEMS) is an enabling technology for new discoveries in various arenas including inertial sensing [1], biomedicine [2] and electronic displays [3]. This technology has empowered us to miniaturize devices and commercialize those on a large scale. In the field of wearable technology, there was a revolutionary impact with the widespread applications of the flexible MEMS devices. The endless applications vary from simple aid in health fitness to complex medical surgery [4].

For devices to be wearable, they need to be bendable and stretchable. Devices can be attached conformally if the substrate, on which the device is fabricated, is flexible. Traditional devices fabricated on rigid Si substrates are not capable of providing flexibility and therefore, not suitable for applications in wearable assistive technology. MEMS inertial sensors have dominated the market for years replacing conventional sensors. Sensors, specifically accelerometers, have been deployed in earthquake detection [5], smartphones [6] and airbag deployment systems in cars [7]. The recent trend of fabricating the devices on a foldable substrate [8] facilitates the development of Smart Skin- an array of flexible sensing devices that can measure motion, temperature and pressure. These sensors are being used in research to be a part of robotics and prosthetic limbs [8].

Developing bendable and stretchable substrates has been a great challenge to the researchers. Polyimides are popular choices for a flexible substrate material. Figure 1-1 shows flexible Ag microelectrodes [9] formed on a polyimide substrate which facilitates the bending of the electrodes. During the fabrication process, the temperature limit set by the flexible substrate makes it difficult to fabricate subsequent layers that may require a high temperature process. Bendability also introduces additional stress which should be limited below the yield strength of the respective materials. In spite of

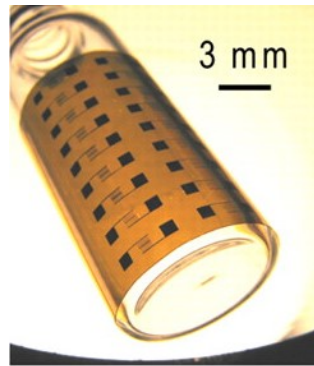


Figure 1-1 Flexible and stretchable Ag microelectrodes. From [9]. Reprinted with permission from AAAS.

all these constraints, many reports have demonstrated successful development and testing of flexible and stretchable MEMS devices [10]. Further research is needed towards the integration of flexible substrates with CMOS and MEMS devices.

1.1.1 Performance of flexible MEMS materials

Besides being flexible, the sensors should fulfill several requirements including stretchability [11], durability [12], low weight [13] and biocompatibility [14]. These flexible sensors include pressure sensors [15], temperature sensors [16], strain sensors [17] and electronic skin (e-skin) [18]. Several works [19] [20] on nanomaterials coupled with flexible polyimides were reported where nanomaterial works as the sensing element due to its excellent electrical, mechanical, chemical and optical properties while the polyimide provides flexible support with outstanding stretchability and durability.

Stretchability-the ability to be extended in any direction was exploited in several works. One of the strategies followed by many researchers was to engineer novel structures instead of developing new materials because of the difficulties to fabricate stretchable electronics [21]. Ultra-thin Si structures offer stretchability as well as excellent absorption of the applied strain [22]. Fabrication of devices on stretchable material was proposed in several works [21] [23]. The second approach of developing stretchable materials paved the path towards the invention of several nanomaterial-based composites. Some of the examples of stretchable materials include polymer composites and very thin metal film on polymer substrate [24]. Highly stretchable electrodes were reported in [21] which are connected to carbon

nano tube (CNT) films and assembled on bandages and clothing. Figure 1-2 demonstrates the stretchability of transistors fabricated on polydimethylsiloxane (PDMS) [25]. Conductive rubber paste [26] [27] was used at the connection of electrodes and CNT film to minimize any mechanical failure. Stretchability of materials was reported to be improved by incorporating nanomaterials in polymer composites. Nanocomposite of silver nanowire and PDMS demonstrated 70% of stretchability [19]. Other works on stretchable nanocomposites combined CNT and ecoflex [28] [29], ZnO nano wire and PDMS [30], graphene and rubber [31] and platinum and PDMS [32].

Linearity between the output performance parameter (for example change in capacitance for capacitive-type sensors or resistance for resistive-type sensors) and the input strain is another important parameter for a flexible material which was reported to have an inverse relationship with stretchability [33] [34] [35]. When the microstructure of the flexible material changes its morphology from homogeneous to nonhomogeneous, non-linearity arises [36]. For example, inhomogeneous microcrack generation and propagation can result in highly nonlinear response in strain sensors [37]. The combination of linear performance and morphologically intactness under stretching cannot be achieved through thin film structure [36].

The flexible film should possess dynamic durability-the capability to maintain good mechanical integrity and stable electrical functionality under long term stretch and release cycles. Durability is more critical when the flexible device is mounted on human skin where the material undergoes several cycles of stretching and releasing. Fatigue can cause the degradation of performance due to lack of durability



Figure 1-2 (a) Stretched PDMS substrate holding an array of organic transistors interconnected by elastic conductors and (b) curvilinear configuration. From [25]. Reprinted with permission from AAAS.

[38] [19]. Hysteresis may also arise due to continuous stretching and releasing cycles. Because of the disturbance in mechanical morphology, thin films will develop different viscoelastic nature [19] [39] which changes their performance. Capacitive strain sensors [40] were reported to have excellent hysteresis performance compared to resistive type sensors [41] as shown in Figure 1-3. This difference in performance is attributed to the fact that in resistive type sensors, the sensing mechanism is highly affected by the change in conductance of the thin-film whereas in capacitive types, only the overlap between the electrodes plays a role in sensing. Conductance is not involved. For flexible films, study of overshoot-the natural phenomenon of instant stress relaxation by mechanical distortion at the end of a stretching cycle-was also reported [40] [42] [43]. During the overshoot, the instant mechanical change at molecular level will not affect the dielectric permittivity, making capacitive sensors to be less sensitive to overshoot, whereas any small change in molecular formation will give rise to higher change in conductivity in resistive type sensors [36].

1.1.2 Strategies to achieve flexibility

Researchers have worked over decades to achieve flexibility of the film materials. Two mainstream strategies were followed, utilizing inherent flexible and stretchable property of certain materials and developing new structures that will minimize the induced stress upon application of external force.

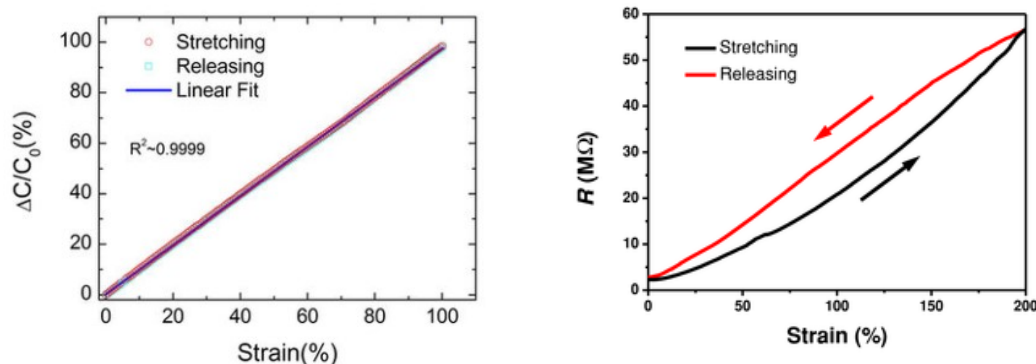


Figure 1-3 (a) CNTs-PDMS composite capacitive-type sensors showing high linear response during stretching and releasing. Reprinted with permission from [40]. Copyright (2013) Nature Publishing Group and (b) hysteresis from AuNWs-latex rubber composite resistive-type strain sensor. Reprinted with permission from [41]. Copyright 2015, John Wiley and Sons.

1.1.2.1 Intrinsic flexibility

Intrinsic flexibility is desired where coplanar devices are required. Materials having intrinsic flexibility can also provide full area coverage when the active layer and the electrodes are fabricated with it. Traditional active layer of light emitting diode (LED) utilizes brittle active layer which was replaced by liquid-like electrochemical layer and electrodes made from polymer composite in [44] and demonstrated 45% stretchability without performance degradation. Intrinsic flexibility and stretchability of CNT was reported in [45] where both electrode and active materials were composed of CNT and PDMS as the dielectric layer. Transistor electrodes and active layers made from graphene were reported to have consistent performance when elongated up to 5%. One major challenge for all these intrinsically flexible and stretchable materials is to develop a proper encapsulant without degradation in performance [46].

1.1.2.2 Geometry

Chronological development of electronic devices shows the use of inorganic semiconductors and metals. These intrinsically brittle materials have excellent performance over the inherently flexible materials [10] discussed before. However, inelastic materials can provide flexibility when appropriate geometrical design is incorporated. Thin layer of inelastic Au can be stretched up to 100% when attached to a flexible and elastic polymer layer [47] [24] shown in Figure 1-4. Flexibility and stretchability can be enhanced by roughening the polymer surface [48] since it hinders the propagation of micro cracks in the

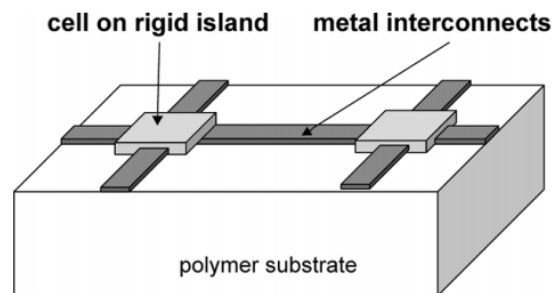


Figure 1-4 Stretchable interconnects on elastic polymer surface. Reprinted with permission from [24] © [2005] IEEE

metal layer and retains the conductive path. Even conductive polymers can be more flexible and stretchable when attached to an elastic substrate. Films of poly(3,4-ethylenedioxythiophene)-poly(styrenesulfonate) known by PEDOT:PSS was reported to maintain conductivity when stretched far beyond its fracture limit [49]. Another method to form a stretchable material is to deposit thin film of polymer on a pre-strained substrate and form a wrinkled layer upon relaxation [50]. This sinusoidal wavy structure allows stretching to the pre-strain limit without inducing any significant strain to the active layer. Electrodes buckled with alumina (Al_2O_3) were reported by Chae *et al* [51]. ZnO transistors offer greater flexibility and stretchability when buckled with a pre-strained substrate [52].

Establishing rigid islands surrounded by flexible polymer interconnects also offer flexibility and stretchability. Functional flexible skin-like transistor islands were formed by S. P Lacour *et al.* where the islands were fabricated on an elastomeric substrate [53]. Same strategy was followed to form transistor islands on a PDMS substrate [53].

1.2 Sensor transduction methods

The mechanical input of a MEMS sensor needs to be converted to an electrical output in order to measure the input magnitude. Various transduction methods of a MEMS sensor are described in this section.

1.2.1 Capacitive

Capacitive sensing has been established in MEMS devices and reported in numerous works [54] [55]. Both vertical and horizontal movement of the electrodes of a capacitive structure can be deployed for MEMS sensing mechanism. Vertical movement is commonly utilized to measure normal force whereas shear force can be quantified by the lateral movement. Capacitive sensors have several advantages including simple governing equation, simplified design and analysis, high strain sensitivity and low power consumption [56]. However, this sensing mechanism requires complex readout circuit [57]. MEMS capacitive sensor using air as a dielectric between electrodes is quite common [58]. Nevertheless other dielectrics like PDMS sandwiched between two layers of PEDOT:PSS was used to

form flexible transparent capacitive sensors [59]. Chapter 2 will provide a detail on capacitive transduction.

1.2.2 Piezoresistive

Piezoresistive sensors transduce any change in mechanical deformation into change in resistance and vice versa. A disturbance in the crystal lattice because of the deformation leads to a change in the band structure of the piezo resistive material and consequently the resistivity changes. Piezoresistive polymer composites are attractive because of their simple integration with device and low cost [10]. Electrical properties of conductive composites vary largely with temperature and show large hysteresis between stress and strain [60]. To eliminate this hysteresis, increasing the concentration of the composite has been proposed [61] which can lead to a stable performance independent of temperature. Polysilicon is advantageous over others as a piezoresistive material because of its high gauge factor, simplicity in deposition and reduced hysteresis compared to metal strain gauges [62].

1.2.3 Piezoelectric

Piezoelectric materials have the capability to generate charges under the application of external force. The force changes the separation between dipoles leading to a build-up of charges on the electrodes. This capability to convert mechanical input to electrical charges is measured by the piezoelectric constant. Lead zirconate titanate (PZT), aluminum nitride (AlN) and zinc oxide (ZnO) are the most commonly used piezoelectric materials for MEMS sensors. Chapter 3 provides more detail on piezoelectric theory and materials.

1.3 Applications of flexible sensors

1.3.1 Prosthetics and robotics

Flexible sensors have widespread biomedical applications [63]. Particularly in robotics and prosthetics, flexible electronics have provided a platform to integrate external contacts while the device is mounted on the robotic or prosthetic limbs. These sensors can offer additional motion sensing that can



Figure 1-5 Flexible and bendable accelerometer on a human fingertip [8]

improve human-robot interactions. The wearer of the prosthetic components can be given feedback for precise motion control based on the sensitivity of the device. Today's robots in the industry can present potential harm to humans [64] and therefore they are confined inside a safety boundary. For enhanced interaction with their surroundings, robots need to possess precise sensing capability, most importantly tactile [65] [66]. A robotic hand, while grasping or manipulating an object, can obtain knowledge on surface hardness, friction, force exerted and curvature [67] when tactile feedback system is provided. This real-world manipulation of unstructured objects by robots, although not at human-level performance [65], is gaining research attraction to make it more enhanced by improving the tactile sensitivity. The learning process for the robots about any unknown objects needs tactile sensors to be mounted on its skin and skin-mountable sensors must possess the capabilities of being bent and stretched [68]. Figure 1-5 demonstrates the mounting of a MEMS flexible accelerometer [8] on a human index fingertip.

Besides achieving more accuracy and human-level perception for robots in the industry, another factor triggered the rapid development of tactile sensing. According to the World Population Prospects from the United nations, 13 percent [69] of the world population is aged over 60 years. This large amount of population would be in need of assistance which can be in the form of wearable technology and robots [70]. Numerous studies [71] [72] [73] have been carried out towards this assistive technology to aid the

aging population. Not only in robotics but also in prosthetic limbs, flexible sensors are the core components [74] [75] to sense motion, orientation or force.

1.3.2 Kinesiology

Kinesiology is another area where flexible sensors have become promising for the study of limbs. Mimicking a human walking pattern by a robot [76] or absorbing the ground impact force by a sensor integrated foot [77] can be of great interest in this area. Full understanding of the motion of human limbs will help to fix many biometric design problems [76]. Various other studies [78] [79] established that the integration of sensors with robotics skin requires flexibility and stretchability.

1.3.3 Sports medicine

A wide variety of studies has been conducted in sports medicine to improve the athlete's performance [80] [81] [82]. Incorporation of wearable devices in sports can greatly enhance the monitoring system of athlete's movements. When sensors like accelerometers are mounted on the athletic clothing or skin, information related to physical loads or impact force can be measured from the response of accelerometers [81]. Quality of training can be improved by the addition of flexible sensors directly mounted on the body. For example, sensors positioned on a golf club or an athlete's body can provide essential information regarding the player's quality of movement [83]. Future research is being directed towards the improvement of the athletes' performance by the inclusion of complex sensors on human body [81].

1.3.4 Automobile industry

Today's high-tech automobiles are equipped with state-of-the-art sensor technology that can assist drivers for detecting collision, controlling speed and recognizing traffic signs [84]. MEMS accelerometers are an essential part inside the airbag deployment system of vehicles. Flexible sensors were reported to be effective for strain measurement [85] when mounted on automobile tire.

1.4 Dissertation layout

The dissertation is divided into eight chapters. The first Chapter provides a brief introduction to flexible MEMS technology and applications of flexible sensors in various arenas of our lives. Numerous benefits of using flexible sensors in robotics, prosthetics as well as in automobiles are presented here.

The second Chapter provides a short narrative for the theory of a MEMS capacitive accelerometer. The mass-spring-damper system of the accelerometer is discussed. Design aspects including spring constant and damping are presented qualitatively. A brief overview of the state-of-the-art MEMS capacitive accelerometers is also outlined here.

Chapter 3 probes into the theory behind the piezoelectric effects of different materials. The significance of AlN and comparison among the piezoelectric materials are presented here. A brief literature review on piezoelectric cantilevers is also included.

Chapter 4 describes the flexible substrate technology and the suitable materials for flexibility. A chronological review of the research work on flexible substrates is presented. Parameters like glass transition temperature and coefficient of thermal expansion (CTE) are considered for choosing the appropriate material for the substrate and the superstrate.

Chapter 5 presents the design, fabrication and characterization process for flexible z-axis capacitive MEMS accelerometers. The Chapter starts with the design requirements followed by the process flow, indicating the steps required for the fabrication of suspended MEMS accelerometers. Next, three accelerometers of different geometry are proposed according to the design requirements and their full specifications are provided. Simulation results from CoventorWare[®] are presented in the next section. Simulated sensitivities for all three accelerometers are tabulated and compared. This section is followed by the spring constant and modal analyses showing the comparative study among the accelerometers. The bending of the accelerometers along with the stress level at different layers are analyzed and compared to yield strength. The pull-in analysis is also shown from the simulations. Next a detailed step-by-step fabrication process incorporating double UV-LIGA (Ultra Violet-Lithografie, Galvanoformung, Abformung) is explained. Characterization setup and the responses from accelerometers are presented in

the following section where the accelerometer is mounted on a flat surface as well as a curved surface. Noise analysis showing the contribution of noise from different sources is quantitatively presented. Lastly, the pull-in analysis considering the hogging of the central proof-mass is described which provides a good match of pull-in voltage with the simulated results.

The sixth Chapter describes the state-of-the-art flexible packaging technology and a detailed encapsulation process using a Kapton[®] superstrate with pre-etched bond pad locations. Backside alignment is the most crucial part of the packaging which is thoroughly described. The same characterization setup described in Chapter 5 is utilized here for the encapsulated accelerometers. A full comparative study of the fabricated accelerometers before and after encapsulation on both a flat and a curved surface is presented here.

Chapter 7 describes the design, fabrication and characterization of AlN cantilevers on a flexible substrate. Simulation results of AlN cantilevers under different pressure are presented. It is followed by the fabrication steps and characterization.

Chapter 8 summarizes the dissertation and provides insight for future work. It is followed by an Appendix section for the mask layouts and the simulation settings.

1.5 Summary

Flexible MEMS technology has gained widespread market acceptance in recent years. Their application in robotics and prosthetics has revolutionized the industry. The current trend of flexible electronics technology points to revenue of 300 billion USD in 2028 [86]. Millions of MEMS sensors are being purchased by the automotive industry each year. An increase in wearable sensor shipment to worldwide market is expected to reach 466 million up from 67 million in 2013 [87]. The capability of these electronics to enable new products requiring flexibility has a large effect not only on inertial sensing but also on biosensors [88], displays [89], photodetectors [90], hybrid CMOS sensors [91], digital x-ray sensors [92], temperature sensors [93] and gas sensors [94].

Chapter 2

MEMS accelerometer

2.1 MEMS accelerometer types

MEMS accelerometer is an integral part of modern smartphones and automobiles [95]. Today's MEMS accelerometers offer integrated readout circuitry and self-test capability with a lower cost than conventional accelerometers [96]. The cost of a MEMS accelerometer has dropped to 10% or less compared to the cheapest conventional commercial accelerometer [97]. Accelerometers operate on different mechanisms depending on their type. The underlying physical mechanism of an accelerometer can be capacitive [98], piezoelectric [99], piezoresistive [100], electromagnetic [101], ferroelectric [102], optical [103] or tunneling [104]. Among these types, the most successful one is of capacitive type because of its simplicity of fabrication, low cost, good stability over temperature and lack of requirement for exotic materials [105]. In this Chapter, the theory and mechanisms for MEMS capacitive accelerometers are discussed.

2.2 Theory

Accelerometers can be modeled by a suspended proof-mass connected to a rigid platform via a spring and damping system as shown in Figure 2-1. Suspended MEMS devices are connected to the

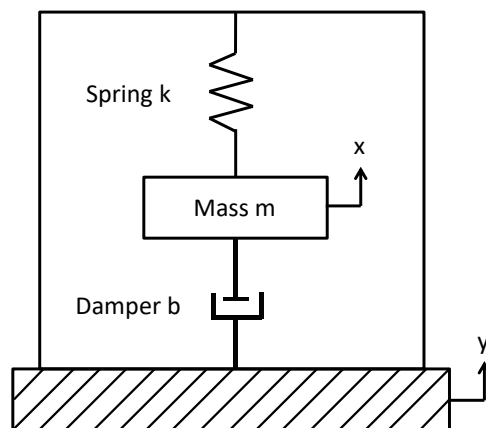


Figure 2-1 Mass-spring-damper system.

substrate by the anchors and anchors are connected to the proof-mass by the spring. The stiffness of the spring depends on the material as well as the geometry. The damping effect causes reduction in the amplitude of an oscillating system which in turn can adversely affect the sensitivity of the system.

The dynamic behavior for the mass-spring-damper system is governed by Newton's second law of motion as shown in Eq. (2-1).

$$m \frac{d^2x}{dt^2} + b \frac{dx}{dt} + kx = F_{ext} = -ma \quad (2-1)$$

where, m = mass, b = damping coefficient, k = spring constant, a = acceleration on mass and x = displacement of the mass. In Figure 2-1, y = displacement of the frame. If the displacement of the proof-mass is z with respect to the frame inside which the accelerometer is contained, we can write $z = y - x$. For vertical z -axis displacement, a is also substituted by g where g is gravitational acceleration.

Laplace transform is taken to obtain the transfer function $H(s)$:

$$H(s) = -\frac{1}{s^2 + \frac{b}{m}s + \frac{k}{m}} \quad (2-2)$$

Typically, accelerometers are operated much below the resonant frequency (ω_0). At those frequencies $H(s) = H(0) = -m/k$ and finally we get,

$$g(t) = -\frac{k}{m}z(t) \quad (2-3)$$

The relation between the resonant frequency ω_0 and the spring constant k is [106]

$$\omega_0 = \sqrt{\frac{k}{m}} \quad (2-4)$$

Therefore, we can write

$$z(t) = -\frac{g(t)}{\omega_0^2} \quad (2-5)$$

This indicates the tradeoff between bandwidth and sensitivity [107]. Higher capacitance results in higher sensitivity for the capacitive accelerometer. Capacitance C between the two parallel plates is given by:

$$C = \frac{\epsilon_0 \epsilon_r A_{plate}}{d} \quad (2-6)$$

where, A_{plate} = area of each plate of a parallel plate capacitor,

d = gap between the parallel plates of a capacitor,

ϵ_0 = vacuum permittivity and

ϵ_r = relative permittivity of the dielectric material.

For a z-axis accelerometer, the change of distance between the proof-mass and the bottom electrode will give rise to the change in capacitance and that change will later be converted to measurable electrical signal by the interface circuit.

2.2.1 Spring constant

The proof-mass of the accelerometer is supported by folded beams or springs. The spring constant of the folded beam spring depends upon the geometry of the beam. The oscillation amplitude of the proof mass in turn depends on the spring constant. Higher value of spring constant leads to stiffer structure which can possibly reduce the mechanical movement of the proof mass. The mechanical restoring force is the spring constant times the displacement of the proof-mass.

W. Wai-Chi *et al.* [108] have developed an expression for the spring constant calculation considering stiffness due to bending moment and shear from each segment of the spring. The whole

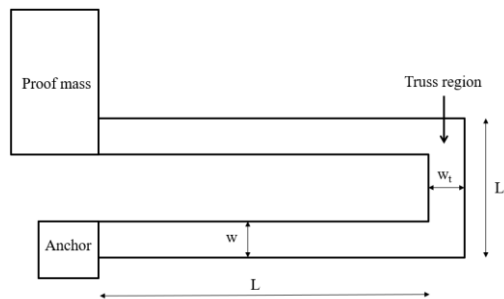


Figure 2-2 Spring connected to the proof-mass.

spring was divided into three parts and the deflection of these three parts was studied individually as depicted in Figure 2-2.

The spring stiffness can be expressed as [108]

$$\frac{1}{k} = \frac{1}{Et_s} \left(\frac{L^3}{2w^3} + \frac{3(1+\nu)L}{5w} + \frac{L_t}{4w_t} - \frac{3LL_t^2}{4w_t^3} \right) \quad (2-7)$$

where, E = Young's modulus

t_s = thickness of the spring

ν = Poisson's ratio

w = width of the spring, w_t = width of the spring at truss region as shown in Figure 2-2

L = length of the spring, L_t = length of the spring at truss region as shown in Figure 2-2

Chae *et al.* [109] proposed a slightly different equation as shown below

$$k \approx \frac{24E}{L^3} \left(\frac{t_s w^3}{12} \right) \quad (2-8)$$

where, t , w and L are the thickness, width and length of the spring respectively. Eq. (2-8) is basically a simplified version of Eq. (2-7) approximating that only bending moment works on the spring whereas Wai-Chi *et al.* [108] considered the deflection of the spring due to the bending moment along with the shear reaction force. The first term in Eq. (2-7) is the contribution of the bending moment towards the spring stiffness and other terms are neglected by Chae *et al.* [109]

In this dissertation, the total displacement of the proof-mass was simulated under different accelerations while fixing the anchors. The total force including the electrostatic force was plotted against displacement to obtain the slope which gives the value of spring constant. The simulated values are then compared with the literature values.

2.2.2 Damping force

Damping force works as an opposing force to the mechanical displacement of the proof-mass. For accelerometers, the vibration energy from the system can be lost because of the interaction of the device

with air. Dissipation of energy can occur in two ways. Either slide film air damping or squeeze film air damping or both can be the reason of damping depending on the accelerometer structure [110].

2.2.2.1 Slide film damping

When two parallel plates are in relative tangential motion, the fluid in between these plates exerts a force opposing this motion. The force that is exerted by the fluid depends on the velocity gradient between the plates, viscosity of the fluid and the area of the moving structure.

Let us consider a parallel plate oscillating in x-direction as shown in Figure 2-3. The Navier-Stokes equation governs the fluid flow and relates several parameters including pressure, density, viscosity and velocity which is given by [111]:

$$\rho \frac{\partial \vec{v}}{\partial t} + \rho \vec{v} \cdot \nabla \vec{v} = \vec{F}_v + \mu \nabla^2 \vec{v} - \nabla P_a \quad (2-9)$$

where, ρ = fluid density, v = fluid velocity in three dimensions = $v_x \hat{i} + v_y \hat{j} + v_z \hat{k}$, F_v = viscous force, P_a = ambient pressure and μ = fluid viscosity. If the moving plate of Figure 2-3 moves only in x-direction, Eq. (2-9) can be simplified to [112]:

$$\frac{\partial v_x}{\partial t} + v_x \frac{\partial v_x}{\partial x} = \frac{\mu}{\rho} \frac{\partial^2 v_x}{\partial z^2} \quad (2-10)$$

Solution to the Navier-Stokes equation leads to a definition of effective decay distance (δ_{eff}) which is the distance along z-direction (Figure 2-3) for which the velocity decays from the moving plate

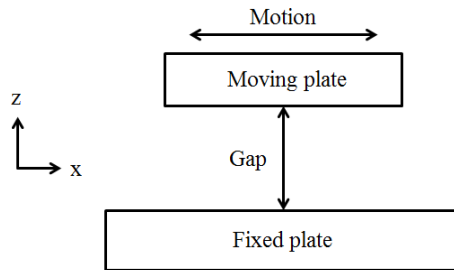


Figure 2-3 Relative motion between plates causing slide film damping

by a factor of $e = 2.718$. Effective decay distance is given by Eq. (2-11):

$$\delta_{eff} = \sqrt{2\mu/\rho\omega} \quad (2-11)$$

where, ω =operating frequency of the system. Two models were proposed for describing the fluid dynamics, depending on the effective decay distance and the oscillation frequency. Without any transient consideration, the fluid dynamics can be modeled by Couette flow which has a linear velocity profile under the condition that the oscillation frequency is low so that $\delta_{eff} \ll d$. The flow pattern of the fluid around the plate is called Couette flow. In this model, velocity gradient at the moving plate is zero and therefore, there is no damping on the top plate and the dissipated energy due to damping occurs only at the bottom. However, the Couette model is not applicable when the gap is comparable to or bigger than δ_{eff} .

Stokes flow describes the fluid motion when the gap between the moving and the fixed plates is large and the oscillating frequency is high. In this model, the viscous force dominates over the inertial force. Reynold's number is the criteria to measure the ratio between the inertial force to the viscous force. Reynold's number is given by [62]

$$Re = \frac{\rho v L_c}{\mu} \quad (2-12)$$

where, L_c = travelled length of the fluid. When Reynold's number is bigger than 1, i.e. inertial force dominates over viscous force, the flow of the fluid is turbulent. On the other hand, when the viscous force is dominant, the flow is laminar.

2.2.2.2 Squeeze film damping

Squeeze film damping is the main source of energy dissipation in parallel-plate structures oscillating vertically. When two plates come close to each other, the air in between them gets squeezed and the pressure created there causes the air flow to move out of the gap. Thus, the squeeze film acts as a damper to the system as shown in Figure 2-4.

With the assumptions of isothermal condition (no temperature gradient along the fluid thickness), uniform fluid thickness and negligible inertial force compared to viscous force, the Navier-Stokes equation and continuity equation can be simplified to compressible-fluid Reynold's equation [113] [114]:

$$\frac{\delta}{\delta x} \left(\frac{d^3 \rho \delta p}{\mu \delta x} \right) + \frac{\delta}{\delta y} \left(\frac{d^3 \rho \delta p}{\mu \delta y} \right) = 12 \frac{\delta(\rho d)}{\delta t} \quad (2-13)$$

For structures where the gap between the parallel plates changes in time, Eq. (2-13) can be further reduced to [115] [116]

$$\frac{d^3 Q}{12\mu} \left(\frac{\delta \Delta p}{\delta x^2} + \frac{\delta \Delta p}{\delta y^2} \right) = \frac{d \delta \Delta p}{P_a \delta t} + \frac{\delta d}{\delta t} \quad (2-14)$$

where, Q = relative flow rate of the fluid. Q is formulated in [115]:

$$Q = 1 + 9.638(K_n)^{1.159} \quad (2-15)$$

where, K_n = Knudsen number which relates the mean free path of the fluid (λ_m) and gap between the parallel plates (d) as shown below:

$$K_n = \frac{\lambda_m}{d} \quad (2-16)$$

$K_n < 0.001$ defines the continuum flow regime and the flow rate coefficient becomes 1. Knudsen

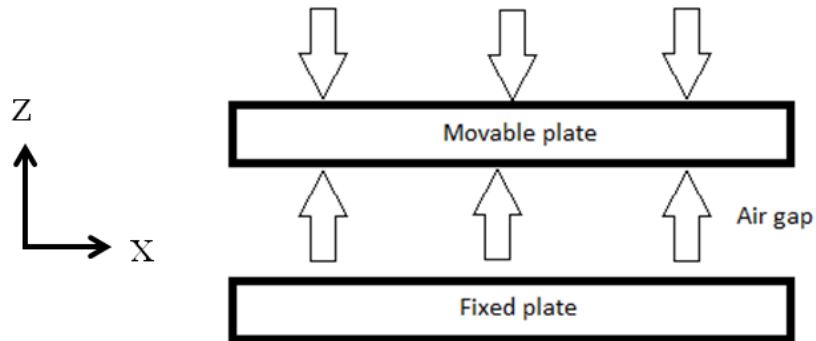


Figure 2-4 Squeeze film damping between two parallel plate.

number is a measure of fluid rarefaction effect which is included in the Reynold's equation.

The resonant frequency of an oscillating system is discussed before. There is also a cutoff frequency for the parallel plate system which is defined as the frequency at which the fluid's spring force is equal to the damping force. This is given by [117]

$$\omega_c = \frac{\pi^2 d^2 P_a}{12\mu} \left(\frac{1}{w_{pm}^2} + \frac{1}{l_{pm}^2} \right) \quad (2-17)$$

where, P_a = the ambient pressure and w_{pm} = width of the proof-mass and l_{pm} = length of the proof-mass.

At low frequencies, damping force maintains a linear relationship with the velocity of the moving plate and the film acts as a pure damper but as the frequencies increases, the relationship turns out to be non-linear and at very high frequencies, the fluid acts as a spring [117]. At a specific frequency, this spring force counterbalances the viscous force of the fluid. This frequency is the cut-off frequency of the oscillating system and squeeze number is used to define it. Squeeze number is the ratio between the spring force due to fluid compressibility and the viscous force of the fluid and at cut-off frequency, these two forces become equal. Low value of squeeze number indicates incompressible fluid. Results from W. E. Langlois [118] showed that fluids with squeeze number smaller than 0.2 show essentially incompressible behavior. On the other extreme when the squeeze number is large, the fluid's performance is similar to an air spring. The operating frequency of a system is lower than the resonant frequency and the resonant frequency is again much lower than the cut-off frequency. In this case, the system is under-damped and the squeeze action is slow so that the fluid has enough time to leak. The damping ratio is a measurement of decaying of oscillation in a system after a disturbance. The damping ratio is given by [111]

$$\zeta = \frac{b}{2m\omega_0} \quad (2-18)$$

where, ζ = the damping ratio.

ζ is a dimensionless quantity. If $\zeta > 1$, the system is over damped and if $\zeta = 1$, it is critically damped. For an over damped system, it takes longer time to come to rest compared to critically damped system. In case of an underdamped system where $\zeta < 1$, the system oscillates with an amplitude gradually decreasing to zero. To reduce the squeeze film damping effect, the proof-mass is sometimes perforated to allow the air escape through the holes instead of the borders which results in increased sensitivity.

Another effect named border effect has contribution towards damping when the damper width is comparable to the fluid gap. The border effect can be included in the damping model by considering the surface elongation of a parallel plate configuration and modifying the fluid width [119] as shown below:

$$w_d = w_{d0} + 1.3(1 + 3.3\sigma_p K_n)d \quad (2-19)$$

where, w_d = extended fluid width considering border effect, w_{d0} = fluid width without border effect, σ_p = viscous slip coefficient, a measure of interfacial damping. Inertial effect can dominate for large fluid thickness and at high frequencies. At frequencies well below the cut-off frequency, the compressibility of the gas can be disregarded and the inertial effects can be overlooked [117].

2.3 State-of-the-art MEMS accelerometers

Many reports can be found on MEMS accelerometers towards improving linearity [120], cross-talk sensitivity [121], noise floor [122], reliability [123] and flexibility [124]. One of the challenges in realizing flexibility of MEMS accelerometers is that the largest subcomponent, the proof-mass, in the sensor is typically fabricated using the device layer of SOI wafers [125] [126], bulk-micromachined crystalline Si [127] or a combination there-of [128]. Although these pioneering works demonstrated excellent functionalities, metal offers much more flexibility as a proof-mass material. Single-level UV-LIGA [129] process has been used to fabricate metal proof-mass MEMS accelerometers [130]. Although flexibility and high aspect ratios are achieved with a single-step UV-LIGA, this process restricts the springs and the proof-mass to be the same thickness, thus greatly limiting the design parameters and the performance.

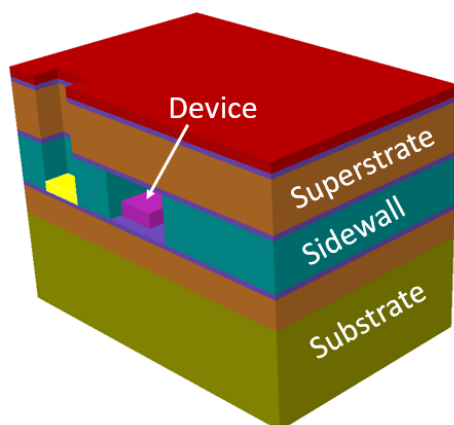


Figure 2-5 Cross section of accelerometer fabricated on flexible substrate and encapsulated by flexible superstrate

Multi-layer electroplated accelerometers have shown a higher sensitivity because of the increased displacement of the proof-mass under same amount of acceleration compared to their single layer counterparts on both rigid [131] [132] and flexible substrates [98]. The latter [98] demonstrated an increase in sensitivity for approximately the same size of the device [130] using double UV-LIGA. EFAB™ (Electrochemical Fabrication) technology [133] is capable of achieving highly complex 3D structures with “Instant Masking”™ [134]. One of the intermediate processes involves a planarization step after blanket-deposition of each material. This abrasive process provides less control on vertical accuracy [135] and requires additional tools. There is no requirement for a blanket deposition or a planarization step in the fabrication process of the accelerometers described in this dissertation. It utilizes a precisely controlled electroplating technology to achieve more accurate vertical dimensions.

To achieve complete bendability, accelerometers are required to be packaged with a flexible superstrate. Epitaxial Si layer was deployed as the superstrate for accelerometers fabricated on a rigid Si substrate [136]. A full Si wafer with cavities was also reported in [137] [138] as a superstrate. The encapsulation process described in those works involve patterning and etching of rigid Si with Bosch DRIE process, which necessitates several cycles to etch in the Si. Spin-coated polyimide film on a flexible superstrate with cavities achieved by dry etching [131] or drilling by laser [139] poses potential risk of damaging the underlying device. In this dissertation, the Kapton® sheet was used as a superstrate

as shown in Figure 2-5, which was pre-etched before thermo-compressive bonding to the flexible device wafer, thus eliminating possible damaging steps. Polyimides were also reported as the underlying substrate and top superstrate [140] [141] to embed ultra-thin dies. Although Al_2O_3 has been used as a packaging material [142], because of its low flexibility, it limits the bending capability of the devices. Chapter 4 will provide details on the state-of-the-art flexible substrate materials.

Highly sensitive MEMS accelerometers fabricated on rigid Si substrate were reported in several works. Micromachined accelerometers described by C. P. Hsu *et al.* [143] have a proof-mass size of $5 \text{ mm} \times 5 \text{ mm}$ and demonstrated a sensitivity of 42.5 fF/g , utilizing a gap closing structure for capacitive sensing. G. Langfelder *et al.* [144] showed a sensitivity of 6 fF/g for a proof-mass area of $450 \mu\text{m} \times 600 \mu\text{m}$ of a differential fringe-field MEMS accelerometer fabricated on a rigid Si substrate. The accelerometers designed and fabricated in this dissertation demonstrated a sensitivity of 195 fF/g for the largest area of proof-mass and bendability down to 2.5 cm ROC . Multi-level LIGA in conjunction with new low temperature processing techniques employing several different polyimides allowed us to realize a flexible MEMS accelerometer with high sensitivity and low noise (SNR better than 100:1). Preliminary findings on this work have been presented in [98]. Later work [124] significantly expanded on what has been reported in terms of device designs, time-domain response characterization, analyses of hysteresis and noise. In addition, linearity and variation of sensor response from device to device are also reported here. The bendability of the accelerometers makes an important distinction from the previous works and significantly widens the application area including robotics, prosthetics and sports medicine.

2.4 Summary

This chapter provides a brief introduction to the design parameters of MEMS accelerometer including spring constant and damping force. Spring constant can be designed by selecting optimized values of thickness, width and length. Damping force limits the motion of the proof-mass of an accelerometer. Techniques like perforated proof-mass is very effective in minimizing the damping force [98]. However, the damping can be further reduced when the devices are vacuum packaged. To enable the

accelerometers to bend, flexible substrate has been used. Polyimides are attractive candidates to introduce bendability not only to the underlying substrate but also to the superstrate and make the whole device fully compatible with a curved surface.

Chapter 3

Piezoelectric effect

3.1 Piezoelectric effect

Some materials have the capability to generate electricity when they encounter mechanical deformation. This phenomenon is called piezoelectric effect. The deformation on the material produces stress inside the crystal lattice leading to a separation of charge. Higher the deformation, higher the stress and more current is generated. The piezoelectric effect also works well in the opposite way i.e. the material gets deformed when electric current is applied. Therefore, piezoelectric materials can be deployed as a sensor as well as an actuator. Although the piezoelectricity was discovered over hundred years ago [145], its applications exist in many stages of our lives. It is used in electronic clocks, gas ovens, inkjet printers, and many other appliances. The automotive and the aerospace industry requires high temperature piezoelectric material [146] which can be fulfilled by the inherent property several piezoelectric materials. Scientific instruments, like microscopes [147] and nano-positioning systems [148] which require extremely precise movements also utilize the piezoelectric effect.

3.2 What causes piezoelectricity?

The overall electric field consisting of all the randomly arranged dipoles inside a piezoelectric material is zero. An applied electric field aligns all the dipoles in the same direction and after the removal of the electric field, the dipoles maintain the alignment. When this material is compressed, the internal charge distribution gets imbalanced. Some dipoles come close together whereas others go far apart. This imbalance disturbs the neutrality and there is a net separation of charge. This gives rise to a net positive charge at one end and a net negative charge at the other end. In case of stretching, the polarity changes the direction. There is also inverse piezoelectric effect which works in exactly the opposite way. When an electric field is applied, the dipoles encounter an electric field and they need to move to rebalance themselves. This movement of the dipoles causes the material to deform. The opposite voltage will

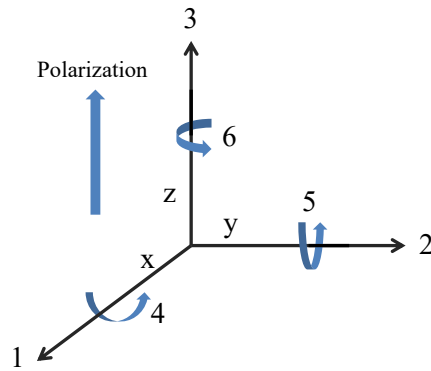


Figure 3-1 Directions of polarization of piezoelectric material

deform the material in the other direction whereas, an AC signal will continuously vibrate the material at the frequency of the signal.

Piezoelectric materials are characterized by several constants that measure the capability of generating charge or deformation of the materials. The most important constant is the piezoelectric coefficient which is usually denoted by d_{ij} where, the first subscript represents the direction of the applied electric field or the direction of the aligned dipoles and the second subscript represents the direction of the mechanical stress or strain. For example, there are piezoelectric coefficients such as d_{33} and d_{31} . The polarization directions are shown in Figure 3-1. Usually the direction of polarization is made to coincide with z-axis. Here, d_{33} represents induced polarization in direction 3 per unit applied stress in direction 3 and d_{31} represents induced polarization in direction 3 per unit applied stress in direction 1. In most cases, d_{33} is the parameter used for a comparison among piezoelectric materials [149]. Besides this piezoelectric coefficient, there are mechanical stress, strain, compliance, permittivity, electric field and electromechanical coupling factor which are also of interest in the study of piezoelectricity.

The development of internal electric field upon strain or the experiencing of strain upon the application of electric field can be in any direction. Therefore, depending on the material, the electric field in one direction can give rise to mechanical strain in any direction. The governing equations relating the

mechanical and electrical quantities are generally represented with tensors. Considering the tensors, the governing equations are:

$$D_i = d_{iq}T_q + \varepsilon_{ik}^T E_k \quad (3-1)$$

$$S_p = s_{pq}^E T_q + d_{pk} E_k \quad (3-2)$$

where, D_i = electric displacement in i -direction, E_k = electric field in k -direction, T_q = mechanical stress in q -direction, S_p = mechanical strain in p -direction, s_{pq}^E = mechanical compliance tensor, ε_{ik}^T = dielectric constant tensor and d_{pk} = piezoelectric coefficient tensor. These expressions essentially describe the relationship between mechanical and electrical behaviors of the piezoelectric material. Eq. (3-1) shows that part of the electric field applied to the material is converted into mechanical stress. Correspondingly, Eq. (3-2) expresses the conversion of mechanical strain into electrical field. In the absence of any electric field, Eq. (3-2) becomes Hooke's law which relates the stress and strain of the material. Likewise, when the mechanical part is missing in Eq. (3-1), it essentially describes the material's electric behavior. The x, y and z-directions of a piezoelectric system are generally denoted by subscripts 1, 2 and 3 whereas, the shear ones are represented by subscripts 4, 5 and 6. Using these directions, Eqs. (3-1) and (3-2) can be rewritten in a matrix form as:

$$\begin{bmatrix} S_1 \\ S_2 \\ S_3 \\ S_4 \\ S_5 \\ S_6 \end{bmatrix} = \begin{bmatrix} s_{11}^E & s_{12}^E & s_{13}^E & s_{14}^E & s_{15}^E & s_{16}^E \\ s_{21}^E & s_{22}^E & s_{23}^E & s_{24}^E & s_{25}^E & s_{26}^E \\ s_{31}^E & s_{32}^E & s_{33}^E & s_{34}^E & s_{35}^E & s_{36}^E \\ s_{41}^E & s_{42}^E & s_{43}^E & s_{44}^E & s_{45}^E & s_{46}^E \\ s_{51}^E & s_{52}^E & s_{53}^E & s_{54}^E & s_{55}^E & s_{56}^E \\ s_{61}^E & s_{62}^E & s_{63}^E & s_{64}^E & s_{65}^E & s_{66}^E \end{bmatrix} \begin{bmatrix} T_1 \\ T_2 \\ T_3 \\ T_4 \\ T_5 \\ T_6 \end{bmatrix} + \begin{bmatrix} d_{11} & d_{12} & d_{13} \\ d_{21} & d_{22} & d_{23} \\ d_{31} & d_{32} & d_{33} \\ d_{41} & d_{42} & d_{43} \\ d_{51} & d_{52} & d_{53} \\ d_{61} & d_{62} & d_{63} \end{bmatrix} \begin{bmatrix} E_1 \\ E_2 \\ E_3 \end{bmatrix} \quad (3-3)$$

$$\begin{bmatrix} D_1 \\ D_2 \\ D_3 \end{bmatrix} = \begin{bmatrix} d_{11} & d_{12} & d_{13} & d_{14} & d_{15} & d_{16} \\ d_{21} & d_{22} & d_{23} & d_{24} & d_{25} & d_{26} \\ d_{31} & d_{32} & d_{33} & d_{34} & d_{35} & d_{36} \end{bmatrix} \begin{bmatrix} T_1 \\ T_2 \\ T_3 \\ T_4 \\ T_5 \\ T_6 \end{bmatrix} + \begin{bmatrix} \varepsilon_{11}^T & \varepsilon_{12}^T & \varepsilon_{13}^T \\ \varepsilon_{21}^T & \varepsilon_{22}^T & \varepsilon_{23}^T \\ \varepsilon_{31}^T & \varepsilon_{32}^T & \varepsilon_{33}^T \end{bmatrix} \begin{bmatrix} E_1 \\ E_2 \\ E_3 \end{bmatrix} \quad (3-4)$$

In general, the crystal system of the piezoelectric material defines the tensors described above.

For AlN which has a hexagonal structure, the above equations become [150]

$$\begin{bmatrix} S_1 \\ S_2 \\ S_3 \\ S_4 \\ S_5 \\ S_6 \end{bmatrix} = \begin{bmatrix} s_{11}^E & s_{12}^E & s_{13}^E & 0 & 0 & 0 \\ s_{21}^E & s_{22}^E & s_{23}^E & 0 & 0 & 0 \\ s_{31}^E & s_{32}^E & s_{33}^E & 0 & 0 & 0 \\ 0 & 0 & 0 & s_{44}^E & 0 & 0 \\ 0 & 0 & 0 & 0 & s_{55}^E & 0 \\ 0 & 0 & 0 & 0 & 0 & s_{66}^E \end{bmatrix} \begin{bmatrix} T_1 \\ T_2 \\ T_3 \\ T_4 \\ T_5 \\ T_6 \end{bmatrix} + \begin{bmatrix} 0 & 0 & d_{13} \\ 0 & 0 & d_{23} \\ 0 & 0 & d_{33} \\ 0 & d_{42} & 0 \\ d_{51} & 0 & 0 \\ 0 & 0 & 0 \end{bmatrix} + \begin{bmatrix} E_1 \\ E_2 \\ E_3 \end{bmatrix} \quad (3-5)$$

$$\begin{bmatrix} D_1 \\ D_2 \\ D_3 \end{bmatrix} = \begin{bmatrix} 0 & 0 & 0 & 0 & d_{15} & 0 \\ 0 & 0 & 0 & d_{24} & 0 & 0 \\ d_{31} & d_{32} & d_{33} & 0 & 0 & 0 \end{bmatrix} \begin{bmatrix} T_1 \\ T_2 \\ T_3 \\ T_4 \\ T_5 \\ T_6 \end{bmatrix} + \begin{bmatrix} \varepsilon_{11}^T & 0 & 0 \\ 0 & \varepsilon_{22}^T & 0 \\ 0 & 0 & \varepsilon_{33}^T \end{bmatrix} + \begin{bmatrix} E_1 \\ E_2 \\ E_3 \end{bmatrix} \quad (3-6)$$

Another important parameter used is the electromechanical coupling coefficient (k_{ij}) of the material which measures the conversion efficiency between electrical and mechanical energy. The first subscript denotes the direction in which the electric field is developed or applied and the second subscript denotes the direction in which the mechanical energy is developed or applied. For direct piezoelectric effect,

$$k_{ij}^2 = \frac{\text{Converted electrical energy}}{\text{Input mechanical energy}} \quad (3-7)$$

and for inverse piezoelectric effect, the inverse is taken to calculate the electromechanical coupling factor. When both stress and electric field are along direction 3 (parallel to the direction in which the material is polarized), the electromechanical coupling factor is given by [151]

$$k_{33}^2 = \frac{d_{33}^2}{\varepsilon_{33}^T s_{33}^E} \quad (3-8)$$

3.3 State-of-the-art piezoelectric materials

Although piezoelectric effect has been widely utilized in our lives, there are very few materials that exhibit excellent piezoelectric effect. Due to weak piezoelectric effect of many materials, those are

not suitable for many applications. On the other hand, having a high piezoelectric coefficient does not necessarily make it compatible with existing CMOS processing technology. The most investigated piezoelectric materials to date are lead zirconium titanate (PZT) [152], lithium niobate (LiNbO_3) [153], zinc oxide (ZnO) [154] and aluminum nitride (AlN) [155] [156].

AlN film has been rather less investigated than PZT and ZnO films because of its smaller piezoelectric constant. It is generally known that piezoelectric materials with a higher Curie temperature (temperature at or above which materials lose their magnetic property due to the collapse of dipole alignment) possess a lower piezoelectric coefficient [157]. The Curie temperature and piezoelectric coefficient of PZT, which is widely used in many electronic devices, are $250\text{ }^\circ\text{C}$ and 410 pC/N [157]. There is a recent movement towards the elimination of lead in piezoelectrics in response to environmental and safety concerns [158] and therefore PZT is facing diminishing interest in the field of piezoelectrics [159]. AlN has a Curie temperature $> 2000\text{ }^\circ\text{C}$ [160] and piezoelectric coefficient of 5.5 pC/N [157]. It is difficult to achieve a good balance between high Curie temperature and large piezoelectricity in a material, and no effective piezoelectric materials with these characteristics have yet been found [157]. Very few piezoelectric materials have been tested at high temperatures. The problems associated with the high temperatures are phase transition, decomposition, aging and dielectric loss [161]. The very high Curie temperature of AlN makes it a very attractive piezoelectric material for CMOS processing. A comparison of Curie temperature and problems related to high temperature process among some piezoelectric materials are shown in Table 3-1. Other features like electrical resistivity and mechanical quality are equally important as temperature compatibility. Quartz has a very high electrical resistivity ($>10^{17}\ \Omega\text{-cm}$) at room temperature [146]. It also possesses high temperature stability and good mechanical quality factor, an indicator of the material's ability to retain energy through oscillatory phenomena. All these qualities of quartz cannot override its low piezoelectric coefficient and high mechanical loss, which is inverse of mechanical quality factor, at temperature above $450\text{ }^\circ\text{C}$. GaPO_4 is another piezoelectric material that exhibits comparable properties like good piezoelectric coefficient and high electrical

resistivity. However, at temperatures above 700 °C, the structural hardness deteriorates. Another option for high temperature applications is Langasite (lanthanum gallium silicate) which has a very high melting point of 1470 °C [146]. Nevertheless, its low electrical resistivity at elevated temperatures limit its applications [162]. Yttrium calcium oxoborate (YCOB) has also gained attention as a promising candidate for high temperature applications. It has demonstrated stable piezoelectric property and high electrical resistivity ($> 2 \times 10^8 \Omega\text{-cm}$) at 800 °C [162] [163].

Table 3-1 Curie temperature and limitations comparison among piezoelectric materials

Piezoelectric material	Curie temperature (°C)	Limitations at high temperature
ZnO	250	Conductance drops with temperature [164]
PZT	< 400	Degradation in electromechanical and piezoelectric properties [165]
Quartz	450	Low piezoelectric coefficient and high losses at high temperature [146]
LiNbO ₃	1150	Resistivity falls above 600 °C [146]
AlN	> 2000	Diffusion of oxygen, cracking [160]

Most of the piezoelectric materials are made of nitrides and oxides of metals and act like inert materials. The crystallinity of the deposited material is vital since it defines the amount of piezoelectricity. The crystallinity, in turns, is a strong function of the deposition temperature or the annealing temperature [166]. The deposition temperature ranges from 200 °C to 800 °C [167]. Contact piezoelectric transducers require acoustic coupling between the sensing and testing element and at elevated temperatures ($>400 \text{ °C}$), the coupling fluids evaporate [168]. Therefore, a very compliant coupling fluid is hardly achievable to meet those conditions. Until now, the number of piezoelectric materials that can be utilized at high processing temperatures and simultaneously maintain excellent mechanical quality factor has been limited.

A good stoichiometry and morphology are required for good piezoelectric properties. This can be achieved by effective control of nucleation and the crystallization process. Several deposition techniques for piezoelectric materials have been developed. Deposition of AlN by a DC sputtering process [169], ZnO by RF magnetron sputtering [170] and PZT by hydrothermal deposition [171] have shown excellent piezoelectric property.

3.4 Significance of AlN

AlN has been widely considered as a high temperature piezoelectric material with a maximum operating temperature of 1150 °C [157]. AlN can be directly deposited onto components and thus, the establishment of acoustic coupling between components at high temperature can be realized [168]. US air force conducted an experiment where extreme high temperature condition (1100 °C) was applied [172] for transmission and reception of ultrasound by AlN at the high pressure of 150 MPa. AlN also showed good thermal, mechanical and physical stability at temperature up to 1000 °C [146]. Properties such as temperature independence of electromechanical properties and electrical resistivity of 10^{11} to 10^{13} Ω -cm [146] have made AlN a very promising candidate for high temperature operations [173] [174]. Other exceptional characteristics of AlN include low thermal resistivity ($2.85 \text{ Wcm}^{-1}\text{K}^{-1}$) and small CTE ($4.5 \times 10^{-6} / ^\circ\text{C}$) [175].

Besides the competition among piezoelectric materials for high temperature applications, AlN has also an upper hand over another popular opponent ZnO in terms of resistivity. AlN is a wide bandgap material (6.2 eV) [176] at room temperature whereas ZnO has a bandgap of 3.3 eV [177]. Therefore, ZnO holds an inherent risk of smaller resistivity. For sensors and actuators operating at frequencies lower than 10 kHz, this low resistivity gives rise to high dielectric loss [178]. For its high piezoelectric coefficient, ZnO is better suited for bulk acoustic wave (BAW) generation whereas AlN is well suited for deflection sensors. On the other hand, PZT has a much higher piezoelectric coefficient than both AlN and ZnO.

Because of its lead content, smaller electric field generation and most importantly incompatibility with high temperature processes, it is not a promising candidate like AlN.

AlN has been widely used as piezoelectric material for thin film bulk acoustics wave resonators [179] [180]. Several works reported the use of AlN as piezoelectric material in fingerprint detectors [181], microphones [182] and vibrational energy harvester [183]. Its compatibility with CMOS manufacturing makes it a superior contender although AlN has low piezoelectric coefficient. Recent trend of making alloy to enhance the piezoelectric property of AlN while maintaining its compatibility with CMOS foundry has shown promises. Particularly Scandium (Sc) alloying with AlN has been reported [184] [185].

3.5 Summary

This chapter has provided a brief introduction to piezoelectric effect and materials. In general, piezoelectric materials with higher piezoelectric coefficients are preferred. Out of many materials, AlN has greater flexibility over other piezoelectric materials like ZnO, PZT, quartz and LiNbO₃. Despite its lower piezoelectric coefficient, the capability of being processed at high temperature manufacturing processes has made AlN a more promising candidate as a piezoelectric material. Other properties of AlN such as high thermal conductivity and small CTE are also attractive. Today's sensor and actuator industry requires high temperature materials for automotive and aerospace and AlN is one of the very few materials that have the capability to meet that demand.

Chapter 4

Flexible substrate and superstrate

4.1 Flexible polyimides

The key part of a flexible device is the substrate on which it is fabricated since this layer defines the extent of flexibility and the device performance. Choosing the right material is, therefore, very crucial to maintain device conformality to a curved surface. The trend of fabricating flexible devices got redefined over time. The first attempt to form devices on a flexible substrate was reported in by Barth *et al.* [186]. Si islands containing conventional ICs were fabricated on top of a polyimide flexible substrate. However, the devices suffered failure during squeezing and folding tests. Initially, the technique to form the flexible area was to form the Si islands first and after formation of the ICs, the islands were cut from the Si wafer and thus only a foldable membrane was obtained afterwards. An enhanced technique was mentioned by Jiang *et al.* [187]. The backside of (100) Si was selectively etched by tetramethyl ammonium hydroxide (TMAH). Four layers of Al and polyimide were the formed as shown in Figure 4-

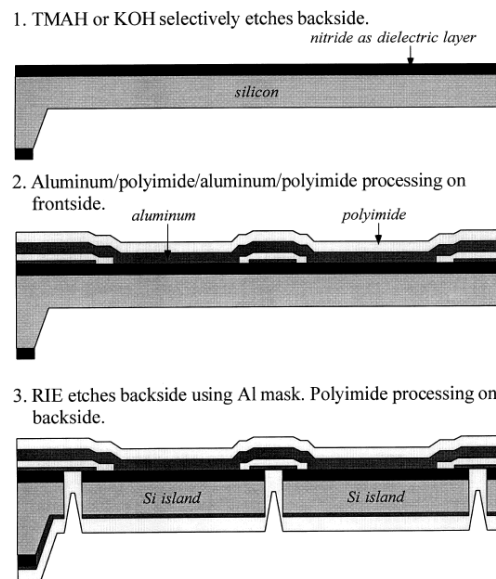


Figure 4-1 Silicon islands formed on a flexible membrane. Reprinted from [187]. Copyright (2000) with permission from Elsevier.

1. Si was then etched at the edges of the islands by reactive ion etching. Finally, after depositing a thick polyimide layer at the backside, the islands were carefully cut off from the Si wafer. This technology was first utilized to fabricate sheer-stress sensor array. This process requires the rigid Si islands to be totally covered by the polyimide. Since Si is not intrinsically flexible and stretchable, it will also limit the flexible coverage area.

Kim *et al.* [188] have shown a process where ICs can be fabricated on a thin polyimide substrate on top of a release layer. Polymethyl methacrylate (PMMA) was used as a release layer and subsequently dissolved by acetone when releasing as illustrated in Figure 4-2. Cao *et al.* [189] also mentioned a process which has the limitation of solubility and low glass transition temperature. Polyamic acid was applied in between the carrier wafer and the polyurethane polyimide substrate. A photoresist was employed by Kim and Najafi [190] to bond parylene based polyimide with the Si wafer. Later the wafer was dissolved in acetone after making an opening at the edge. A paper based flexible substrate was fabricated by Siegel *et al.* [191] but it showed fatigue when bent repeatedly. When a device on a flexible substrate is packaged, the superstrate may cause additional stress due to the mismatch of coefficient of thermal expansion (CTE). An attempt to balance the CTE between the substrate and the superstrate was reported by Christiaens *et al.* [142]. Later ashing was utilized in several works [192] [62] to form suspended

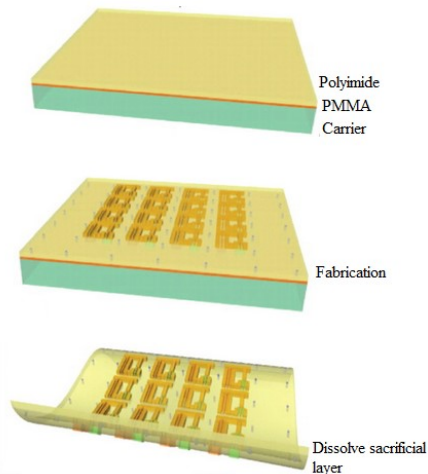


Figure 4-2 PMMA used as release layer and dissolved in solvent for final release. From [188]. Reprinted with permission from AAAS.

structures. After complete ashing, the die is cut off from the carrier wafer and the wafer can be reused again for another process.

4.2 Requirements for polyimides

Polyimides have been used as a flexible substrate in several works which are described in Chapter 1. They offer intrinsic flexibility as well as many desirable mechanical, electrical and chemical properties including excellent mechanical strength, small dielectric constant and chemical inertness [193]. Applicability in integrated circuit electronics require high temperature processing in addition to outstanding mechanical and electrical stability and polyimide is the best fit there. Because of their exceptional mechanical stability and high strength to weight ratio, polyimides are replacing metals [194] for structural applications. Some of the desired properties of polyimides are discussed in this section.

- **High glass transition temperature (T_g)**

Glass transition temperature of a polyimide is that temperature where the polyimide transitions from a solid glassy state to a viscous liquid state. Regardless of the technological development of numerous new glassy materials, T_g itself is not very well understood [195]. T_g is different from the melting point of a polyimide. Melting only occurs in the crystalline structure and above the melting point that crystal-like structure collapses whereas glass transition happens to an amorphous polyimide even

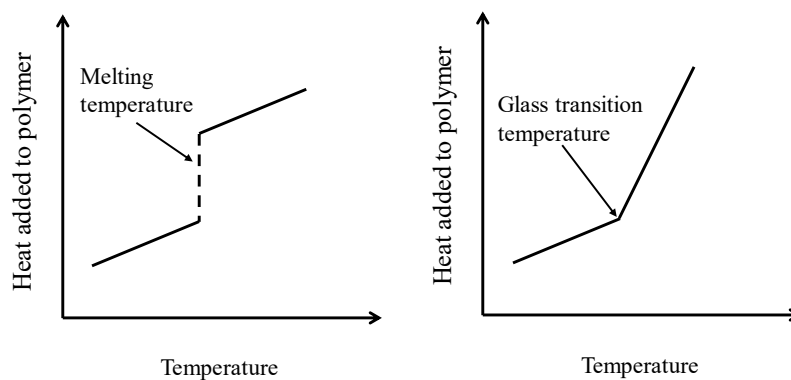


Figure 4-3 (a) Melting temperature of a crystalline polymer and (b) glass transition temperature of an amorphous polymer. Redrawn with permission from Polymer Science Learning Center (<http://pslc.ws/macrog/tg.htm>)

though they are solid and glassy. Above T_g , the polyimide becomes more pliable rubbery and has a higher heat capacity. Figure 4-3 shows the difference between melting point and T_g . The heat capacity of an amorphous polymer increases beyond its glass transition temperature [196] indicated by the increase in slope in Figure 4-3(b) after T_g . Lower T_g indicates that its polymer chains can move more effortlessly than that one having a higher T_g . This temperature is very critical for MEMS fabrication since it limits the highest processing temperature of the device. Therefore, polyimides having a high T_g are very attractive for MEMS processing.

The relation between T_g and the film thickness was reported by J. A. Forest *et al* [195]. An empirical equation relating these two parameters was proposed as shown in Eq. (4-1)

$$T_g(h) = T_g(bulk)[1 - (\lambda/h)^\delta] \quad (4-1)$$

where, $T_{g(bulk)}$ = bulk glass transition temperature, h = film thickness, $\lambda = 32 \text{ \AA}$ and $\delta = 1.8$. The reduction of T_g with the decrease of film thickness was also reported by J. K. Keddie *et al.* [197]. They suggested the presence of a liquid like layer on the polymer surface which expands more for thinner films as T_g is approached. The exact opposite behavior was reported in [198] where T_g of PMMA was investigated on a Si substrate with native oxide on it. It was observed that with the decrease of PMMA thickness, T_g increases slightly. It was speculated that the hydrogen bonding at the interface restricts the polymer chain mobility and as a result, T_g increases.

The fabrication process described in this work does not need any solvent to release the flexible substrate. Instead it utilizes a low bond-strength release layer PI2611 which has a high glass transition temperature. Another polyimide PI5878G is used to form the substrate on top of the release layer. The glass transition temperatures of the material of few flexible substrates are shown in Table 4-1. Because of its high glass transition temperature, PI5878G is an excellent choice for a bendable substrate. Temperature sensors were formed on PI5878G and were reported [199] to work without any loss of

performance. In this work, the release layer (PI2611) was cured at 350 °C which set the maximum processing temperature.

Table 4-1 Glass transition temperature for different substrate materials

Substrate materials	Glass transition temperature (°C)
PI5878G [200]	> 400
PI2611[201]	360
PMMA [202]	< 106
Polyurethane [203]	< 65
Parylene [204]	< 90
Kapton® [205]	360 - 410

- **High tensile strength**

Tensile strength is a measurement of mechanical firmness. The tensile strength of polyimides can be increased by proper incorporation of nanomaterials. Combination of graphene with polyimide can significantly enhance the polyimide toughness [206]. There is an increasing demand for polyimides with increased strength in microelectronics, aerospace and fuel industries [206]. Over the last few years, several developments in the polyimide strength were reported by incorporation of organic and inorganic materials including TiO₂ [207], Al₂O₃ [208], graphene oxide [209], boron nitride (BN) [210] and SiO₂ [211]. Polyimide composite films have a tensile strength of 134 MPa [206] while Kapton® has a tensile strength up to 234 MPa [205]. High tensile strength of polyimides leads to higher resistance to fatigue and cracking under stress [212].

- **Low thermal expansion coefficient**

The most effective strategy to minimize the stress on polyimides is to reduce the CTE mismatch [213]. Polyimides are often in total contact with other fabrication layers like Si or Si₃N₄. Low CTE value indicates smaller mechanical stretching with temperature increase and results in less induced stress. When polyimide is formed on rigid Si, it will experience stress depending on the CTE mismatch. CTE of Si is 2.6 ppm/°C and Young's modulus is 180 GPa [214]. To reduce any additional stress on the flexible substrate, the substrate material should have similar CTE value. Therefore, there are limited options for

the substrate material. After the fabrication of the device, when the substrate is gently peeled off from the Si wafer, any stress remaining in the substrate will cause curvature. Therefore, stress management is essential when dealing with the flexible substrate. The CTE of Si is close to that of PI2611 release layer as shown in Table 4-2. Therefore, it will induce very little stress during curing. The very low values of CTE of the substrate PI5878G and superstrate HD4110 will have insignificant effect on device stress. Young's Modulus is important for stress management. To keep the device on a plane of minimal stress, the engineering of the substrate as well as the superstrate is required. It is discussed in Chapter 6.

Table 4-2 Young's modulus and coefficient of thermal expansion (CTE) of the material of different substrates

	Young's modulus (GPa)	CTE (ppm/°C)
Si [214]	163-188	2.6
PI2611 [201]	8.5	3
PI5878G [200]	2.3	20
HD4110 [215]	3.4	35
Kapton® [216] [205]	4	20

- **Very low outgassing in vacuum**

Polyimides have relatively higher outgassing rate at elevated temperature [217]. Despite this fact, they have been widely used as insulating, spacer and sealing materials [218]. A comparative study on the outgassing behavior of several polyimides including Kapton®, Vespel®, Meldin®, polyetheretherketone (PEEK) and polybenzimidazole (PBI) was reported in [217]. Kapton® demonstrated outgassing rate of $1.3 \times 10^{-8} \text{ Pa m}^3\text{s}^{-1}\text{m}^{-2}$ whereas others outgassed between $1.1 \times 10^{-3} \text{ Pa m}^3\text{s}^{-1}\text{m}^{-2}$ and $4.0 \times 10^{-8} \text{ Pa m}^3\text{s}^{-1}\text{m}^{-2}$. Lower outgassing rate has made Kapton® an excellent candidate for MEMS processing.

- **Usability at cold temperatures**

Aerospace and aviation industry requires materials to be usable at ultra-low temperatures. Silver nanowire (AgNW) and polyimide composites demonstrated applicability down to $-150 \text{ }^\circ\text{C}$ [219] whereas Kapton® has been used successfully in applications at temperatures down to $-269 \text{ }^\circ\text{C}$ [205].

- **Application dependent thermal conductivity**

Polyimides generally possess low thermal conductivity which is useful for most of the microelectronic applications. However, some applications require heat dissipation through the polyimides which demands high thermal conductivity of the polyimides [220]. Polyimides usually have thermal conductivity in the order of $0.1 \text{ Wm}^{-1}\text{K}^{-1}$. For example, Kapton[®] has thermal conductivity value of $0.12 \text{ Wm}^{-1}\text{K}^{-1}$ [205]. Polyimides with lower thermal conductivity can possibly over-heat the electronics. A variety of nanomaterials including Al_2O_3 [221], SiC [222], SiO_2 [223] and Si_3N_4 [224] were introduced inside polyimides to increase their thermal conductivity. Polyimides with SiC nanowires were reported in [220] having their thermal conductivity increased to $0.577 \text{ Wm}^{-1}\text{K}^{-1}$.

- **Chemical inertness**

Chemical resistance is required for those polyimides which are deployed as substrates in many electronics and MEMS process because they need to encounter several solvents for subsequent processing steps. In general, polyimides are inert to alcohols and acids. There is no known chemical solvent for Kapton[®] [205].

- **Other properties**

For wider range of applications, polyimides which are inflammable and highly resistive to radiation, are very attractive. Polyimides like Kapton[®] are widely used in high radiation environments where flexible insulating material is required [225]. Other desired properties include insensitivity to humidity, temperature and extended thermal aging.

Figure 4-4 illustrates the cross-section of an accelerometer fabricated during this dissertation work. The device is formed on a flexible substrate PI5878G and encapsulated by Kapton[®] superstrate. The sealing polyimide chosen is HD4110 since its Young's modulus and CTE values are close to those of PI5878G substrate and Kapton[®] superstrate. No solvent is required in the process to suspend the device

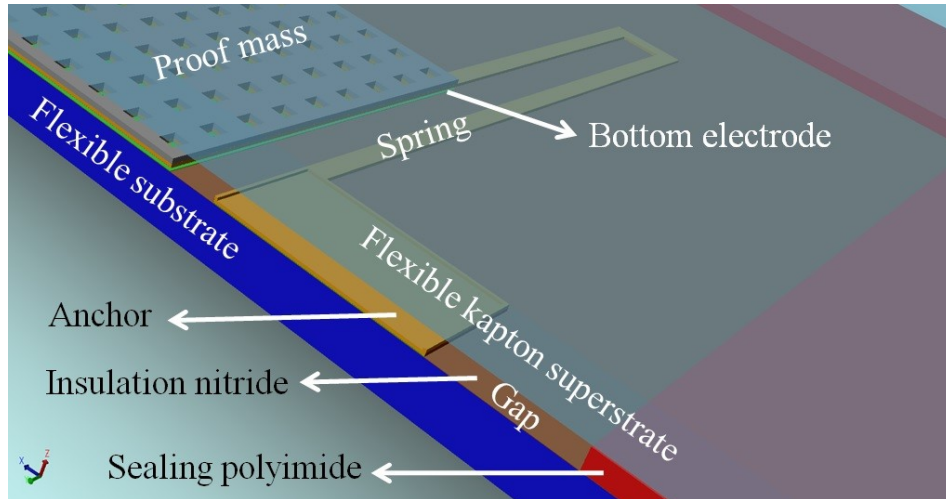


Figure 4-4 Illustration of an accelerometer on flexible substrate encapsulated by Kapton® superstrate.

since the process utilizes oxygen plasma ashing. Complete bendability is assured as the device lies in between a flexible substrate and a superstrate.

4.3 Summary

The chapter has introduced the state-of-the-art polyimides for flexible substrates as well as flexible superstrates. Polyimide is unquestionably the best choice among all other materials for bendability. Among several polyimides, certain factors such as T_g , CTE, tensile strength, outgassing, ultra-low temperature performance, chemical resistance and thermal conductivity are considered to obtain the best possible option. For minimal stress at the substrate, CTE value close to Si was desired for our fabrication. Commercially available Kapton® sheets were suitable for the superstrate considering all the required properties. The work in this dissertation utilizes PI5878G polyimide as a flexible substrate and Kapton® as a superstrate.

Chapter 5

MEMS capacitive accelerometers on a polyimide substrate

5.1 Introduction

Sensors fabricated on flexible substrates have shown a lot of promise due to their ability to bend and conform to non-planar surface. Rigid surface limits the applications of sensors. The major challenge lies in the formation of the flexible substrate without any loss of performance. Previous fabrication processes for flexible substrates suffered problems like low glass transition temperature [204] and releasing sacrificial layer in solvents like acetone, isopropyl alcohol (IPA) and methanol [226]. Application of low adhesion strength release layer has removed the requirement of the solvent. Stress management is also vital in maintaining the functionality of the device. Various research is now oriented towards the achievement of better device performance as well as retaining stability and reliability. In near future, the flexible sensor technology is expected to deeply penetrate into different applications including automotive, consumer electronics, defense, energy and healthcare.

5.2 Design

5.2.1 Requirements

A typical capacitive accelerometer consists a proof mass, springs, electrodes and connection pads. For a vertical gap-closing type, the bottom electrode lies underneath the suspended proof mass. This gap is formed by a sacrificial layer which is removed at the end of the fabrication. The springs connect the proof mass to the substrate with the anchors. One bond pad is connected with the proof mass and the other one is coupled with the bottom electrode. The proof mass along with the springs is suspended on the substrate.

The capacitance between the proof mass and the bottom electrode is similar to two parallel plate capacitors. As the proof mass moves closer to the bottom electrode, the capacitance increases and vice versa. Without any external acceleration, only gravity works and the capacitance between these two parts under this condition is called the rest capacitance.

The spring constant k defines the stiffness of the springs. In equilibrium, the weight of the proof mass is balanced by the mechanical restoring force of the spring as shown in Eq. (2-3). Here, the damping force is ignored and it is assumed that the device operates much below the resonant frequency.

This relation shows that if the mass of the proof mass m is large and the value of the spring constant is small, the displacement must be high and therefore it will result in high sensitivity. Eq. (2-5) expresses the tradeoff between the sensitivity and the bandwidth. Higher displacement and higher sensitivity result in smaller resonant frequency and the bandwidth becomes limited. The target resonant frequency of the accelerometer is 1 kHz to provide a wide range of low frequency applications in robotics, prosthetics, sports medicine and automotive air bag deployment system. For a vibrating system, the resonant frequency ω_0 is given by Eq. (2-4). The target spring constant value was set to be 2 N/m. This value of the mechanical spring constant is smaller when compared to the accelerometer having dimensions of $650 \mu\text{m} \times 650 \mu\text{m} \times 3 \mu\text{m}$ which was reported in [62] to have spring constant of 7.9 N/m. The gap between the proof mass and the bottom electrode was set to 7 μm . Devices with smaller gap will not sustain under high acceleration due to the collapse of the moving plate. On the other hand, larger gap reduces the sensitivity. This is an optimized value chosen for the best performance of the device. The smallest radius of curvature of human thumb is 3.5 cm whereas it is 1.0 cm for index finger [227]. The accelerometers should be capable of being bent down to that level if they are to be mounted on robotic or prosthetic extremities. Once these parameters are set, one can start the design of the springs and proof mass.

5.2.2 Process flow

CoventorWare[®] software was used to design and simulate the z-axis accelerometer. For all the simulations, a common process flow was used as shown in Figure 5-1. It starts with a 50 μm thick polyimide substrate which is used as the flexible substrate. Next, there is a 0.5 μm of Si_3N_4 deposition on top of the polyimide. Following the Si_3N_4 , there is a 0.5 μm thick sputtered and patterned layer of Al to serve as a bottom electrode. Each layer of patterning requires a mask as named in the “Mask Name”

Number	Step Name	Layer Name	Material Name	Thickness	Mask Name	Photoresist
0	Substrate	substrate	POLYIMIDE	50	substrate_mask	
1	Sputtering Si3N4	Insulator	SI3N4	0.5		
2	Sputtering bottom electrode	bottom electrode	ALUMINUM	0.5		
3	Pattern bottom electrode				bottom_electrode	+
4	Sputtering bondpad	bondpad	ALUMINUM	0.5		
5	Patterning bondpad				bondpad_mask	+
6	Sputtering sacrificial layer	sacrificial layer	POLYIMIDE	7		
7	Pattern sacrificial layer				sacrificial_mask	-
8	Gold seed layer	gold seed layer	GOLD	0.1		
9	Sputtering electrode	first nickel	NICKEL	3		
10	Patterning nickel1				nickel1	+
11	Sputtering electrode	second nickel	NICKEL	5		
12	Patterning nickel1				nickel2	+
13	Etching gold				gold_mask	+

Figure 5-1 Process flow in CoventorWare® for fabrication of flexible accelerometers

column. Another layer of 0.5 μm thick Al is deposited and patterned after forming the bottom electrodes. This step utilizes bond pad mask which makes the bond pad locations thicker (1 μm). Then a sacrificial layer (7 μm) is deposited and patterned with negative a photoresist to open the anchor areas. The anchor area is the connecting region between the substrate and the springs.

Afterwards Au seed layer (0.1 μm) is deposited and on top of that mold photoresist is patterned to open the Ni electroplating areas. Two layers of Ni are plated on top of Au. These layers have a thickness of 3 μm and 5 μm , respectively. Final steps are to remove the mold resist, etch the Au and ash the sacrificial layer to suspend the proof mass. The whole fabrication process flow can be shown sequentially below

- Flexible substrate and insulation layer deposition
- Sacrificial layer deposition
- Seed layer formation
- Mold resist deposition
- Electroplating proof mass and
- Ashing sacrificial layer

5.2.3 Accelerometer geometry

A MEMS accelerometer has several performance parameters. The most important ones are spring constant, resonant frequency, sensitivity, stress and radius of curvature for bending. These parameters must be optimized to achieve the desired performance. As discussed before, there are tradeoffs among these parameters.

To increase the displacement of the proof mass z as well as the sensitivity, the mass m can be increased as shown in Eq. (2-3) since spring stiffness k is independent of the proof mass and it depends

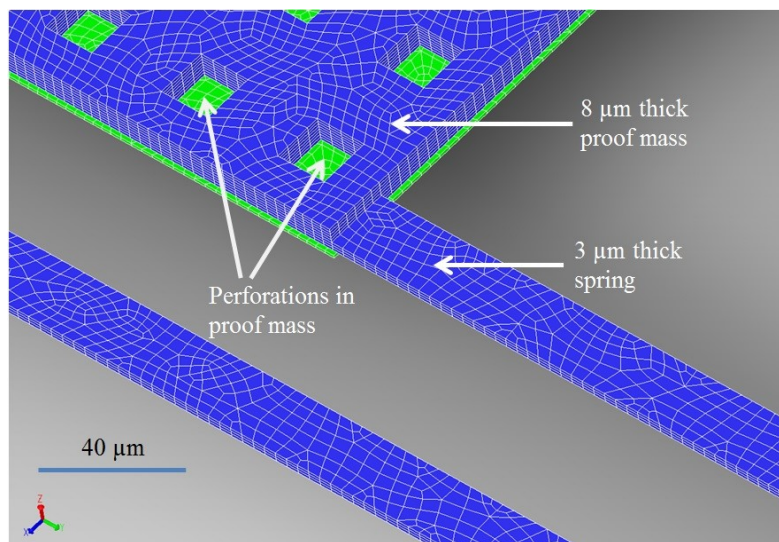


Figure 5-2 Thickness of the proof mass and the spring

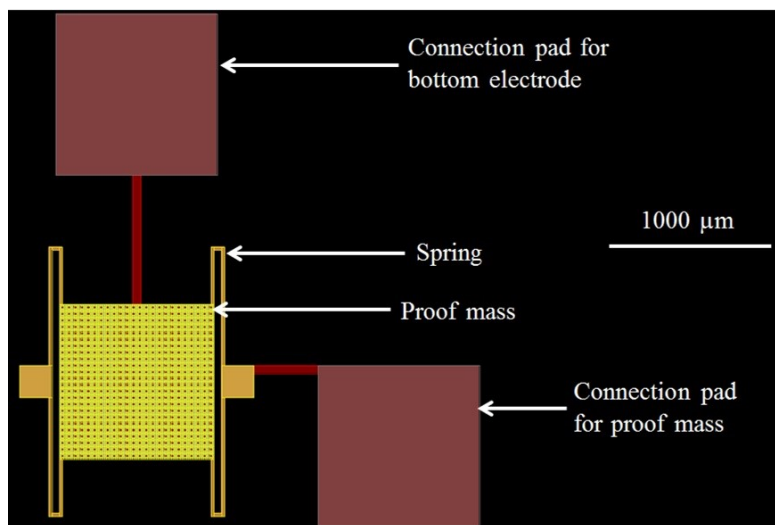


Figure 5-3 Layout of a capacitive MEMS accelerometer

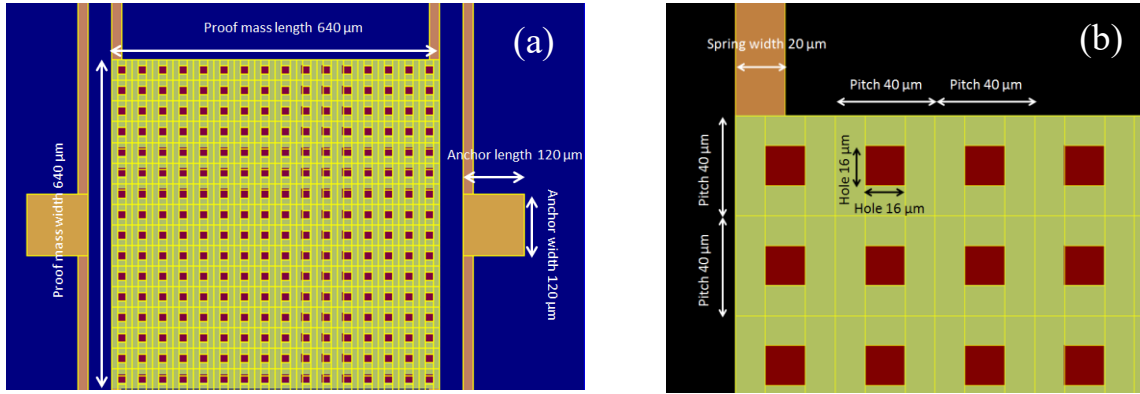


Figure 5-4 Proof mass and anchor dimensions of an accelerometer and (b) perforation and pitch size on the accelerometer

only on the geometry of the springs. One way of increasing the mass is to increase the area of the proof mass but increased area will limit the bending capability. In this current work, the proof mass was designed to be thicker than the springs as shown in Figure 5-2. Here, the spring and proof mass thicknesses are 3 μm and 8 μm , respectively. With this thicker proof mass, the device will have increased displacement as well as sensitivity and it will not limit the resonant frequency.

A full layout of a MEMS capacitive accelerometer is shown in Figure 5-3 with different parts labeled. The springs are connected with the anchors. The accelerometers will be suspended everywhere except the anchor locations. Anchor dimension of an accelerometer compared to the whole device is shown in Figure 5-4(a). The proof mass is perforated to facilitate the releasing process of the proof mass. The pitch of the holes of each of the devices is 40 μm with the hole size of 16 $\mu\text{m} \times 16 \mu\text{m}$ as shown in Figure 5-4(b). Therefore, the distance from one hole to another is 24 μm . During the last step of fabrication, ashing is required to remove the sacrificial layer. The farthest distance for O_2 to ash the polyimide is half the distance between the holes i.e. 12 μm . This is achievable with the available tool Deiner asher.

The design of the accelerometer spring is one of the most vital parts of the whole design. The design criteria include the capability of holding the heavier central proof mass as well as providing

sufficient displacement for the proof mass to achieve high sensitivity. The lengths and widths of the springs were optimized for all three different sizes of accelerometers named as A640, A720 and A960.

Geometry and other details of A640, A720 and A960 are given below.

1. Accelerometer A640 specifications:

- a. Proof mass length \times width = $640 \mu\text{m} \times 640 \mu\text{m}$
- b. Spring length, $L = 335 \mu\text{m}$ on smaller side and $595 \mu\text{m}$ on longer side
- c. Spring width, $w = 20 \mu\text{m}$
- c. Spring thickness, $t_s = 3 \mu\text{m}$
- d. Proof mass thickness = $8 \mu\text{m}$
- e. Proof mass hole dimensions = $16 \mu\text{m} \times 16 \mu\text{m}$
- f. Hole pitch = $40 \mu\text{m}$
- g. Number of holes = 256
- h. Anchor size = $120 \mu\text{m} \times 120 \mu\text{m}$
- i. Sacrificial layer thickness, $t_{sac} = 7 \mu\text{m}$

2. Accelerometer A720 specifications:

- a. Proof mass dimensions = $720 \mu\text{m} \times 720 \mu\text{m}$
- b. Spring length, $L = 335 \mu\text{m}$ on smaller side and $635 \mu\text{m}$ on longer side
- c. Spring width, $w = 20 \mu\text{m}$
- d. Spring thickness, $t_s = 3 \mu\text{m}$
- e. Proof mass thickness = $8 \mu\text{m}$
- f. Proof mass hole dimensions = $16 \mu\text{m} \times 16 \mu\text{m}$
- g. Hole pitch = $40 \mu\text{m}$
- h. Number of holes = 324
- i. Anchor size = $120 \mu\text{m} \times 120 \mu\text{m}$
- j. Sacrificial layer thickness, $t_{sac} = 7 \mu\text{m}$

3. Accelerometer A960 specifications:
 - a. Proof mass dimensions = $960\ \mu\text{m} \times 960\ \mu\text{m}$
 - b. Spring length, $L = 335\ \mu\text{m}$ on smaller side and $715\ \mu\text{m}$ on longer side
 - c. Spring width, $w = 20\ \mu\text{m}$
 - d. Spring thickness, $t_s = 3\ \mu\text{m}$
 - e. Proof mass thickness = $8\ \mu\text{m}$
 - f. Proof mass hole dimensions = $16\ \mu\text{m} \times 16\ \mu\text{m}$
 - g. Hole pitch = $40\ \mu\text{m}$
 - h. Number of holes = 576
 - i. Anchor size = $200\ \mu\text{m} \times 200\ \mu\text{m}$
 - j. Sacrificial layer thickness, $t_{sac} = 7\ \mu\text{m}$

5.3 Performance simulations

The simulation results of A640, A720 and A960 devices are presented below.

5.3.1 Sensitivity

A640 has a proof mass size of $640\ \mu\text{m} \times 640\ \mu\text{m}$ and it is the smallest device among the three. The convergence analysis was done to achieve maximum accuracy. Since acceleration is applied vertically on the proof mass, it is required to confirm that sufficient number of segments is there vertically both in the proof mass and in the spring since acceleration will be applied vertically and these two parts will move in vertical direction. Finite element method (FEM) requires sufficiently refined mesh to accurately model any device. In all cases, extruded brick meshing scheme was used to refine the mesh to reduce the element size consistently in the area where the springs interface with the proof mass. As seen from Figure 5-2, the mesh size is reduced at the interface between the proof mass and the spring. Elements get smaller as the mesh is refined. It helps to capture the motion more accurately. Extruded

brick meshing automatically reduces the element size wherever it finds any interface. This is not achievable with other meshing schemes such as manhattan or triangular brick meshing.

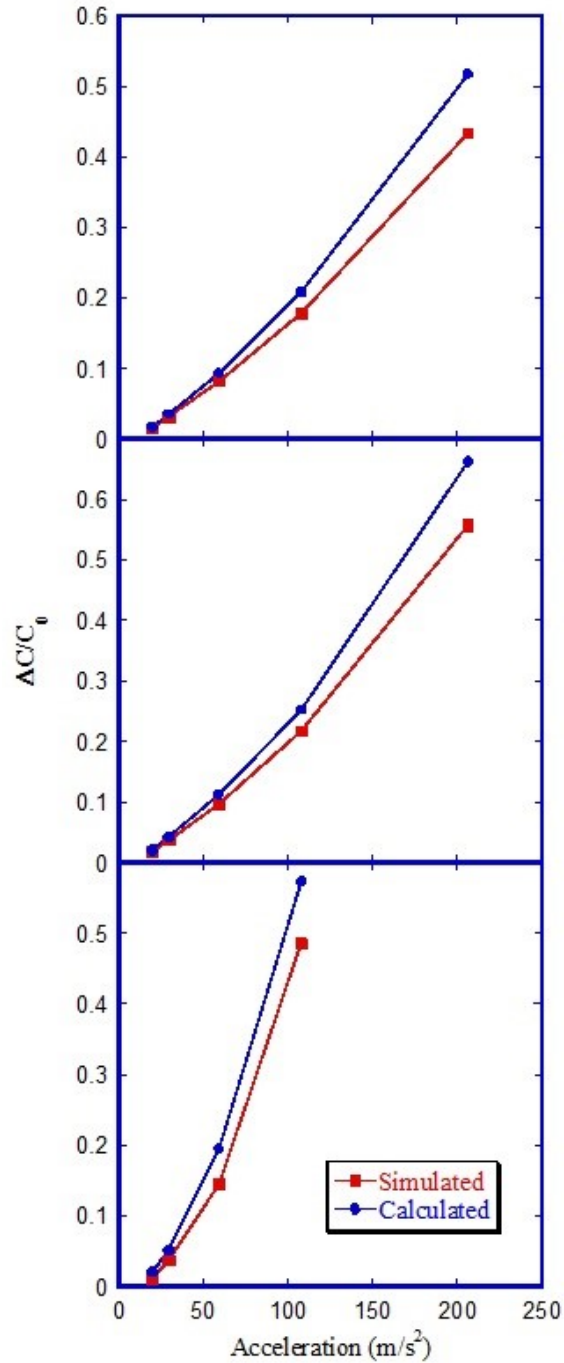


Figure 5- 5 Change in capacitance vs. acceleration for device (a) A640. (b) A720 and (c) A960 for both simulation and calculation.

Table 5-1 shows the simulated sensitivity in fF/g for accelerometers A640 which has a proof mass size of $640\ \mu\text{m} \times 640\ \mu\text{m}$. Up to 10g acceleration was applied on top of 1g during the simulation. C_0 is the rest capacitance = 0.55 pF and ΔC is the change in capacitance between the proof mass and the bottom electrode. A720 has a proof mass size of $720\ \mu\text{m} \times 720\ \mu\text{m}$ and it is the medium size device

Table 5-1 Simulated sensitivity of A640

Acceleration	Displacement (μm)	Simulated capacitance (pF)	Simulated ΔC (pF)	Simulated $\Delta C/C_0$	Simulated sensitivity (fF/g)
1g	1.19×10^{-01}	5.46×10^{-01}	----	----	
1g + 1g	2.38×10^{-01}	5.54×10^{-01}	8.38×10^{-03}	1.53%	8.38
1g + 2g	3.56×10^{-01}	5.63×10^{-01}	1.70×10^{-02}	3.11%	8.51
1g + 5g	7.12×10^{-01}	5.91×10^{-01}	4.47×10^{-02}	8.18%	8.94
1g + 10g	1.30×10^{00}	6.43×10^{-01}	9.74×10^{-02}	17.84%	9.74

Table 5-2 Simulated sensitivity of A720

Acceleration	Displacement (μm)	Simulated capacitance (pF)	Simulated ΔC (pF)	Simulated $\Delta C/C_0$	Simulated sensitivity (fF/g)
1g	1.39×10^{-01}	6.89×10^{-01}	----	----	
1g + 1g	2.78×10^{-01}	7.01×10^{-01}	1.25×10^{-02}	1.81%	12.52
1g + 2g	4.17×10^{-01}	7.14×10^{-01}	2.55×10^{-02}	3.71%	12.76
1g + 5g	8.33×10^{-01}	7.56×10^{-01}	6.76×10^{-02}	9.82%	13.53
1g + 10g	1.52×10^{00}	8.39×10^{-01}	1.50×10^{-01}	21.81%	15.02

Table 5-3 Simulated sensitivity of A960

Acceleration	Displacement (μm)	Simulated capacitance (pF)	Simulated ΔC (pF)	Simulated $\Delta C/C_0$	Simulated sensitivity (fF/g)
1g	2.21×10^{-01}	1.26×10^{00}	----	----	
1g + 1g	3.54×10^{-01}	1.28×10^{00}	1.33×10^{-02}	1.05%	13.32
1g + 2g	5.53×10^{-01}	1.31×10^{00}	4.63×10^{-02}	3.67%	23.16
1g + 5g	1.33×10^{00}	1.45×10^{00}	1.84×10^{-01}	14.59%	36.89
1g + 10g	2.69×10^{00}	1.88×10^{00}	6.15×10^{-01}	48.65%	61.50

among the three. Simulated results are shown in Table 5-2. The rest capacitance of A720 is 0.69 pF. A960 has proof mass size of $960 \mu\text{m} \times 960 \mu\text{m}$ and it is the largest device among the three. Simulated results are shown in Table 5-3. The rest capacitance of A960 is 1.26 pF. The calculated values for change in capacitance and sensitivity for A640, A720 and A960 are shown in Tables 5.4, 5-5 and 5-6, respectively. The normalized change in capacitance for each of the accelerometer vs the applied acceleration is

Table 5-4 Calculated sensitivity of A640

Acceleration	Displacement (μm)	Calculated capacitance (pF)	Calculated ΔC (pF)	Calculated $\Delta C/C_0$	Calculated sensitivity (fF/g)
1g	1.19×10^{-01}	4.42×10^{-01}	----	----	
1g + 1g	2.38×10^{-01}	4.50×10^{-01}	7.78×10^{-03}	1.76%	7.78
1g + 2g	3.56×10^{-01}	4.59×10^{-01}	1.58×10^{-02}	3.58%	7.92
1g + 5g	7.12×10^{-01}	4.85×10^{-01}	4.18×10^{-02}	9.44%	8.36
1g + 10g	1.30×10^{00}	5.35×10^{-01}	9.20×10^{-02}	20.78%	9.20

Table 5-5 Calculated sensitivity of A720

Acceleration	Displacement (μm)	Calculated capacitance (pF)	Calculated ΔC (pF)	Calculated $\Delta C/C_0$	Calculated sensitivity (fF/g)
1g	1.39×10^{-01}	5.62×10^{-01}	----	----	
1g + 1g	2.78×10^{-01}	5.74×10^{-01}	1.16×10^{-02}	2.07%	11.63
1g + 2g	4.17×10^{-01}	5.86×10^{-01}	2.37×10^{-02}	4.23%	11.87
1g + 5g	8.33×10^{-01}	6.25×10^{-01}	6.33×10^{-02}	11.26 %	12.66
1g + 10g	1.52×10^{00}	7.04×10^{-01}	1.42×10^{-01}	25.27%	14.20

Table 5-6 Calculated sensitivity of A960

Acceleration	Displacement (μm)	Calculated capacitance (pF)	Calculated ΔC (pF)	Calculated $\Delta C/C_0$	Calculated sensitivity (fF/g)
1g	2.21×10^{-01}	1.01×10^{00}	----	----	
1g + 1g	3.54×10^{-01}	1.03×10^{00}	2.01×10^{-02}	2.00%	20.18
1g + 2g	5.53×10^{-01}	1.06×10^{00}	5.20×10^{-02}	5.14%	26.00
1g + 5g	1.33×10^{00}	1.21×10^{00}	1.97×10^{-01}	19.49%	39.41
1g + 10g	2.69×10^{00}	1.59×10^{00}	5.80×10^{-01}	57.33%	57.97

depicted in Figure 5-5. The calculated capacitance values are obtained considering a fixed area A_{eff} (plate area excluding the perforations) for both electrodes using Eq. (2-6). The gaps between the plates were calculated by subtracting the displacement of the proof mass from the initial gap of 7 μm . The simulated capacitance values obtained from CoventorWare[®] are higher since the bottom electrode is not perforated which results in higher effective area during simulations. Therefore, the normalized simulated sensitivity values are lower than the calculated ones in Figure 5-5. At high acceleration, the calculated and the simulated values deviate more due to the non-linear behavior of the accelerometers. Non-linearity in the case of A960 is higher than the other accelerometers. The trend was well-fitted with a second order polynomial, as shown in Table 5-7. The improvement in the capacitive sensitivity due to the quadratic dependence of capacitance change on acceleration in Figure 5-5 is a trade-off against its nonlinearity. To assess the nonlinearity, first we define capacitive sensitivity S_{cap} as:

$$S_{cap} = \partial(\Delta C/C)/\partial a \quad (5-1)$$

The nonlinearity is quantified as:

$$Nonlinearity = \frac{S_{cap}|_{a=1g+10g} - S_{cap}|_{a=1g+1g}}{S_{cap}|_{a=1g+1g}} \quad (5-2)$$

When Eqs. (5-1) and (5-2) are operated on the simulated results in Figure 5-5, it is found that A960 delivers $\times 4.7$ sensitivity improvement at 10g compared to 1g applied on top of the gravitational acceleration, at the expense of 370% nonlinearity. Both sensitivity improvement and nonlinearity are much less for the smaller accelerometers. The results are compiled in Table 5-7.

Table 5-7 Trade –off Between Nonlinearity and Sensitivity in Simulated Capacitance Change

	Quadratic Model for Normalized Capacitance Change	Nonlinearity at 1g+10g	Sensitivity Improvement at 1g+10g
A960	$3.95 \times 10^{-05} a^2 + 3.34 \times 10^{-04} a - 9.69 \times 10^{-03}$	370%	$\times 4.7$
A720	$6.31 \times 10^{-06} a^2 + 1.46 \times 10^{-03} a - 1.17 \times 10^{-02}$	65%	$\times 1.7$
A640	$4.03 \times 10^{-06} a^2 + 1.33 \times 10^{-03} a - 1.18 \times 10^{-02}$	65%	$\times 1.7$

Due to the lower spring stiffness and the higher proof-mass associated with A960, higher displacement is possible. In the case when this displacement becomes comparable to the spring thickness, response becomes significantly nonlinear [228], due to the non-uniform gap between the proof-mass and the bottom electrode. Higher deflection improves the sensitivity at the cost of nonlinearity.

5.3.2 Spring constant

Spring constant for each accelerometer was calculated from Eq. (2-3). When the proof mass gets displaced because of the applied acceleration, some portion of the connected springs also gets displaced from the equilibrium position. To take this into account, one-third of the total mass of the four springs were also added with the actual proof mass to obtain m .

Bias was applied to the capacitive microaccelerometer in CoventorWare® to measure the induced charge and therefore, capacitance. This bias also induced an electrostatic force between two parallel charged plates which is given by Eq. (5-3) [229]

$$F_e = \frac{\epsilon_{air} A_{eff} V^2}{2d^2} \quad (5-3)$$

where, ϵ_{air} = permittivity of air, V = applied voltage between the plates and d = gap between the plates.

The total force was calculated by adding the weight of the proof mass (including one-third of the spring mass) and F_e . The total force was then plotted against corresponding simulated displacement and the spring constant was calculated from the slope of those curves as shown in Figure 5-6. The points represent the various amounts of applied accelerations shown in Tables 5-1, 5-2 and 5-3. The spring constants thus obtained for A640, A720 and A960 are 2.28 N/m, 2.25 N/m and 2.11 N/m, respectively. This implies that the largest accelerometer A960 is less rigid than the other two accelerometers. Therefore, upon the application of the same amount of acceleration, A960 will demonstrate the highest displacement as well as sensitivity which is evident from Tables 5-1 to 5-6. The largest accelerometer A960 is of particular interest in terms of bending and stress at different layers since it showed the smallest spring constant and highest sensitivity

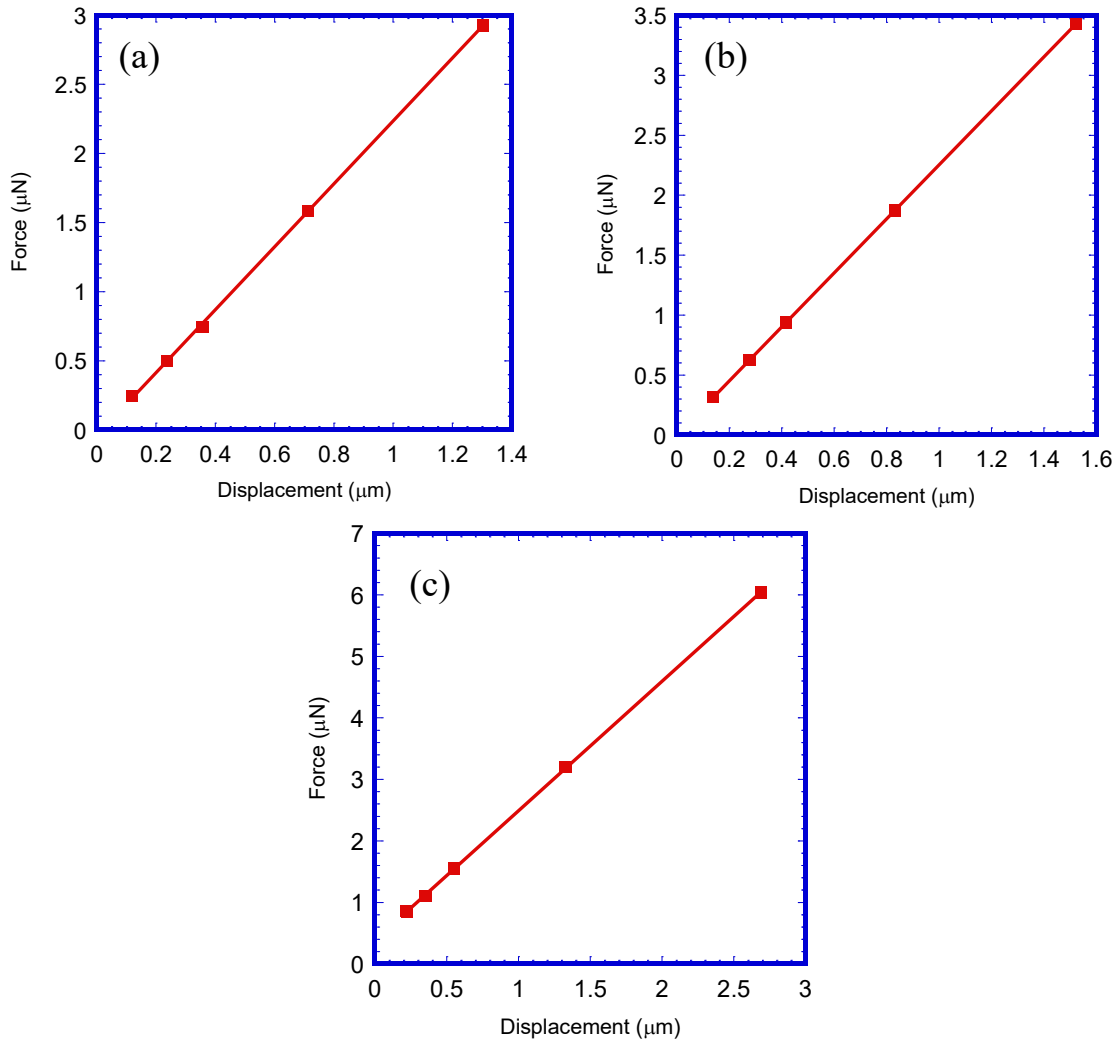


Figure 5-6 Total force vs displacement for (a) A460, (b) A720 and (c) A960

5.3.3 Resonant frequency

Modal analyses on all three different accelerometers were carried out to determine different

Table 5-8 Modal frequencies for different accelerometers

Modes	Frequency of A640 (Hz)	Frequency of A720 (Hz)	Frequency of A960 (Hz)
1	1.18×10^3	9.71×10^2	6.17×10^2
2	1.26×10^4	1.24×10^4	1.19×10^4
3	3.77×10^4	3.35×10^4	2.69×10^4
4	8.13×10^4	6.72×10^4	3.78×10^4
5	8.75×10^4	7.37×10^4	4.35×10^4
6	9.53×10^4	8.42×10^4	7.05×10^4

modes of vibration. The devices were simulated for six different modes. The six modal frequencies for all the devices are listed in Table 5-8.

It is desired that the first modal frequency, which is a resonance frequency of the device, represents the movement along the z-axis and dominates over all other modes. Connection of four springs at the corners of the square proof mass and optimization the spring dimensions confirmed negligible lateral movement of the proof mass under vertical acceleration. Figure 5-7(a) shows the first modal displacement of A640 in vertical direction while the others represent the remaining modes of the six modal frequencies mentioned in Table 5-4. The generalized displacements for different modes are also shown in Figure 5-8. Each of these plots shows that the first modal displacement is approximately three orders higher than others and also the first modal frequency is much lower than other frequencies. This

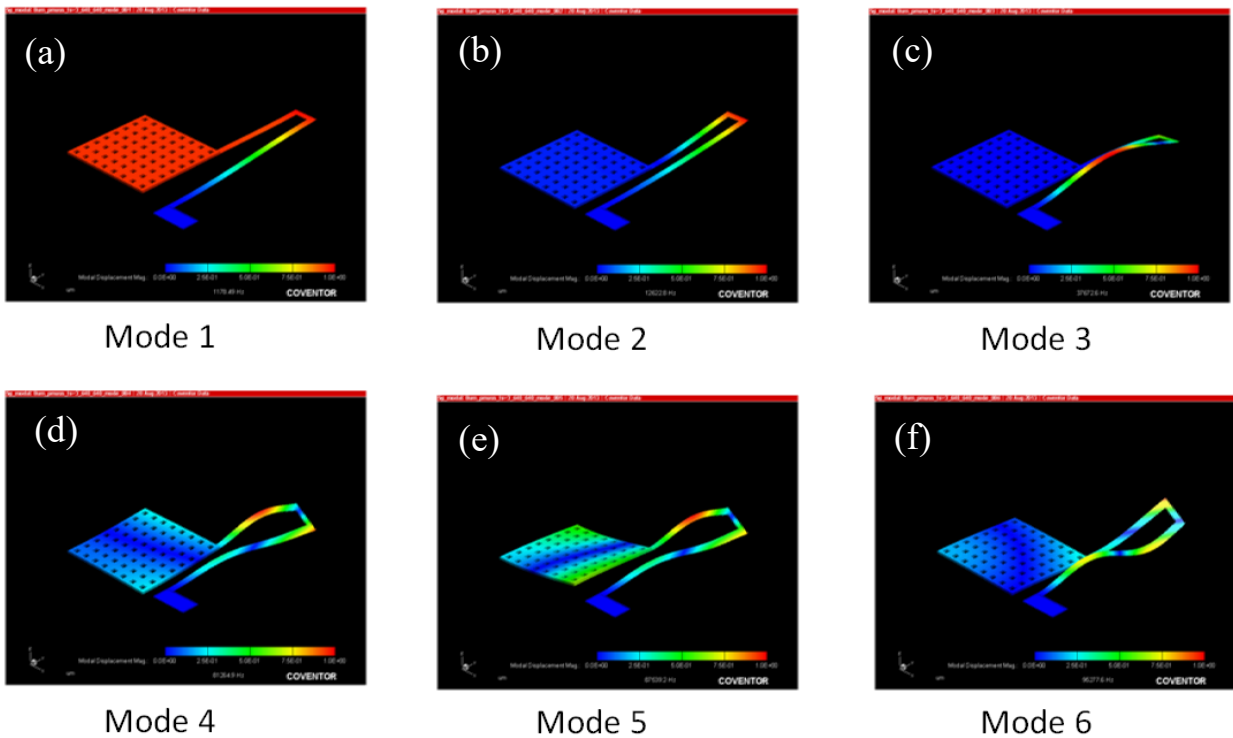


Figure 5-7 Six modes of the accelerometer A640. (a) Mode 1 displaying desired vertical movement and (b)-(f) other high frequency vibration modes.

modal analysis indicates that the possibility of arising fluctuations from other mode is very low due to huge gap between the first mode and the immediate following mode for all the accelerometer types. The first mode contains motion in preferred z-direction whereas the other modes contain motion in random directions.

5.3.4 Bending and stress

To simulate the bending capability of the accelerometers, displacement was applied on a side of the substrate while keeping the opposite side fixed in all directions. The ROC was calculated from the coordinates of the bent substrate. A960 was bent down to 2.5 cm ROC by applying 4.4 μm displacement on one side of the substrate, as depicted in Figure 5-9. All the layers of the accelerometer experience

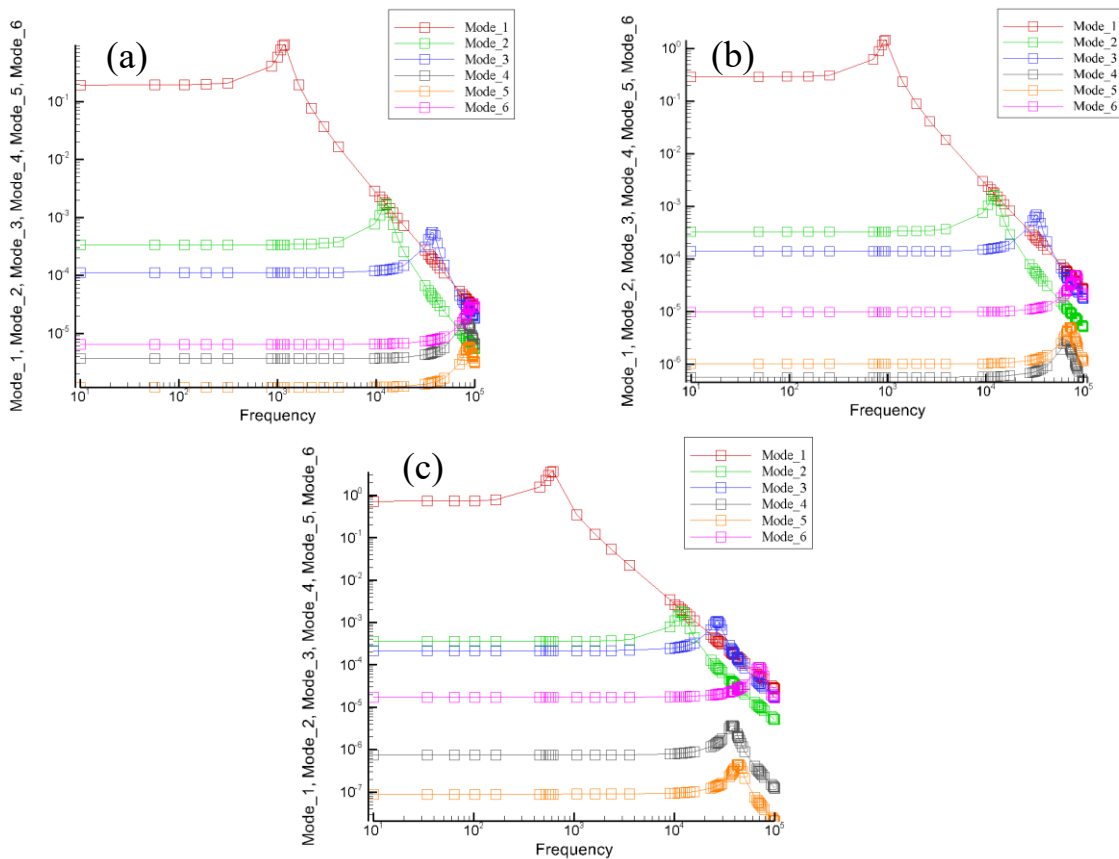


Figure 5-8 Modal displacements for (a) A640, (b) A720 and (c) A960 devices

stress upon bending. The maximum layer stresses of Au and Ni proof mass layer are 207.38 MPa and 187.13 MPa while the yield strengths of these layers are 400 MPa [230], 330-450 MPa [231], [232]. The stress results for all the accelerometers are summarized in Table 5-9. In all cases, the maximum stress level is smaller than the respective yield strength.

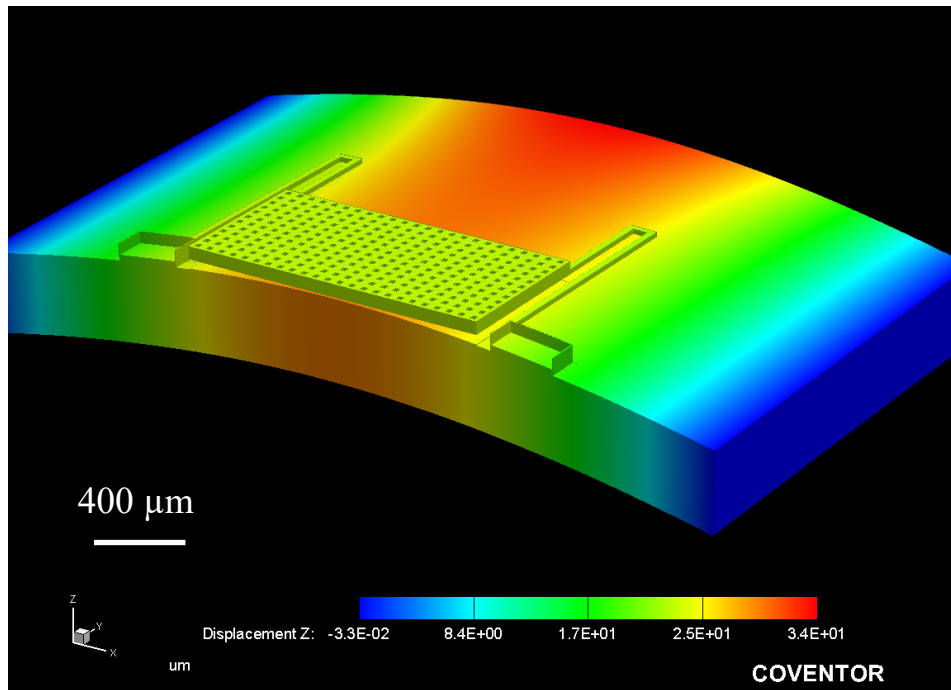


Figure 5-9 A960 bent down to 2.5 cm ROC upon application of 4.4 μm displacement on one side of the substrate

Table 5-9 Maximum stress at the seed layer and the springs for different accelerometers

	Maximum stress on Au seed layer (MPa)	Maximum stress on Ni springs (MPa)
A960	207.358	187.13
A720	203.66	149.76
A640	198.68	142.44
Yield strength (MPa)	400	330-450

The location of the maximum stress is always the edge of the respective layer where it is connected at the anchor. As shown in Figure 5-10 and Fig 5-11, the maximum stress point lies at the very edge of the Au seed layer and Ni proof mass layer, respectively.

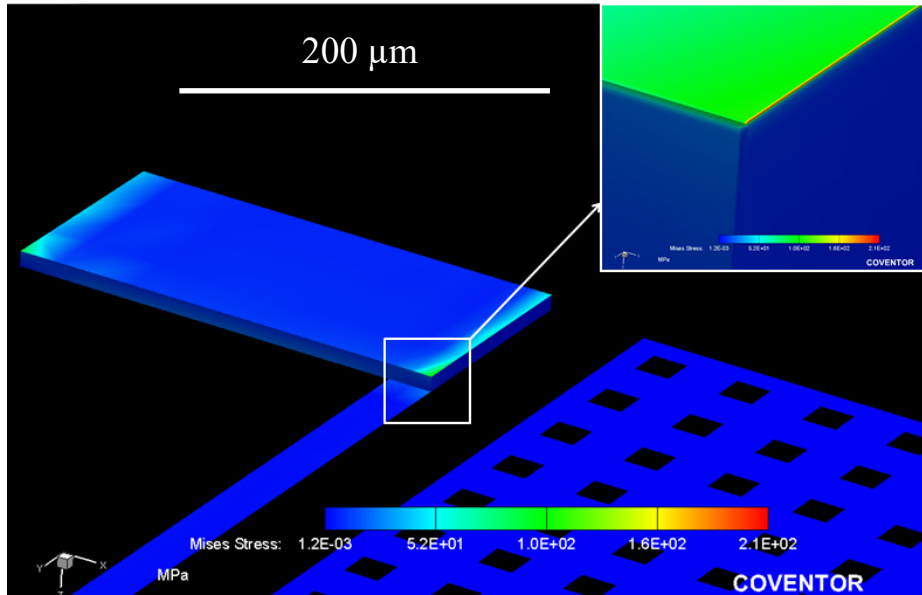


Figure 5-10 Maximum stress location of Au seed layer of A960

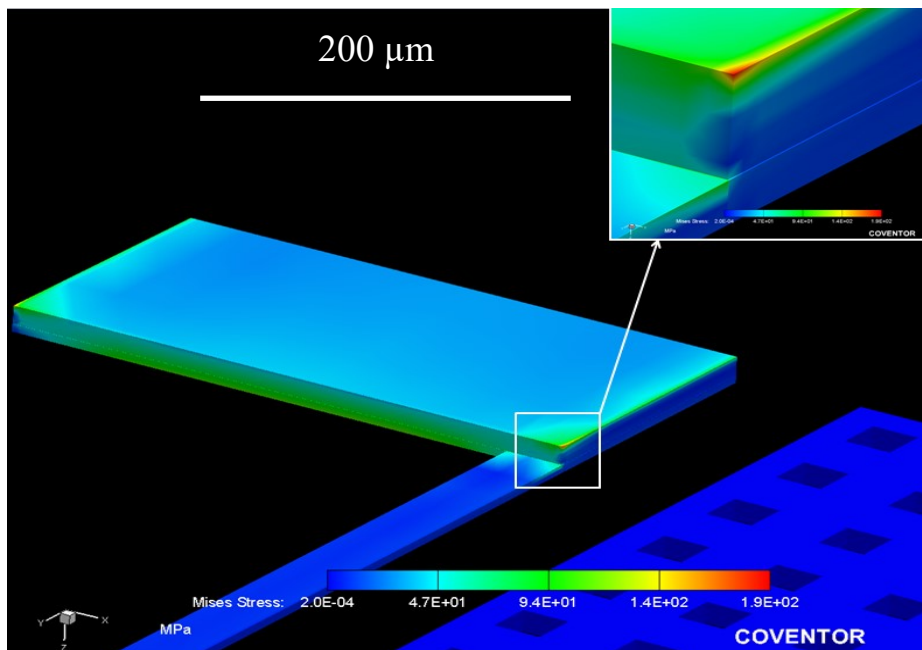


Figure 5-11 Maximum stress location of Ni proof mass layer of A960

5.3.5 Pull-in analysis

Pull-in analysis was carried out to confirm that the applied voltage is less than the pull-in voltage. Above the pull-in point the electrostatic force will be greater than the mechanical restoring force and therefore, the top movable structure will collapse. The pull-in voltage V_{pi} is given by [233]

$$V_{pi} = \sqrt{(8kd^3)/(27\epsilon_{air}A_{eff})} \quad (5-2)$$

The calculated pull-in voltage of A640, A720 and A960 are 19.77, 18.60 and 17.51 V whereas the simulated pull-in voltages for the same devices are 17.5 V, 14.5 V and 11.0 V, respectively. After complete fabrication, hogging at the center of the proof mass was observed and the modified gap between the top and bottom electrode was used to simulate the pull-in voltage again which is discussed later.

5.4 Fabrication

This section describes the fabrication steps of the flexible accelerometers in details. Figure 5-12 shows the complete fabrication process flow of the accelerometer on flexible substrate.

- **Passivation layer deposition**

The fabrication started with a deposition of 0.5 μm thick Si_3N_4 passivation layer on a bare and clean Si wafer. AJA sputtering system was utilized at 2.8 mT chamber pressure and 150 W RF power under 5 sccm N_2 and 30 sccm Ar gas flow for 6 hours. The rate of the deposition of Si_3N_4 was 0.083 $\mu\text{m}/\text{hour}$.

- **Release layer deposition**

A polyimide tape was wrapped around the perimeter of the Si carrier wafer to prevent the PI2611 release layer from coating the perimeter of the wafer. Then, liquid polyimide PI2611 was spin coated at 3000 rpm for 30 seconds on top of the carrier wafer to obtain the desired thickness of 10 μm , and the tape

was removed after spin coating, leaving the Si_3N_4 layer uncoated with PI2611 around the perimeter. The polyimide was soft baked at $130\text{ }^\circ\text{C}$ for 90 seconds and cured at $350\text{ }^\circ\text{C}$ for 30 minutes.


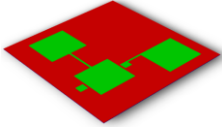
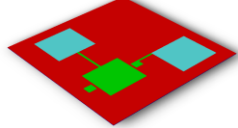
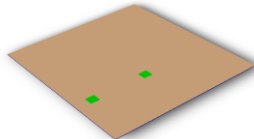
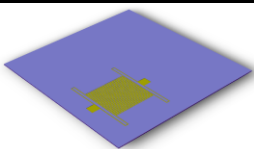
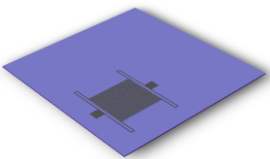
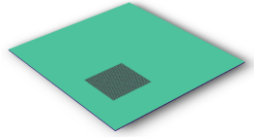
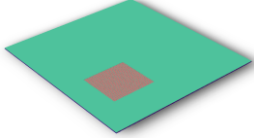
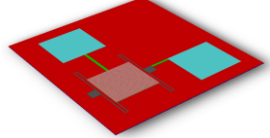
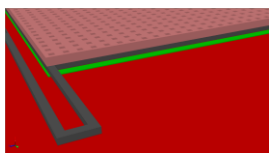
	Process steps	Schematics
(a)	Polyimide deposition on Si wafer as a flexible substrate.	
(b)	Sputtering of insulation layer. Deposition and patterning of bottom electrode ($0.5\text{ }\mu\text{m}$).	
(c)	Deposition and patterning of bond pads (Another $0.5\text{ }\mu\text{m}$). A total of $1\text{ }\mu\text{m}$ of Al for bond pads.	
(d)	Spin-on polyimide sacrificial layer and cure ($7\text{ }\mu\text{m}$). Patterning to make openings at anchor locations.	
(e)	Au deposition (100 nm). Spinning of the 1 st mold layer ($5\text{ }\mu\text{m}$). Patterning to define the proof mass and the springs	
(f)	1 st Ni electroplating to form the proof mass and the springs ($3\text{ }\mu\text{m}$)	
(g)	Removing 1 st mold layer. Spinning of the 2 nd mold layer ($10\text{ }\mu\text{m}$). Alignment and patterning to define the proof mass.	
(h)	2 nd Ni electroplating to thicken the proof mass ($5\text{ }\mu\text{m}$). A total of $8\text{ }\mu\text{m}$ Ni for the proof mass.	
(i)	Removing the 2 nd mold layer. Etching Au seed layer. Ashing the sacrificial polyimide in O_2 to suspend the accelerometers.	
(j)	Accelerometer after complete ashing (exaggerated 5 times along vertical axis).	

Figure 5-12 The complete fabrication process flow of the accelerometers on flexible substrate utilizing double UV-LIGA process. (Not to scale).

- **Flexible substrate deposition**

The fabrication of the flexible substrate was achieved by employing four successive coatings of the PI 5878G polyimide. For each layer, a three-step spin was adopted to reach a final spin speed of 1500 rpm with 500 rpm increments with a ramp rate of 100 rpm/second. After each spin coating, the layer was soft baked at 110 °C for 3 minutes and then cooled down to room temperature. Following the coating process, the polyimide was cured in N₂ atmosphere at 300 °C for 4 hours with ramp up and ramp down times of 3 hours and 3 hours, respectively, resulting in a final thickness of approximately 35 μm.

- **Insulation layer deposition**

Another 0.5 μm thick layer of sputtered Si₃N₄ was deposited which serves as an isolation layer between the substrate and the device. It also promotes adhesion between the underlying polyimide and the subsequent layers. The process condition was the same as the previous sputtering of Si₃N₄.

- **Bottom electrode and bond pad formation**

Lift-off technique was deployed for patterning the bottom electrode and the bond pad. At first, negative polarity lift-off photoresist, NR-9 1500PY was spin coated in a two-step process, 500 rpm for 5 seconds followed by 2500 rpm for 40 seconds. Coated photoresist was baked at 150 °C for 1 minute followed by UV exposure using the OAI aligner for 16.5 seconds. The intensity of the light source was previously checked and it was set at 20 mW/cm². The resist was then baked at 100 °C for 1 minute and developed in a RD-6 developer for 14 seconds.

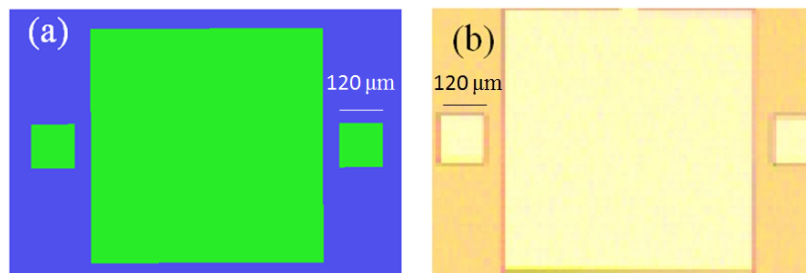


Figure 5-13 Bottom electrode patterning (a) modeled and (b) fabricated

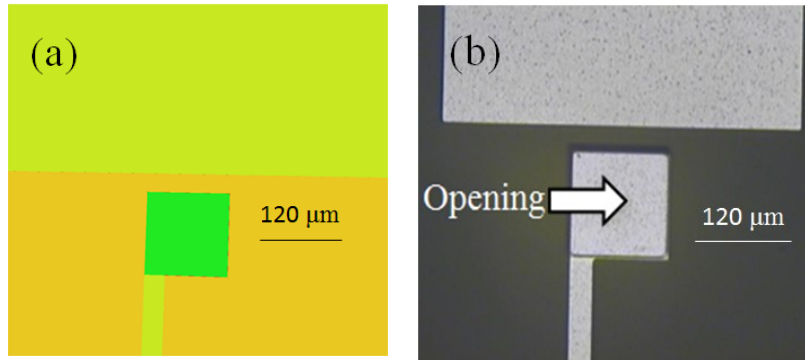


Figure 5-14 Cured sacrificial layer has openings at anchors (a) modeled and (b) fabricated

Al was then deposited with the sputtering tool. The desired thickness of the bottom electrode was $0.5\ \mu\text{m}$ and the rate of Al deposition was $8\ \text{nm/minute}$. Therefore, the duration for this deposition was for 63 minutes at a pressure of $2.8\ \text{mT}$, using 150W DC power under $30\ \text{sccm}$ of Ar flow. The resist was finally developed in 1165 solvent to achieve the patterned bottom electrode layer on top of the substrate as shown in Figure 5-13.

After defining the bottom Al layer, the bond pad area was patterned similarly with the bond pad mask. The bond pad area was opened and then another $0.5\ \mu\text{m}$ layer of Al was deposited to make the bond pad area thicker.

- **Sacrificial layer deposition**

As the sacrificial layer, HD 4104 (HD Microsystems) negative polarity photo definable polyimide

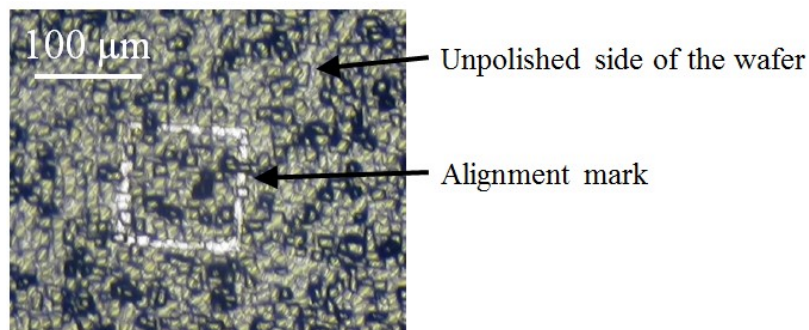


Figure 5-15 Backside alignment mark under the device wafer

was used. A two-step spin coating, 500 rpm (100 rpm/second) for 5 seconds followed by 2000 rpm (500 rpm/second) for 50 seconds, was implemented with a bake at 100 °C for 3 minutes afterwards. The polyimide was exposed with 126.5 mJ/cm² energy after aligning the sacrificial mask with respect to metallization layer. A four-step development procedure was employed using PA 401D developer (HD Microsystems) for 35 seconds, 1:1 PA 401 D: PA 400 R for 30 seconds and two different baths of PA 400 R rinse for 15 seconds each.

Polyimide curing was done in N₂ gas ambient by ramping up the temperature to 200 °C in 1 h, with a dwell time of 30 minutes at that temperature followed by a ramp up to a peak temperature of 300°C and keeping it there for 1 h before cooling down to room temperature in 2 hours to obtain a final thickness of 7 μm. Figure 5-14 shows the anchor after curing the polyimide.

- **Patterning backside alignment mark**

The backside alignment marks are required to align the device wafer with the encapsulation wafer before wafer bonding process. For the fabrication, first NR-9 1500 PY was spin coated and patterned as described before for bottom electrode patterning. The cavity alignment marks are to be aligned with the bottom Al. Therefore, the bottom Al mask was used to form the same pattern on the backside of the device wafer. Sputter deposition technique was used to deposit 0.5 μm Al on the backside of the wafer. The lift-off process was completed by removing the resist in 1165 resist remover. Figure 5-15 shows the final alignment mark after removing the resist. Since the backside is not polished, the marks also became grainy but still detectable.

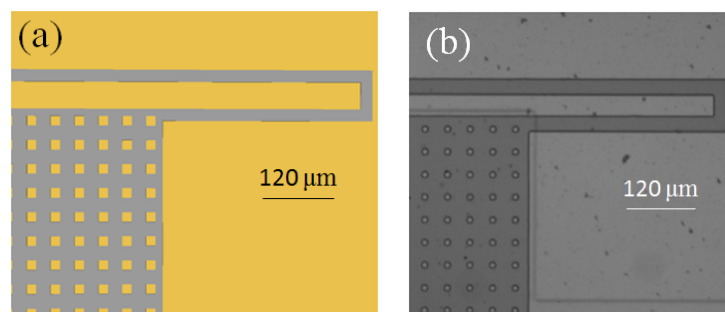


Figure 5-16 Patterns after first Ni electroplating and mold resist removal (a) modeled and (b) fabricated.

- **Seed layer formation**

A 100 nm thick layer of Au was deposited to serve as a seed layer using an e-beam evaporator. This seed layer defines the locations of proof mass growth.

- **Mold resist deposition**

As the mold photoresist, SU-8 was used. The photoresist was first spin coated using a two-step process, 600 rpm for 5 seconds followed by 4000 rpm (1500 rpm/second) for 40 seconds. Resist was pre-baked at 150 °C for 1 minute and exposed with 670 mJ/cm² energy. After a post exposure bake for 3 minutes at 80°C, the photoresist was developed in RD-6 developer for 50 seconds to give a final thickness of approximately 5 μm which provided sufficient thickness to grow a 3 μm thick layer of Ni.

- **Electroplating proof mass**

Ni electroplating was performed at a temperature of 45°C for 45 minutes at a current density of 15 mA/cm². The target Ni thickness was 3 μm for the first layer. The springs after the Ni electroplating

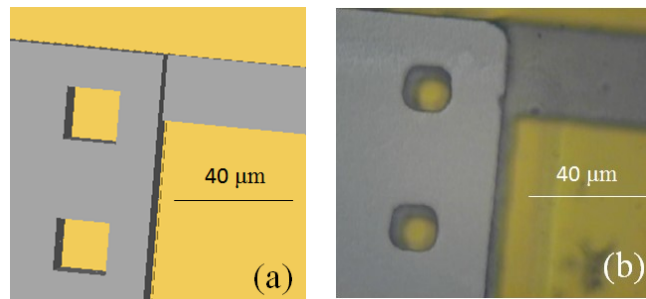


Figure 5-17 Pattern after seconds Ni electroplating and mold resist removal (a) modeled and (b) fabricated.

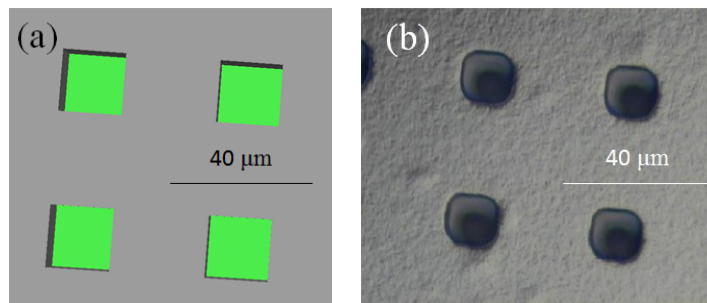


Figure 5-18 Proof mass after Au etching (a) modeled and (b) fabricated

and mold removal are shown in Figure 5-16.

- **Second mold resist patterning**

A second layer of mold (10 μm) was spin-coated and patterned a similar procedure like the first mold resist. This mold layer is critical because it must be aligned properly to the underlying first Ni layer and any misalignment will result in reduction of the hole size.

- **Second Ni electroplating**

Second layer of Ni electroplating was performed at the same temperature of 45 $^{\circ}\text{C}$ for 45 minutes at a current density of 15 mA/cm^2 to obtain 5 μm of additional Ni on top of the first Ni layer. This layer was only electroplated over the central proof mass making the spring layer thinner than the proof mass. Once the electroplating was completed, the mold was removed. Using Trion reactive ion etcher (RIE), Au etching was carried out so that the ashing gas can come into contact with the sacrificial polyimide in the subsequent ashing step. Figure 5-17 and Figure 5-18 show the wafer after removing the mold and after Au etching, respectively. Later, imaging using scanning electron microscope (SEM) and identifying the elemental composition using energy dispersive x-ray (EDX) were done to confirm that no Au was remaining there. Figure 5-19(a) shows the EDX result after Au etching. No trace of Au was observed. EDX was again done after complete ashing to confirm that there is no remaining polyimide as shown Figure 5-19(b).

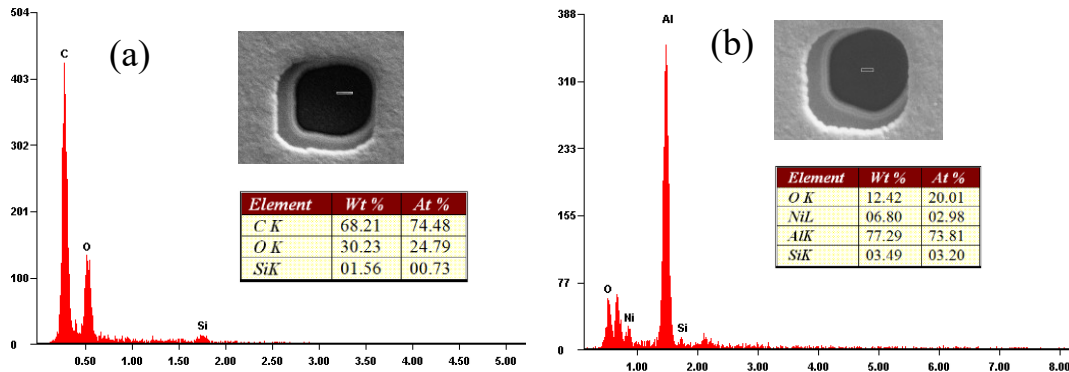


Figure 5-19 EDX completed inside the holes (a) after Au etching and (b) after ashing

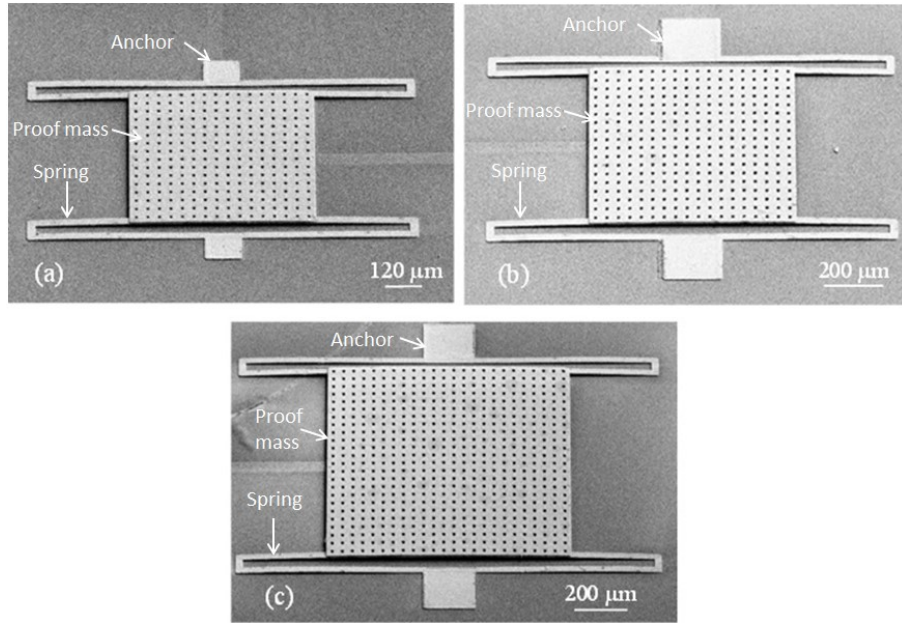


Figure 5-20 Accelerometers (a) A640, (b) A720 and (c) A960 after complete ashing of the sacrificial layer

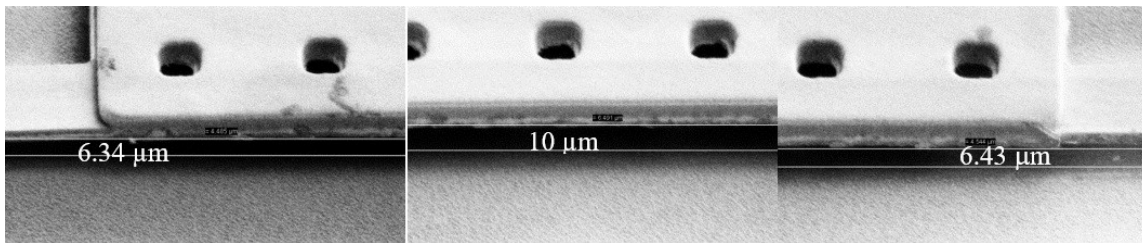


Figure 5-21 SEM images of A720, tilted at 45 °angle, illustrating bowing of the proof-mass due to residual stress. Left and right photos show the respective edges of the proof-mass connecting to the springs while the center photo is taken at the center of the proof mass. Although the average gap was ~7 m as designed, it varied from ~6.4 to 10 m for each accelerometer from the springs to the proof mass center.

- **Ashing of sacrificial layer**

The last step of the fabrication is ashing the sacrificial layer. This step was carried out in Diener asher system using O₂ as the ashing gas for 150 hours under a pressure of 1 mBar. After complete ashing, the accelerometers became suspended and connected to the substrate only with the springs as shown in Figure 5-20. The perforations are visible in all cases. The proof mass is of two layers of Ni which is perceivable from Figures 5-20 and 5-21. The connection line to the bond pad is taken out from the bottom electrode which is also evident from the Figure 5-20. The SEM was used to take several pictures of the resultant device. It was observed that because of stress in the Ni layer, the proof mass became curved and

the gap under it varied from center to the edge as illustrated in Figure 5-21. This phenomenon was taken into account to reevaluate the pull-in voltage of the accelerometers.

- **Wire bonding**

Wire bonding was done on a separate package after peeling off a die from the carrier wafer. As mentioned previously that the substrate was deposited under a low strength release layer PI2611, the die can be peeled off from the wafer with the help of a sharp cutting tool. After releasing, the die was carefully placed inside a quad flat package (QFP). A double-sided tape was used as an adhesive. Indium (In) was soldered to make Au wire bonding on the bond pads.

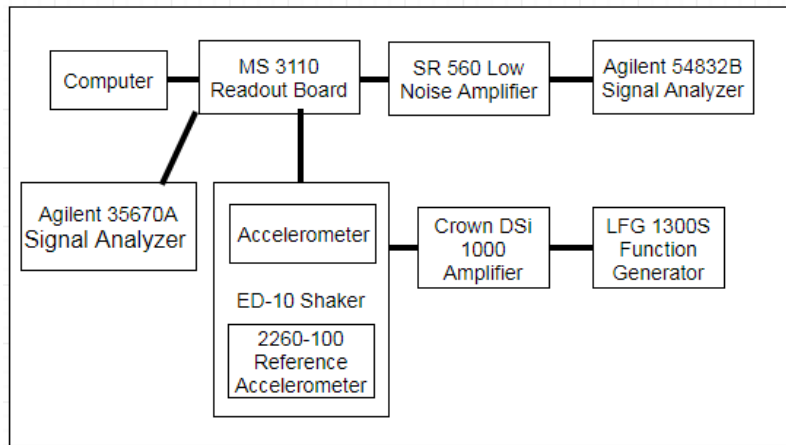


Figure 5-22 Block diagram of the setup for characterization

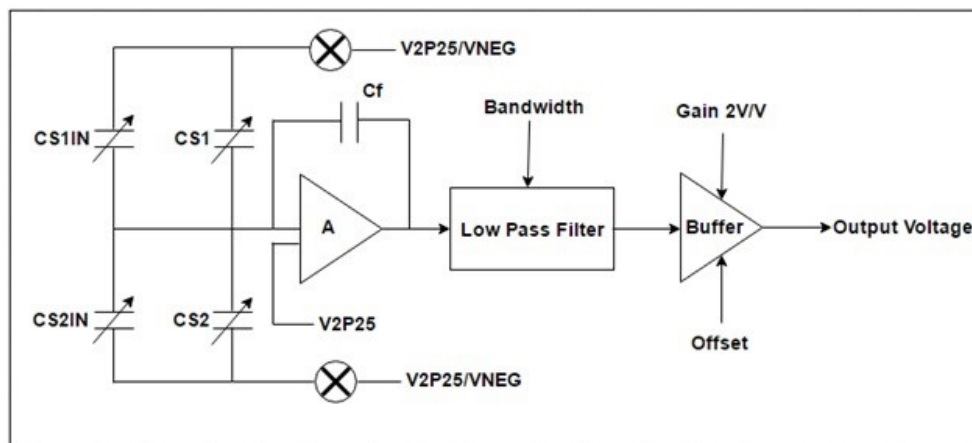


Figure 5-23 Functional block diagram of the MS 3110 readout circuit (redrawn with the permission from Irvine Sensors)

5.5 Performance characterization

5.5.1 Characterization setup

Once the device was packaged, it was mounted on a shaker driven by a function generator via an amplifier. MS3110 capacitor read-out circuit converted the capacitance induced between the bottom electrode and the proof mass into voltage. A reference accelerometer Si Designs 2260-100 with a sensitivity of 40mV/g, frequency range of 2.50 kHz and acceleration range ± 100 g was also mounted on the shaker. The block diagram of the measurement setup is shown in Figure 5-22. The functional block diagram of MS3110 readout circuit [234] is displayed in Fig 5-23. C_f is the feedback capacitor and its value was set at 5.13 pF to obtain a scale factor of $\sim 1\text{V/pF}$ for MS3110. The reference voltage and gain were set at 0.5 V and 2V/V, respectively. C_{S1} and C_{S2} are the balance capacitors which can be changed using the software. The purpose of these balance capacitors is to eliminate the parasitic capacitance of the device. The device was connected to C_{S1IN} while C_{S2IN} was left open. The transfer function of the readout circuit is [234]

$$V_{out} = Gain \times V_{2P25} \times 1.14 \times (C_{S2T} - C_{S1T})/C_f + V_{ref} \quad (5-3)$$

where, V_{2P25} is a reference test voltage set at 2.25 V, $C_{S1T} = C_{S1} + C_{S1IN}$, $C_{S2T} = C_{S2} + C_{S2IN}$ and V_{out} is the output voltage. The change in capacitance was then obtained from $\Delta C_T = C_{S2T} - C_{S1T}$.

5.5.2 Accelerometer on a flat surface

5.5.2.1 Sensitivity

Figure 5-24 shows the time domain responses of the devices A640, A720 and A960 at 1080 Hz, 1020 Hz and 800 Hz at which the device output sensitivity was found to be the highest. From the reference accelerometer response, the instantaneous acceleration was computed and plotted against the fabricated accelerometer output voltage. Finally, the change in the device capacitance was calculated for each instant using Eq. (5-3). As seen in Figure 5-25, the response is near linear with minimal hysteresis. The measured sensitivities for A640, A720 and A960 are 146 fF/g, 165 fF/g and 187 fF/g, respectively.

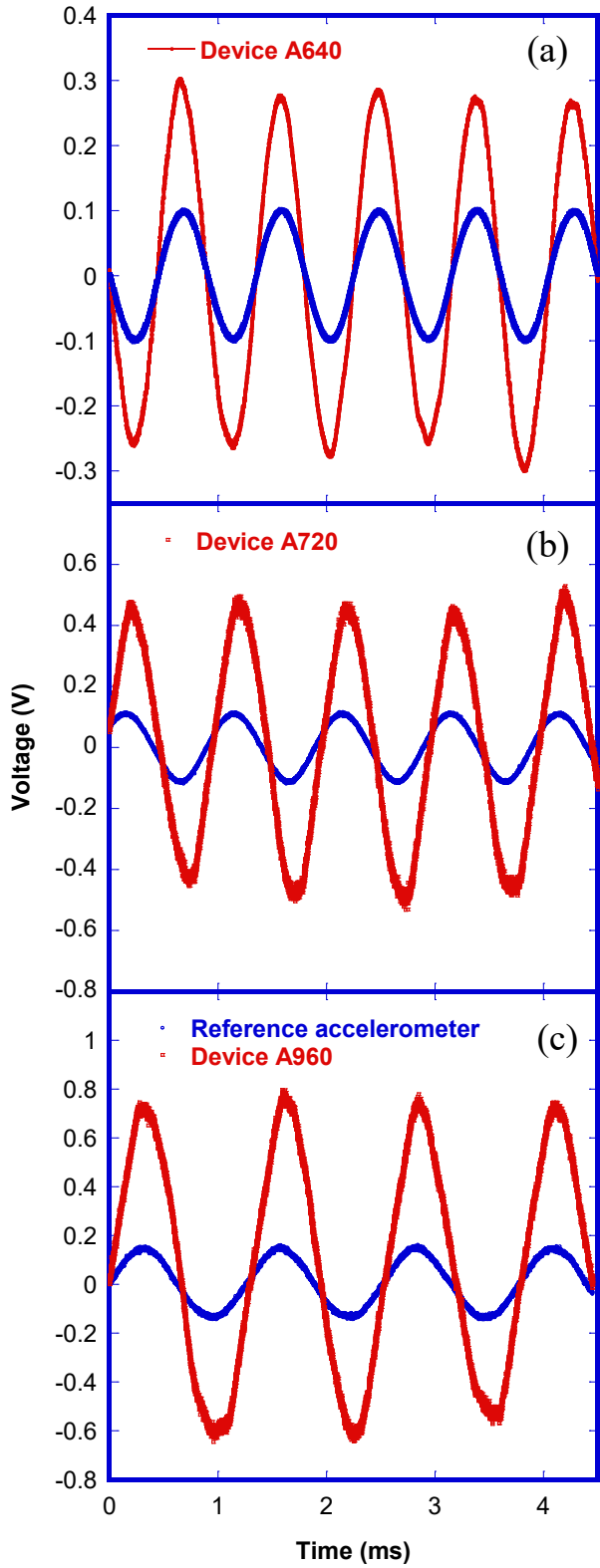


Figure 5-24 Time domain response of (a) A640 at 1080 Hz, (b) A720 at 1020 Hz and (c) A960 at 800 Hz.

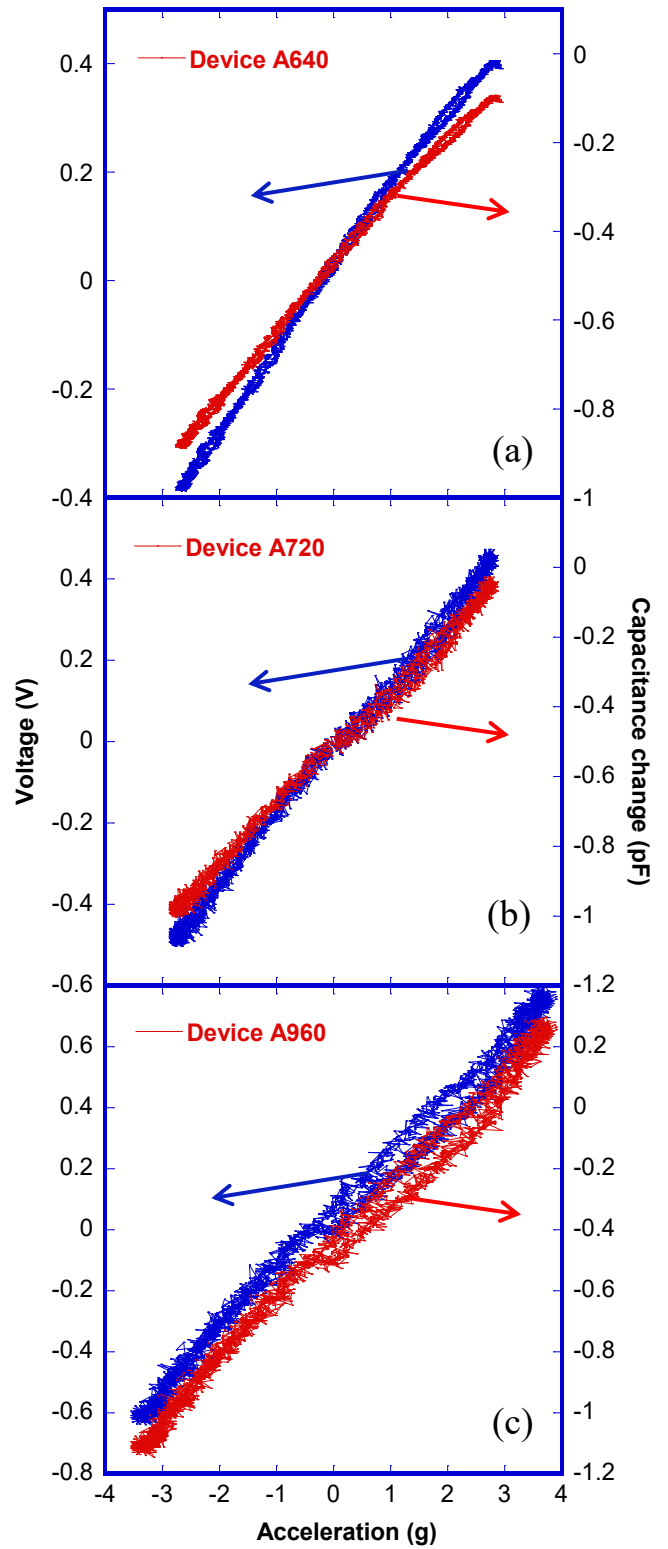


Figure 5-25 Voltage response and change in capacitance for (a) A640 at 1080 Hz, (b) A720 at 1020 Hz and (c) A960 at 800 Hz

5.5.2.2 Frequency response

The frequency of vibrations was varied from 700 Hz to 1.5 kHz for all the accelerometers. Different accelerations, up to 4g, were applied. The responses from the accelerometers on flat surface are

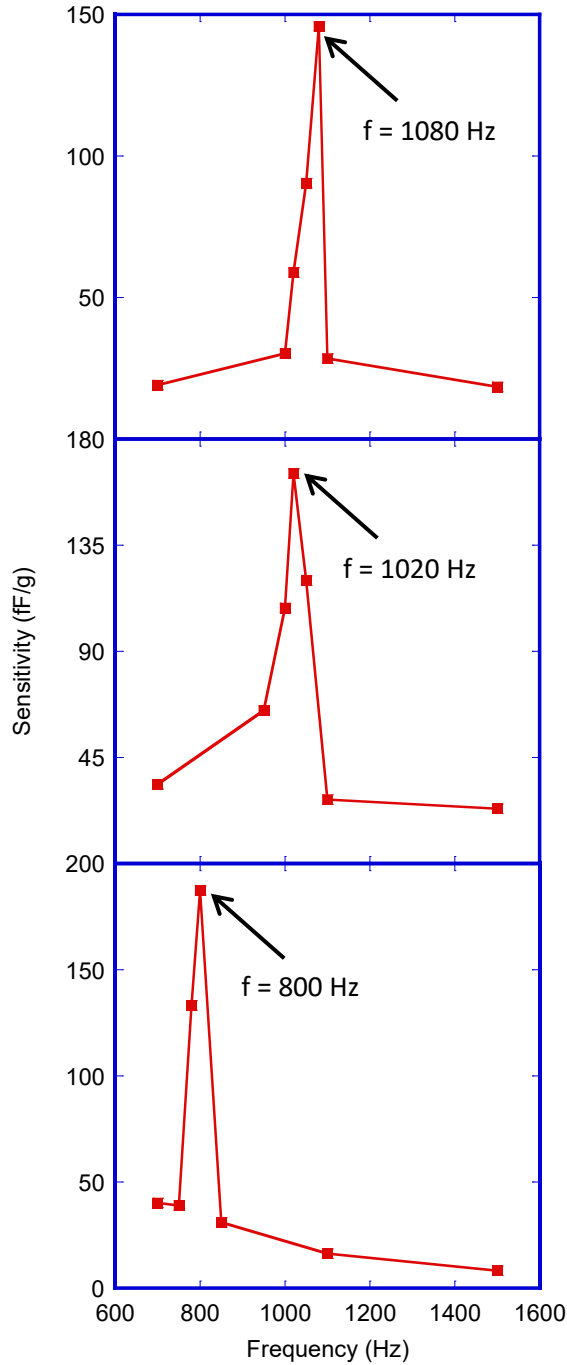


Figure 5-26 Frequency response from the accelerometers (a) A640, (b) A720 and (c) A960

illustrated in Figure 5-26 showing the highest sensitivity of A640, A720 and A960 at 1080 Hz, 1020 Hz and 800 Hz, respectively.

5.5.3 Accelerometers on a curved surface

5.5.3.1 Sensitivity

The same characterization setup was used to measure the sensitivity of the accelerometers. This time, the accelerometers were mounted on curved PVC pipes as shown in Figure 5-27 to provide different amounts of bending. The PVC pipes used in the setup had 3.8 cm, 2.5 cm and 2 cm ROC. The sensitivity was obtained to be highest at 1080 Hz, 1020 Hz and 800 Hz, respectively for A640, A720 and A960. A comparison among the accelerometers in terms of sensitivity on flat and curved surfaces is shown in Table 5-10. The percentage degradations of sensitivity when mounted on PVC pipe of 2.0 cm ROC from the performance on flat surface are 7.53%, 8.48% and 10.16% for A640, A720 and A960, respectively.

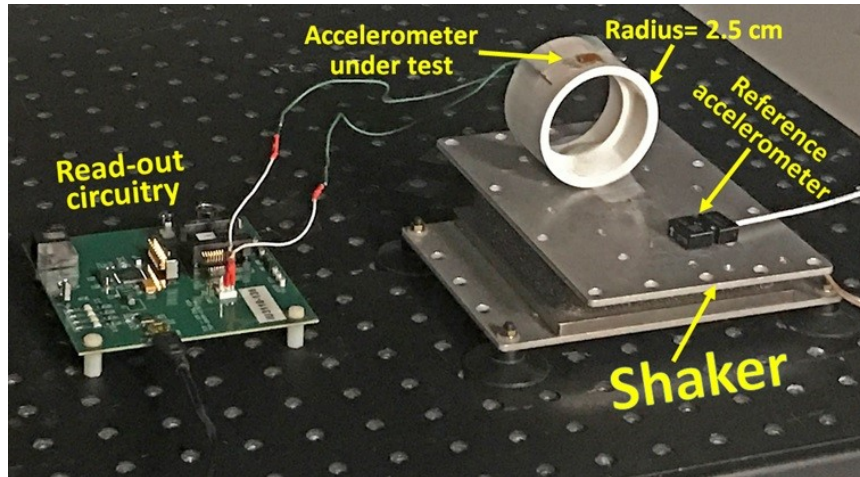


Figure 5-27 Experimental setup for characterization of the accelerometers on curved surface

Table 5-10 Sensitivity comparisons among the accelerometers when mounted on flat and curved surfaces

Devices	Flat	ROC of curved surface		
	surface	3.8 cm	2.5 cm	2 cm
A640	146	138	136	135
A720	165	159	152	150
A960	187	175	169	168

5.5.3.2 Frequency response

3-axis contour plot of sensitivity against frequency and ROC for all three accelerometers are

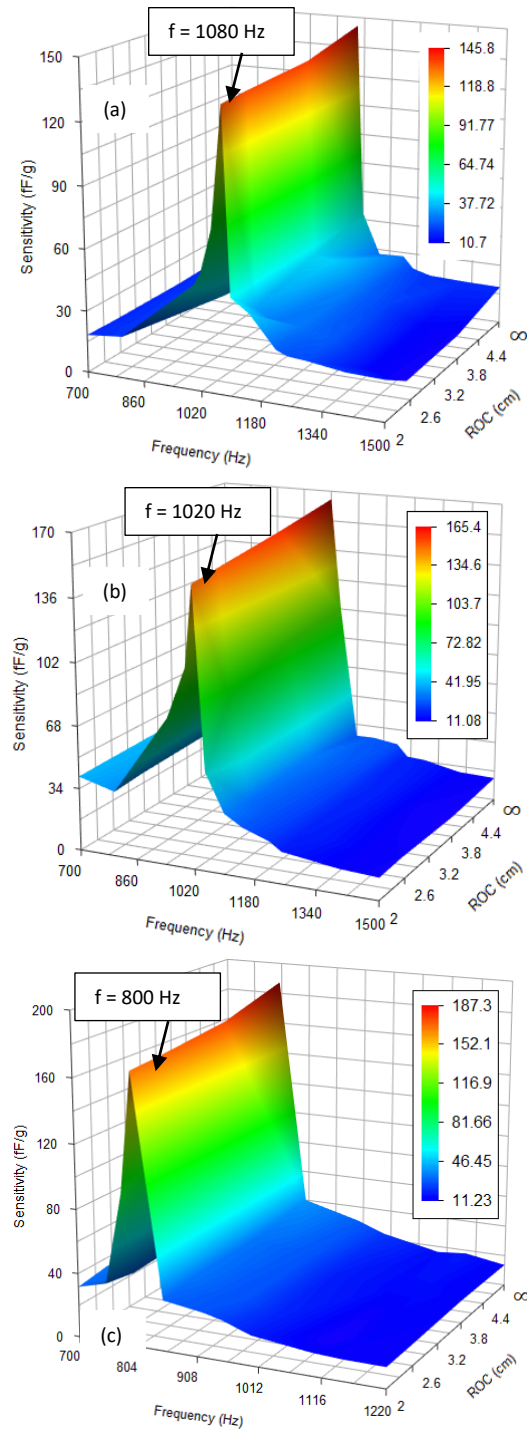


Figure 5-28 Contour plot for sensitivity of accelerometers (a) A640, (b) A720 and (c) A960. against frequency and radius of curvature of the surface the device was mounted. Flat surface is denoted by $ROC = \infty$.

illustrated in Figure 5-28. The flat surface here is denoted by infinite ROC where the sensitivity was obtained to be the highest.

5.6 Noise analysis

In order to assess the noise performance of the accelerometers, output voltage power spectral density was measured. Figure 5-29 shows the output voltage power spectrum for A640 for the excitation at 1080 Hz. Output voltage spectral density was measured (1) during normal operational conditions with the device on the shaker (Shaker ON), (2) with the shaker turned off (Shaker OFF) and (3) with the shaker operational, but the accelerometer off the shaker. (Device OFF the shaker). In the first case, the accelerometer response shows a peak at 1080 Hz and the noise level at $10 \mu\text{V}/\sqrt{\text{Hz}}$. In the second and third cases, there is no response at the vibrational frequency demonstrating lack of cross talk and the noise level is the same as the first case.

In order to calculate the components of the fluctuations contributing to the overall measured noise floor $v_n^2/\Delta f$, the noise PSD originating from the thermomechanical (Brownian) noise of the accelerometer ($v_{Br}^2/\Delta f$), from MS3110 capacitance reading circuitry ($v_{MS3110}^2/\Delta f$), and the SR560

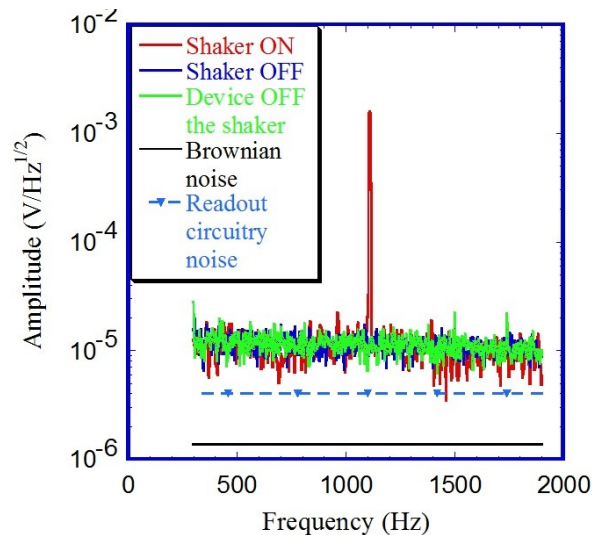


Figure 5-29 Output voltage spectral density along with the read-out circuitry noise and Brownian noise components for device A640 shaken at 1080 Hz. The measured noise floor is dominated by noise originating from the readout circuit.

amplifier ($v_{SR560}^2/\Delta f$) are referred to the accelerometer output and can be expressed as:

$$v_n^2/\Delta f = (v_{Br}^2/\Delta f) + v_{MS3110}^2/\Delta f + v_{SR560}^2/\Delta f \quad (5-4)$$

The Brownian noise is computed using [235], [236]:

$$(v_{Br}^2/\Delta f) = (4 k_B T b / m^2) S_{meas}^2 A^2 \quad (5-5)$$

where, k_B is the Boltzmann constant, T is the absolute temperature, b is the coefficient of damping, m is the mass of the proof mass, and S is the measured accelerometer sensitivity in fF/g and $A = 1 \text{ V/pF}$ as stated earlier. The effective mass of A640 is obtained as $2.61 \times 10^{-8} \text{ kg}$ from the density of electroplated Ni 8.91 g/cm^3 [237]. The coefficient of damping is calculated from [236]

$$b = \mu w_{pm}^3 L_{pm} / d^3 \quad (5-6)$$

where, μ is the viscosity of the damping medium (air) taken as $21.32 \text{ } \mu\text{Pa}\cdot\text{s}$ at 300K [238]. For A640, the Brownian noise voltage level thus calculated is $v_{Br}/\sqrt{\Delta f} = 1.36 \text{ } \mu\text{V}/\sqrt{\text{Hz}}$, about the same as what is

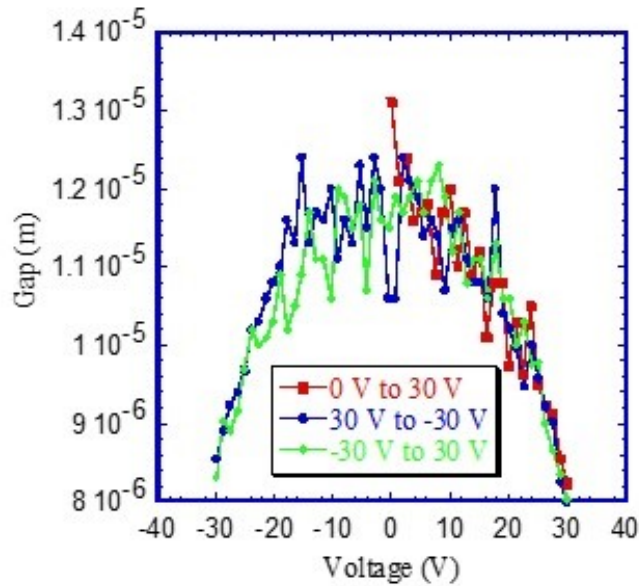


Figure 5-30 Decrease in the gap of A640 between the bottom and suspended electrodes due to the deformation of the proof-mass resulting from electrostatic force.

observed in Figure 5-29 as the noise floor. For A720 and A960, the values are $1.87 \mu\text{V}/\sqrt{\text{Hz}}$ and $2.06 \mu\text{V}/\sqrt{\text{Hz}}$, respectively.

The capacitance reading circuitry MS3110 contributes to the noise as:

$$v_{MS3110}^2/\Delta f = A^2(C_n^2/\Delta f) \quad (5-7)$$

Here, $C_n/\sqrt{\Delta f}$ is the input-referred capacitance noise of MS3110 stated as $4 \text{ aF}/\sqrt{\text{Hz}}$ [234], which yields $v_{MS3110}/\sqrt{\Delta f} = 4 \mu\text{V}/\sqrt{\text{Hz}}$ for $A = 1 \text{ V/pF}$.

The low noise amplifier SR560 will also add noise to the output. R_{out} is the output resistance of MS3110, seen as a source resistance by amplifier SR560. The noise factor (NF) for SR560 for a source resistance of $R_{out} = 10 \text{ k}\Omega$ is 0.5 dB [239], indicating that the noise added by the amplifier is negligible, leaving us with the thermal noise of R_{out} , the last term in Eq. (5-4) $v_{SR560}/\sqrt{\Delta f} = \sqrt{4k_B T R_{out}}$. This, however, contributes in the order of tens of $\text{nV}/\sqrt{\text{Hz}}$, negligible compared to the other two noise components.

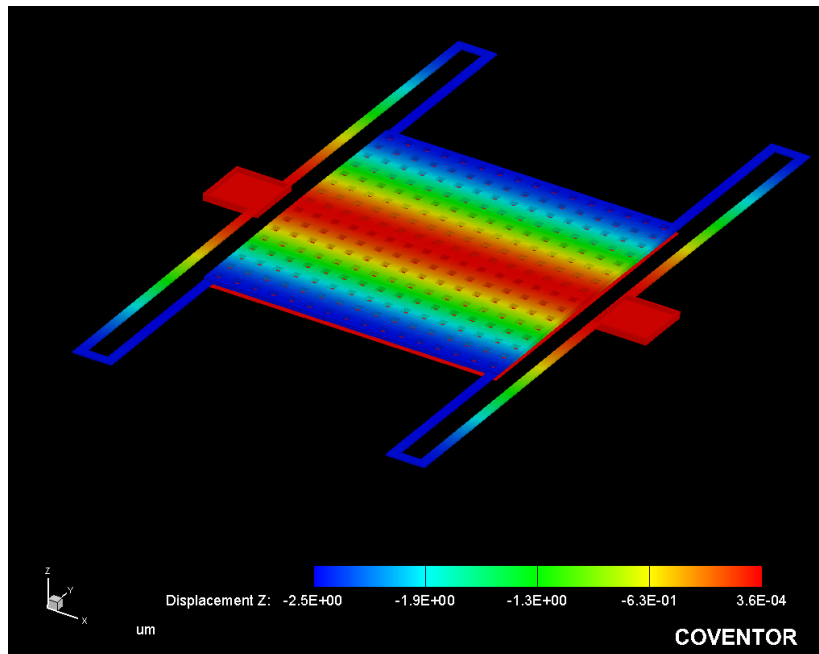


Figure 5-31 Pull-in analysis carried out in the deformed state of the proof mass and the springs

Table 5-11 Comparison between simulated and experimental pull-in voltages considering bowing of the proof mass due to residual stress

	Simulated pull-in voltage (V)	Experimental pull-in voltage (V)
A640	34.5	30.0
A720	32.0	28.8
A960	28.5	27.6

The analysis above leads to the conclusion that the noise floor observed in Figure 5-29 is dominated by the readout circuitry (MS3110 board) noise and partially by the Brownian noise of the accelerometer, a fundamental fluctuation source at room temperature.

5.7 Pull-in analysis

It has been reported in several studies that the pull-in of a MEMS structure occurs when the electrostatic force is strong enough to deform the movable electrode to one-third of the initial gap [240], [241]. Due to the residual stress and the resultant bowing of the suspended proof-mass structure, the gap beneath, forming the capacitor, is not uniform (Figure 5-21). However, it is still possible to roughly quantify the decrease in the effective gap with the applied voltage by CV measurements. Figure 5-30 shows the effective gap underneath the proof-mass of A640 as a function of applied DC voltage. Following the one-third rule described above, it can be concluded that the pull-in voltage is about ~30V, which is slightly lower than the simulated pull-in voltage of 34.5 V when the hogging due to residual stress is considered as shown in Figure 5-31. Similarly, the pull-in voltages for A720 and A960 were determined to be 32 V and 28.5 V, respectively, from the simulation. For the largest device, the pull-in voltage is smaller because it has a larger proof-mass area, which corresponds to a higher capacitance. The corresponding experimental pull-in voltages for these devices are 28.8 V and 27.6 V. Therefore, inclusion of bowing due to stress results in better matching between the simulated and experimental results as indicated in Table 5-11.

5.8 Summary

This Chapter described the design, fabrication and characterization of z-axis MEMS accelerometers on a flexible substrate. Accelerometers of three different geometry were designed using CoventorWare[®] software. The accelerometers were fabricated on a polyimide substrate to make the devices bendable. The sensitivity of the three accelerometers were measured to be highest at different frequencies. The resonant frequencies are 1080 Hz, 1020 Hz and 800 Hz for A640, A720 and A960, respectively, which also complies with the size of the accelerometers. The resonant frequencies did not change when the devices were mounted on curved surfaces having ROC down to 2.0 cm. The sensitivities of the accelerometers dropped when they were bent. The noise analysis revealed that the dominant noise source is the readout circuitry used for the measurement setup. The signal-to-noise ratio was better than 100:1. The incorporation of double UV-LIGA during electroplating of the proof mass significantly enhanced the sensitivity of the accelerometers as high as 187 fF/g compared to the state-of-the-art sensitivity of 23.3 fF/g [131]. The accelerometers fabricated in this work were encapsulated with a flexible superstrate which is described in Chapter 6.

Chapter 6

Encapsulation of flexible MEMS accelerometers

6.1 Introduction

Hermetic or vacuum packaging is required for various Microelectromechanical Systems (MEMS) for protection from contaminants including moisture [242], dust particles [243] and back-end fabrication residues [244] which can potentially degrade the performance of the devices [245]. In addition, vacuum encapsulation minimizes the possibility of stiction [246]. The packaging layer, however, might induce additional mechanical stress [247]. Often this encapsulation process introduces more complexity to fabrication and the cost associated with packaging is higher than the device fabrication cost itself [248]. Various solutions [249], [250], [251], [252] were introduced including both die-level and wafer-level packaging, with the latter being a more efficient approach.

The realization of flexibility in MEMS accelerometers is reported in Chapter 5. The proof mass of the accelerometers is fabricated utilizing SOI wafers [253], bulk-micromachined crystalline Si [254] or both [128]. As the proof mass material, metal offers more flexibility compared to polysilicon. The metal proof mass of the accelerometer has been fabricated by single-level UV-LIGA process in [131]. This process restricts the thickness of the proof mass to be the same as that of the springs and thus preventing room for flexibility in design parameters. In this work, multi-layer UV-LIGA is exploited to form central proof-mass of the accelerometer which boosts the six-fold increase in sensitivity compared to the state-of-the-art [131].

Accelerometers with moving MEMS components pose a special challenge. Die-level [255] and wafer-level packaged [256], [257], [258], [259], [138] accelerometers have been successfully demonstrated using conventional Si substrates and glass capping layers. These, however, lack flexibility and bendability. Flexible accelerometers, although previously reported [98] [125] [131] [260], have not been successfully encased into conformal, bendable vacuum packages. Applications in robotics,

prosthetics and other medical fields require functioning flexible micro-accelerometers, encapsulated in vacuum packages which allow bendability without compromising in performance.

Although Al_2O_3 has been used as a packaging material in MEMS [142], since its flexibility is low, it limits the bendability of the package. Use of polymers, on the other hand, has proven very promising [261], [262]. Wafer-level packaging using glass frit bonding has also been demonstrated, utilizing a Si cap wafer [139], [263] which itself has cavities to encapsulate the device. Two wafers are required for this encapsulation process and the associated cost is high. This work presents, for the first time, a wafer-level, low-cost, vacuum encapsulation process for flexible MEMS accelerometers using a polyimide as an adhesive as well as a robust stress buffer. HD 4110 is a negative photo definable polyimide with high glass-transition temperature ($330\text{ }^\circ\text{C}$). Polyimides were used also in [264], [142] as a base and top layer to completely embed an ultra-thin die. This technique is relatively simple but it can only be deployed with ultrathin chip package, which has already a packaged die with bond pad openings. It is particularly helpful for assembling thinned die to meet the demand for lighter products and increased flexibility. In our work, a flexible polyimide substrate is bonded to a polyimide superstrate. Cavities patterned by HD 4110 on Kapton[®] sheet are aligned with the device on a carrier wafer. This carrier wafer is removed upon completion of the packaging and can be re-used thus lowering the cost.

As explained in Chapter 5, we have designed z-axis MEMS capacitive accelerometers of three different geometry, surface micro-machined on a flexible polyimide substrate incorporating a double UV-LIGA process to make the center of the proof-mass thicker. The micro accelerometers operated in the frequency range of 600 to 1,100 Hz and were tested at an acceleration of $\pm 4\text{g}$ in addition to gravity. The largest device, with dimensions $960\text{ }\mu\text{m} \times 960\text{ }\mu\text{m}$, showed a sensitivity of 187 fF/g with a signal-to-noise ratio of at least 100 at 800 Hz. The flexible accelerometers developed in this work offered higher sensitivities than their rigid counterparts reported in the literature for similar sizes [265], [266], [267]. Without any encapsulation or packaging, the results were limited to laboratory testing but not real-life

applications. The packaging described here allows full functionality of these flexible micro-accelerometers.

The accelerometers, after completing the encapsulation, were characterized in the same way the open accelerometers were characterized [124] on flat and curved surfaces with radius of curvature (ROC) down to 2 cm. Thus, compatibility of mounting the accelerometers on robotic or prosthetic fingertips was verified, since the radii of robotic fingertips of the index finger and thumb are 1.0 cm and 3.5 cm, respectively [268].

6.2 Design requirements

To encapsulate the flexible accelerometers, a sidewall and a superstrate are required. Previously in Chapter 4, the requirements for flexible substrate and superstrate are discussed. To minimize stress at different layers of the accelerometer as well the encapsulation stack, polyimides having similar CTE to that of the substrate, were chosen. The polyimides for the sidewall and the superstrate will also possess the capability of withstanding high processing temperature. For sidewall, HD4110 negative photo-definable polyimide was preferred due to its CTE values being close to that for the underlying PI5878G polyimide substrate. The sidewalls were patterned and the cavities were formed to fit the designed accelerometers. Since there are varied sizes of accelerometers, the cavity sizes also differ. The area of the cavity openings was designed to be larger than the accelerometer as shown in Figure 6-1 to provide a margin against any misalignment during encapsulation. As an encapsulation layer, Kapton[®] sheets from Dupont were used. The thickness of Kapton[®] sheets were 50 μm . This ensures that the accelerometers remain at the half-way of the total encapsulation stack so that they experience minimum stress while bending.

6.3 Encapsulation

The step-by-step encapsulation process flow is illustrated in Figure 6-2 and described in the following sections

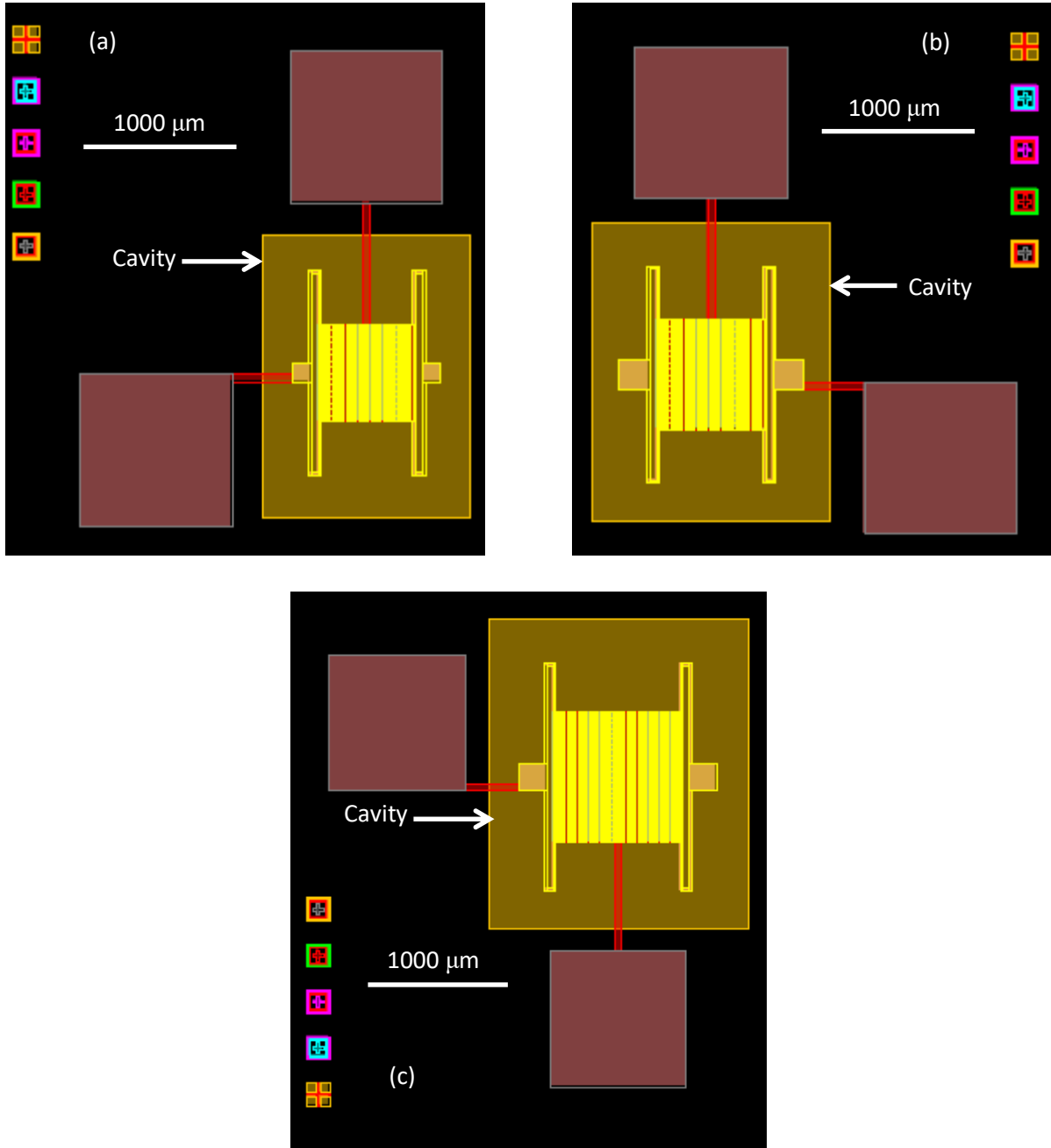


Figure 6-1 Layout of cavity size of accelerometers of geometries (a) A640, (b) A720 and (c) A960

- **Preparing Kapton® sheet**

Dupont Kapton® polymer sheets of 50 μm thickness were used for the encapsulation process, serving as a superstrate when packaging is completed. They were first baked at 350 °C for 1 hour to remove any moisture and prevent further contraction during the subsequent high temperature processes.


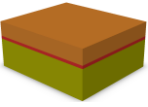
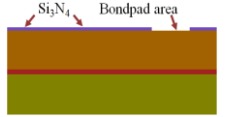
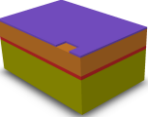

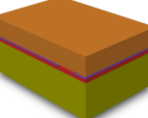
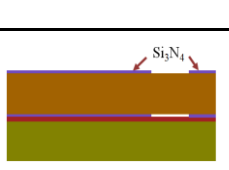
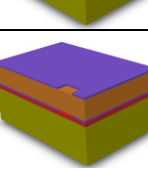
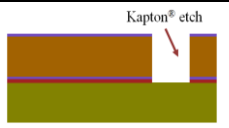
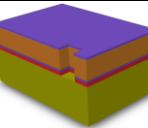
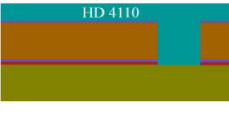
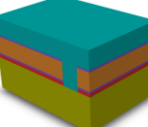

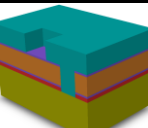
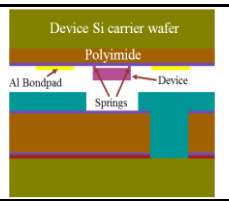
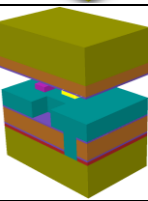
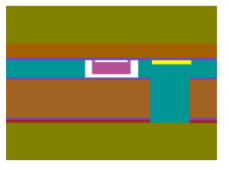
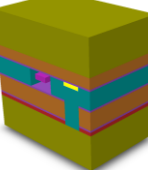

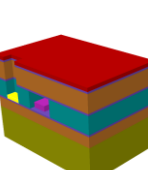
	Process steps	Schematics	Device cross section
(a)	Attaching Kapton® on 1 st Si carrier wafer		
(b)	Si ₃ N ₄ deposition & patterning with bond-pad mask		
(c)	Flip & bond patterned Si ₃ N ₄ side with 2 nd Si carrier wafer		
(d)	Si ₃ N ₄ deposition & patterning, aligning with the bottom Si ₃ N ₄ layer		
(e)	Deep reactive ion etching of Kapton®		
(f)	HD 4110 superstrate deposition		
(g)	Patterning HD 4110 superstrate with cavity mask		
(h)	Aligning device wafer with Kapton® carrier wafer (Simplified springs are shown)		
(i)	Bonding device wafer with Kapton® carrier wafer		
(j)	Etching of the superstrate to open the bond-pad locations. (Schematics and cross sections are flipped)		

Figure 6-2 Step-by-step (a)–(j) encapsulation process flow showing the schematics and device cross section. (Not to scale).

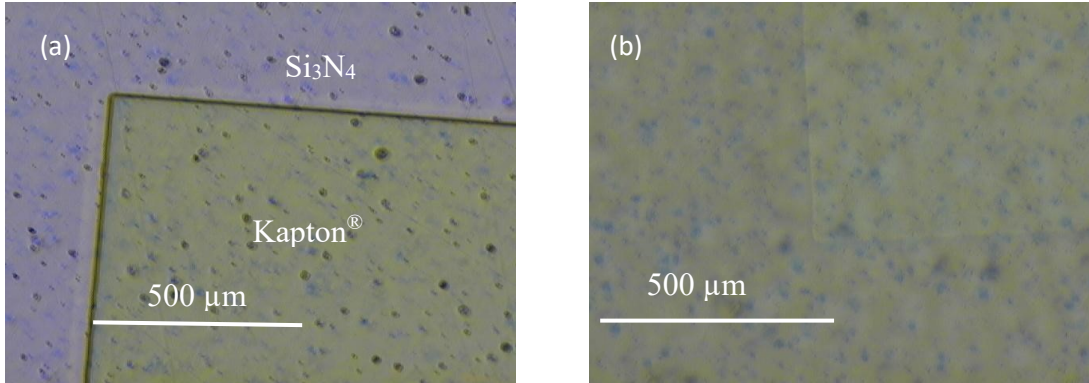


Figure 6-3 (a) Pattern on Kapton after Si_3N_4 lift-off and (b) after flipping and bonding

- **Attaching Kapton® sheet on Si wafer**

WaferBOND® HT 10.10 polyimide was spin coated on a Si carrier wafer as an intermediary layer. It also serves as a thermal release layer facilitating the removal of the carrier wafer in the final stage. It was spin coated at 2500 rpm (1000 rpm/second) for 40 seconds followed by 2 minute bake at 180 °C. The wafer along with the attached Kapton® sheet was put on a hot plate at 180 °C. Developing air bubbles were flattened using a metal tube. To ensure total attachment of the Kapton® sheet, the wafer was loaded in EVG 520IS wafer bonder, put under 1 mTorr pressure and heated up to 190 °C. A simultaneous application of 1kN of load for 5 minutes concluded the attachment process.

- **Patterning Si_3N_4**

Lift-off technique was deployed for patterning the first layer of Si_3N_4 . Lift-off resist LOR15B was spin coated at 1500 rpm for 35 seconds. Soft-baking was done at 170 °C for 5 minutes. Another positive photoresist S1813 was spin coated at 2000 rpm for 35 seconds. Soft-baking was done at 115 °C for 2 minutes. The resist was then exposed for 8 seconds, developed in CD-26 developer for 45 seconds, rinsed in DI water and dried. The wafer was baked at 125 °C for 5 minutes on a hotplate. 0.5 μm thick Si_3N_4 was sputtered on the Kapton® followed by the lift-off to create openings for bond-pads as illustrated in Figure

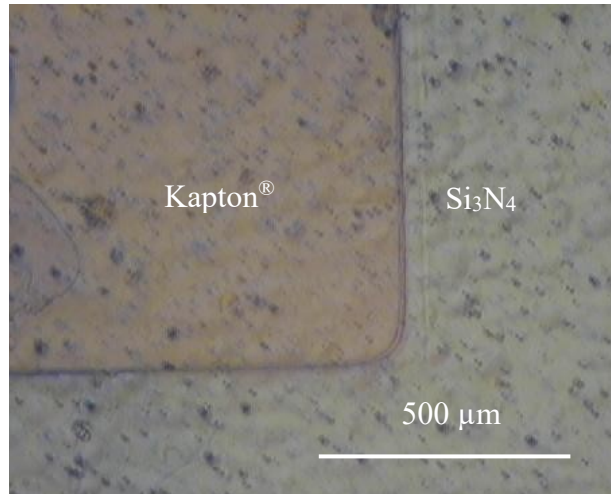


Figure 6-4 Pattern on Kapton® after 2nd Si₃N₄ lift-off

6-2(b). After sputtering, remover PG was used with ultrasonic for lift-off. Figures 6-3(a) and (b) show the top of Kapton® after Si₃N₄ lift-off and Kapton® after debonding, flipping and bonding on the 2nd Si wafer.

- **Flipping Kapton® sheet and attaching on Si wafer**

The wafer was heated at 190 °C on the hotplate and utilizing the thermal property of HT 10.10, the Kapton® was removed from the wafer, flipped and attached to a 2nd Si wafer. The wafer precoated with another layer of HT 10.10 using the same coating recipe mention before. The 1st Si wafer was cleaned by immersing in WaferBOND® remover. EVG 520IS bonder was used to apply pressure on the Kapto®n and maintain excellent bonding with the wafer. The chamber was first evacuated and was heated up to 190 °C. It was kept there for 10 minutes and then piston pressure of 1kN was applied for 5 minutes. Afterwards the chamber was cooled and the wafer was taken out.

- **2nd Si₃N₄ patterning**

A 2nd layer of 0.5 μm thick Si₃N₄ was then patterned on top of the Kapton®. This time, the top layer is aligned with the bottom layer. Since Kapton® is semi-transparent, the bottom Si₃N₄ was visible while patterning. Figure 6-4 shows the patterned Si₃N₄ on top of the Kapton® aligned with the patterned Si₃N₄ underneath the Kapton®.

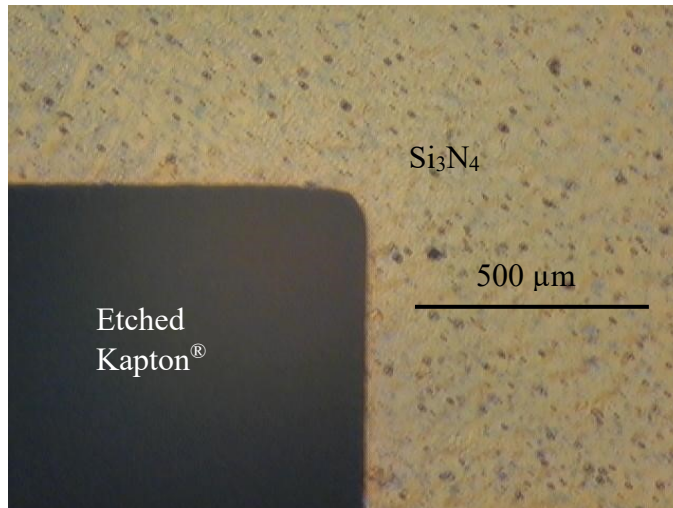


Figure 6-5 Completely etched Kapton® sheet

- **Kapton® etching**

Trion Deep Reactive Ion etcher (DRIE) was used to etch Kapton®. The chamber pressure was 15 mTorr with an O₂ flow of 70 sccm. 300 W RIE with 3000 W Inductively Coupled Plasma (ICP) power were applied during the etching. Full etching of the Kapton® sheet was complete within 50 minutes. Figure 6-5 shows completely etched Kapton® with Si₃N₄ used as a hard mask.

- **Sidewall deposition and patterning**

HD 4110 polyimide was spin coated on Kapton® at 1200 rpm for 30 seconds and baked at 90 °C for 3 minutes and then 110 °C for 3 minutes. The polyimide was then exposed for 50 seconds and then developed for 5 minutes. The patterned sidewall of HD4110 polyimide forming a cavity for an accelerometer is shown in Figure 6-6.

- **Aligning device wafer with Kapton® carrier wafer and bonding**

Alignment of the sample device wafer to the encapsulation wafer was done using EVG 620 backside aligner. The device wafer already had alignment marks on the back. After alignment, the two wafers were taken to the EVG 520IS bonder. The wafers were brought into contact by applying 1.5 kN load. Then the chamber was evacuated to under 1 mTorr pressure and the stack was heated. Bonding was

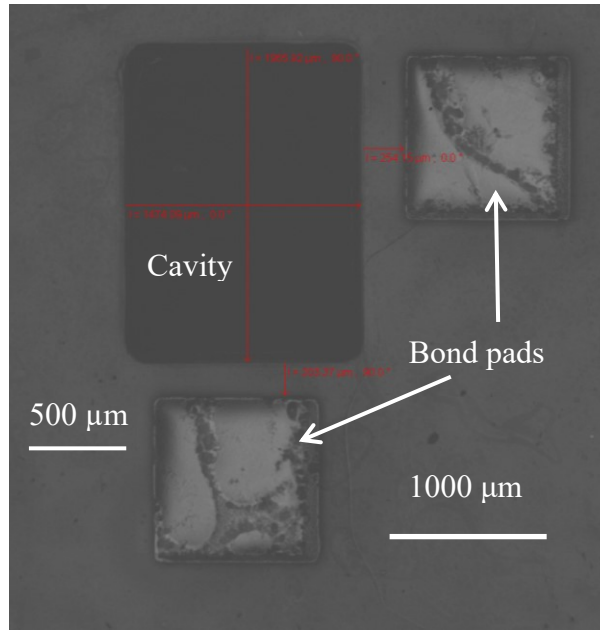


Figure 6-6 HD4110 patterning for forming cavity for accelerometer

initiated by ramping up the temperature to 200 °C with a rate of 5 °C/minute and dwell time of 30 minutes at that temperature followed by a ramp up to a peak temperature of 300 °C with a rate of 5 °C/minute for a dwell time of 10 minutes. The chamber was then cooled down at a rate of 5 °C/minute and the bonded wafers were taken out.

- **Kapton® carrier wafer debonding**

The bonded wafers were heated at 190 °C on the hotplate. Application of a shear force helped to debond the Kapton® carrier wafer using the thermal release property of HT 10.10. The released wafer was cleaned in WaferBOND® remover.

- **Etching sidewall polyimide to open the bond pads**

Trion DRIE tool was used to etch the bond pad area covered by HD4110 sidewall. The same etch chemicals and process conditions were used in this step as used in the previous step to etch Kapton®. Full etching of the HD4110 was complete within an hour. Figure 6-6 shows a completely etched bond pad location. Figure 6-7 is the SEM image of the final device with the Kapton® superstrate cut and folded up

to reveal the underlying cavity and accelerometer A720. The encapsulated accelerometers were peeled off using a sharp cutting tool and utilizing PI2611 underneath the substrate as low bond strength adhesive. The Kapton[®] superstrate as well as the polyimide substrate of the accelerometers are 50 μm thick, thus ensuring the devices are on a plane of minimal stress when bent.

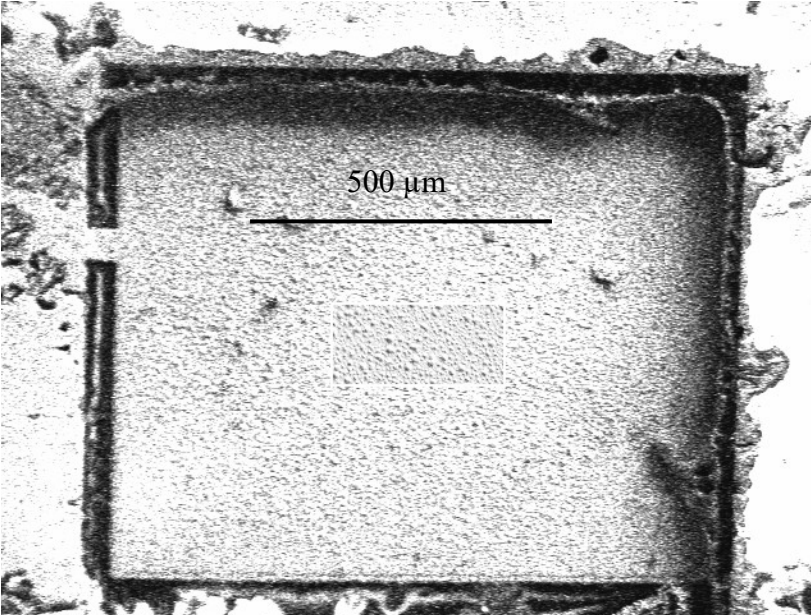


Figure 6-7 Complete etching of the sidewall polyimide

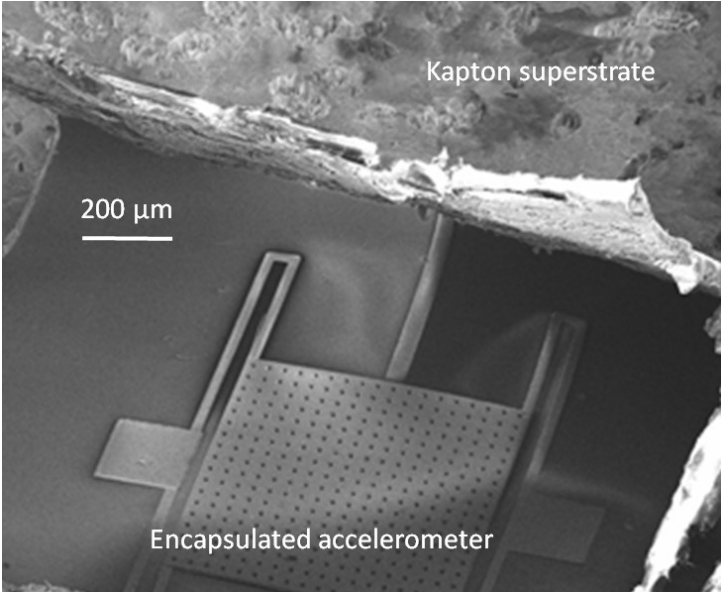


Figure 6-8. Kapton[®] lifted-off to observe the encapsulated accelerometer

6.4 Stress simulation

The stress level on different layers was simulated using CoventorWare[®]. It was observed that the maximum von Mises stress at all the device layers is below the yield strength of the layer material. Figure 6-9 shows A960 bent down to 2.5 cm ROC. The maximum layer stresses for the Au seed layer, Ni springs, HD 4110 sidewall and the Kapton[®] superstrate are 285 MPa, 312 MPa, 21 MPa and 13 MPa,

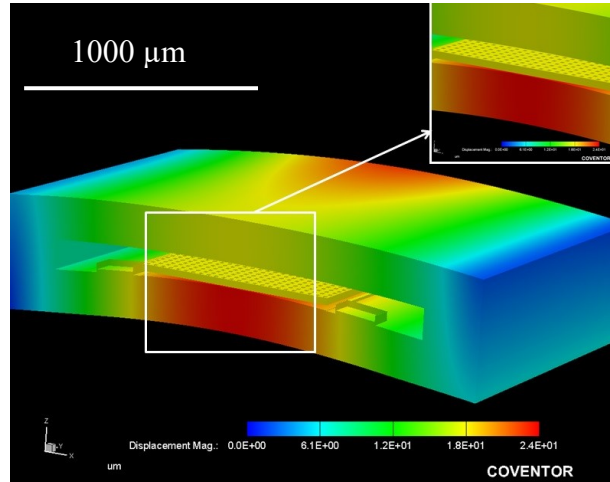


Figure 6-9 Accelerometer A960 bent down to 2.5 cm ROC. Z-axis is exaggerated 4 times.

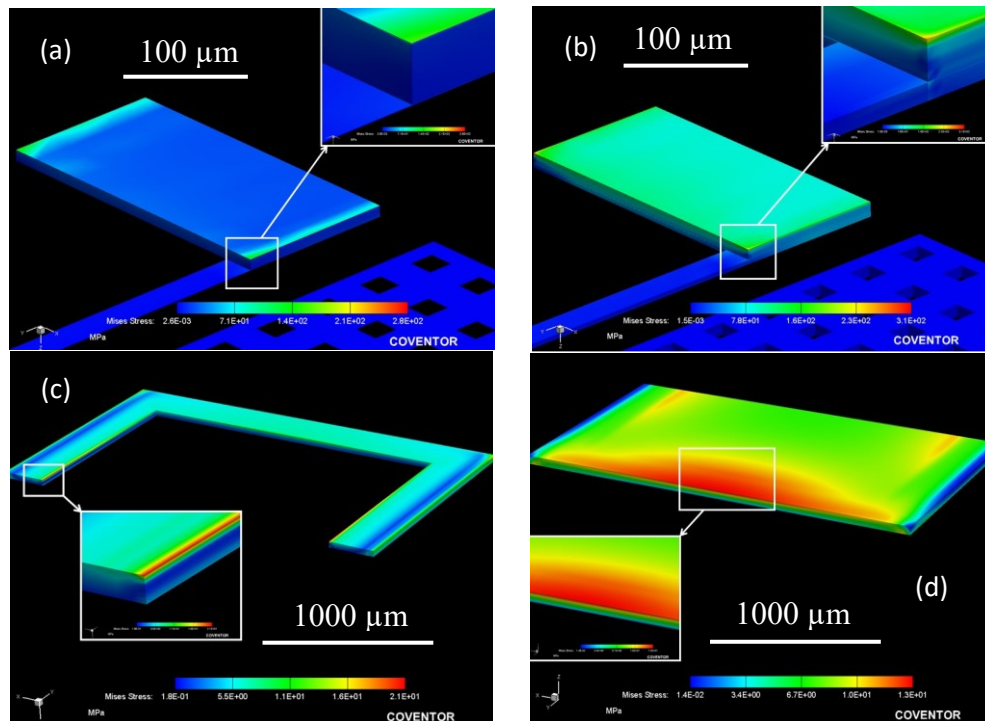


Figure 6-10 Maximum layer stress of (a) Au seed layer, (b) Ni springs, (c) HD 4110 sidewall and (d) Kapton[®] superstrate of A960. ROC = 2.5 cm.

respectively as shown in Figure 6-10, while the yield strengths of these layers are 400 MPa [231], 330-450 MPa [269], [270], 200 MPa [271] and 231 MPa [272], respectively. The simulated stress levels for the same ROC, before encapsulation of A960 were 207 MPa in the Au seed layer and 187 MPa in the Ni springs. The von Mises stress in the proof mass remained well below 1 MPa in all cases for the ROC of 2.5 cm.

6.5 Characterization

Upon completion of the fabrication of the accelerometers on a flexible substrate, experimental characterization was carried out before encapsulation. The results are published in [124]. The same accelerometers encapsulated through the procedure above were characterized again. Sensitivity, noise and flexibility of the encapsulated accelerometers were compared to those before encapsulation. The results are summarized in Table 6-1. The setup in [125] was utilized for the characterization of the encapsulated accelerometers. The accelerometers were initially wire bonded inside a flat package and placed on a Controlled Vibration ED-10 shaker. The shaker was connected with Crown DSi 1000 power amplifier controlled by a LFG 1300S function generator. Irvine Sensors MS 3110 interface circuit was coupled with the device to convert the capacitance change into voltage and later the signal was filtered by Stanford Research Systems SR560 low noise amplifier. The final output was observed in an oscilloscope. A reference accelerometer 2260-100 from Silicon Designs was also attached on the shaker for calibration purposes.

Table 6-1 Sensitivity comparison among the accelerometers on surfaces of different ROCs before and after encapsulation

Devices	Sensitivity (fF/g)							
	Flat surface		ROC of curved surface					
	Before	After	3.8 cm		2.5 cm		2 cm	
Before			After	Before	After	Before	After	
A640	146	157	138	143	136	140	135	139
A720	165	171	159	167	152	164	150	163
A960	187	195	175	181	169	179	168	174

6.5.1 Sensitivity

Figure 6-11 shows the change in capacitance of the encapsulated accelerometers when characterized on a flat surface along with the results on a curved PVC surface. The frequencies of vibration for A640, A720 and A960 were 1050 Hz, 1010 Hz and 800 Hz respectively, corresponding to their resonance frequencies of vibration after encapsulation [124].

6.5.2 Flexibility performance

To perform the flexibility test, the same encapsulated accelerometers were removed from the flat package and directly mounted on a PVC pipe with ROC of 3.8, 2.5 and 2.0 cm. Responses from A640, A720 and A960 mounted on curved surfaces are depicted in Figures 6-11 (a), (b) and (c), respectively. In all the four cases of ROC ranging from 2.0 cm to infinity, the response is linear with minimal hysteresis.

A 3-axis contour plot for sensitivity of encapsulated accelerometers A640, A720 and A960 are shown in Figures 6-12 (a), (b) and (c) respectively against frequency and ROC. The contour plots for the same accelerometers before encapsulation are in Figures 6-12 (d), (e) and (f). The percentage degradation of sensitivity for encapsulated accelerometers A640, A720 and A960 when mounted on 2 cm ROC surface compared to the flat surface results are 11%, 5%, and 11%, respectively which is attributed to the non-uniformity between the electrodes.

6.5.3 Noise performance

Noise power spectrum of the output signal was observed in Agilent 35670A signal analyzer. Figure 6-13 shows the power spectral density of each of the accelerometers with the time domain output in inset. The noise floor was detected to be as low as $10 \mu\text{V}/\sqrt{\text{Hz}}$ and the signal power is approximately 2 orders of magnitude higher than the noise floor in all cases. Power spectrum when the shaker is off and when the device is off the shaker but the shaker is on overlap with the noise floor when the shaker is on. The calculated Brownian noise level for A640, A720 and A960 are $1.71 \mu\text{V}/\sqrt{\text{Hz}}$, $1.94 \mu\text{V}/\sqrt{\text{Hz}}$ and $2.14 \mu\text{V}/\sqrt{\text{Hz}}$ respectively. The noise contribution from the MS3110 readout circuit and the low noise amplifier

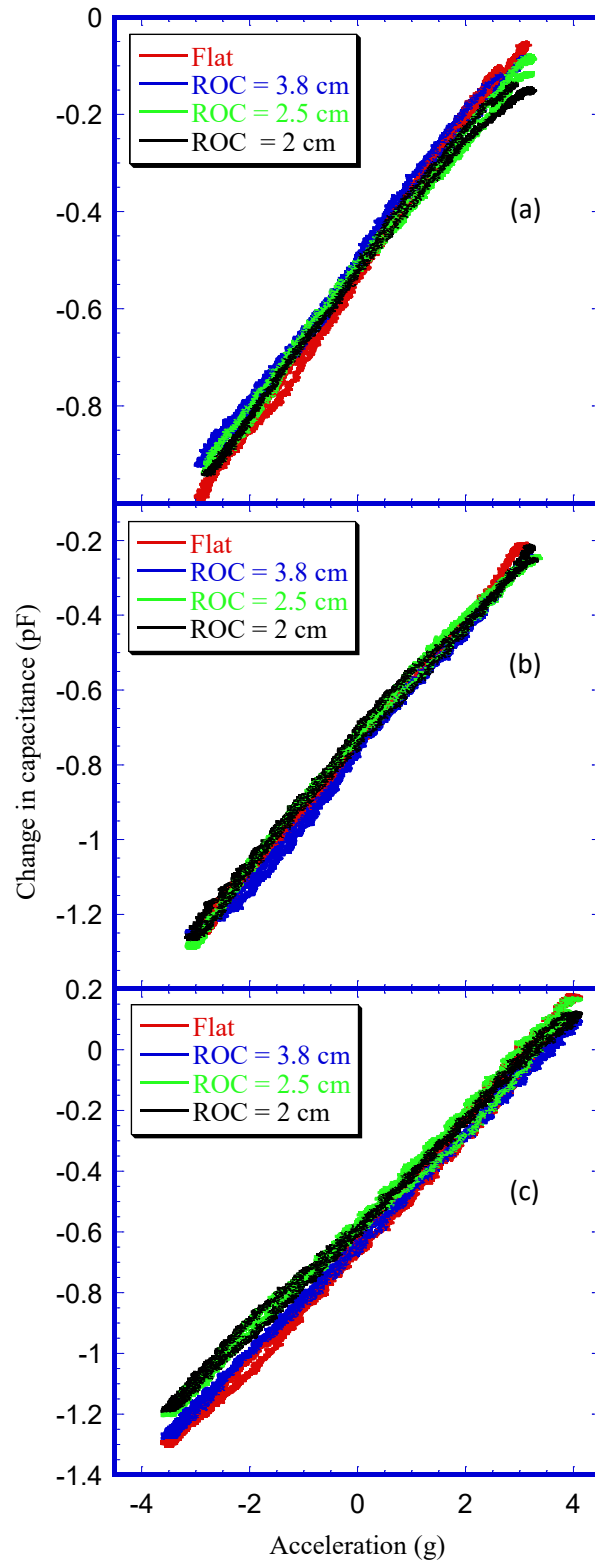


Figure 6-11 Capacitance change of the accelerometers at their resonant frequencies: (a) A640 at 1050 Hz, (b) A720 at 1010 Hz and (c) A960 at 800 Hz when subjected to acceleration. Accelerometers were mounted both on flat and curved surfaces with ROC = 3.8 cm, 2.5 cm and 2 cm.

SR560 were also calculated to be $4.0 \mu\text{V}/\sqrt{\text{Hz}}$ and $12.87 \text{ nV}/\sqrt{\text{Hz}}$ [273]. Comparison of the contributions among the noise sources leads to the readout circuitry as the most dominating source of noise while Brownian motion of the accelerometers have less significant portion in the total noise. Based on these figures, Brownian noise equivalent acceleration measurement capability is computed to be $10\text{-}15 \mu\text{g}/\sqrt{\text{Hz}}$. The noise performance did not exhibit any change with ROC.

6.6 Effect of encapsulation on accelerometers

Table 6-1 shows the sensitivity for the three accelerometers in all four scenarios before and after the encapsulation. The highest sensitivity of 195 fF/g was obtained for the encapsulated A960. This is to be expected as the largest accelerometer has the highest proof mass. As can be seen in Figure 6-12, there is a slight shift in the resonant frequencies, but well within variation from device to device. The sensitivity has increased 3-9 % with encapsulation, depending on the device type.

The flexibility has improved with encapsulation as per original design. When the accelerometers are subjected to bending before encapsulation, maximum stress develops on the top surface holding the devices. In the case of encapsulated accelerometers, however, the superstrate is under tension, while the substrate is under compression. At the neutral plane of the stack lies a low stress plane which experiences minimal strain. If the stiffness of the device layer in the middle is negligible, then the accelerometers can be made to lie on a plane of no strain as long as the following expression $Y_s d_s^2 = Y_e d_e^2$ is valid [41]. Here, the subscript e refers to the encapsulation while the subscript s refers to the substrate. Y is the Young's or tensile modulus and d is the thickness of the layer. In our case, since both the substrate and the encapsulating superstrate are polyimides, an optimal design would require the substrate and superstrate thicknesses to be the same, ($\sim 50 \mu\text{m}$), which was part of the design. The noise performance has not changed with encapsulation

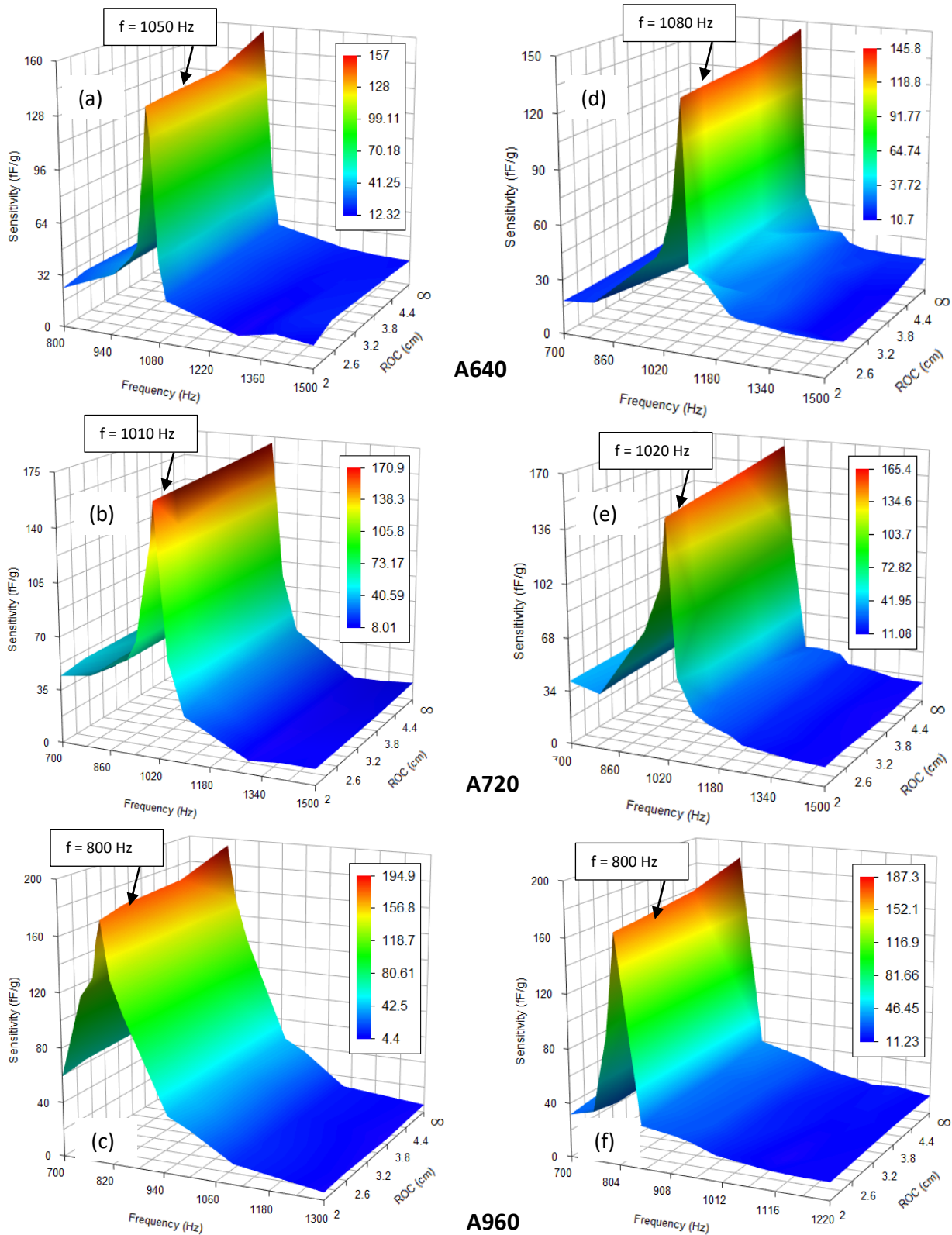


Figure 6-12 Contour plot for sensitivity of accelerometers (a) A640, (b) A720 and (c) A960 after encapsulation (d) A640, (e) A720 and (f) A960 before encapsulation against frequency and radius of curvature of the surface the device was mounted. Flat surface is denoted by $ROC = \infty$. The vibration frequency at which the maximum sensitivity is observed is marked for each case.

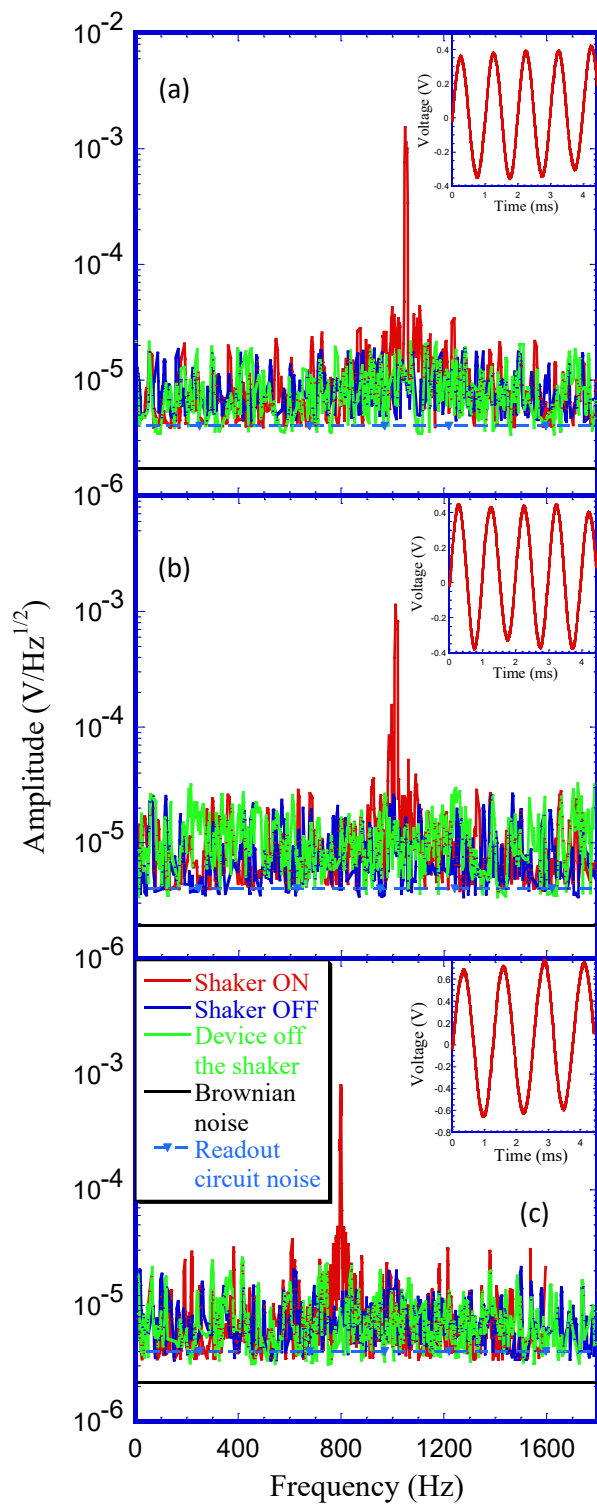


Figure 6-13 Noise spectrum of the accelerometers (a) A640, (b) A720 and (c) A960 plotted with the environmental noise when the shaker is turned off and when the shaker is on but the device is off the shaker. The time domain responses of the accelerometers are shown in inset. Also shown are the Brownian noise and the read-out circuitry noise. The peaks are observed at 1050 Hz, 1010 Hz and 800 Hz for A640, A720 and A960 respectively, corresponding to shaker vibration frequency for each case.

6.7 Summary

MEMS capacitive accelerometers of three varied sizes were fabricated on a flexible substrate and vacuum-packaged with a polyimide superstrate. The measured sensitivities of the accelerometers vary between 157 fF/g and 195 fF/g on a flat surface and between 139 fF/g and 174 fF/g when curved down to 2 cm radius of curvature. Brownian noise equivalent acceleration measurement capability was $10 \mu\text{g}/\sqrt{\text{Hz}}$. The resonant frequencies of the accelerometers range from 800 to 1050 Hz. The encapsulation process was found to improve the accelerometer response. Exhibiting excellent performance down to 2 cm radius of curvature, these self-packaged accelerometers may be conformably mounted on a curved surface, including prosthetic and robotic extremities with small ROCs, to aid in their motion.

Chapter 7

Ultra-thin AlN cantilevers on flexible substrate

7.1 Introduction

Excellent piezoelectric properties and very good compatibility with CMOS process have made AlN a very promising material for piezoelectric sensor. Less investigation of piezoelectric property was done on AlN than on PZT and ZnO films. Their temperature/humidity stability and higher signal-to-noise ratio are more attractive than other piezoelectric materials [274]. In general, piezoelectric materials with a higher Curie temperature possess a lower piezoelectric coefficient [275]. Lead zirconium titanate (PZT) has Curie temperature and piezoelectric coefficient of 250 °C and 410 pC/N [275], respectively. The maximum process temperature of AlN is 1150 °C and its piezoelectric coefficient is 5.5 pC/N [275]. ZnO has a piezoelectric coefficient of 12.4 pC/N [275]. A good balance between the maximum process temperature and large piezoelectricity in a material is difficult to achieve. Until now, there is no piezoelectric material that simultaneously possess these two desired characteristics [275].

7.2 Review of the state-of-the-art for AlN cantilevers

Micro cantilever structures are the most simplified among other sensor structures and offer an excellent platform for sensing at micro and nano scale. This simplicity in design and fabrication make them to be commonly employed as biomedical [276], mechanical [277], chemical [278] and electrical [279] transducers. AlN cantilevers as a pressure sensor were reported in several works. Surface micromachined ultra-thin AlN pressure sensor with a dimension of 60 μm \times 12 μm \times 0.3 μm was fabricated on a Si substrate [6] with Ti electrodes. The AlN layer, sandwiched between the Ti electrodes, was deposited by sputtering at 300 °C. The output voltage from the cantilevers varied between 3.69×10^{-5} V to 4.48×10^{-4} V. Effect of annealing temperature on the AlN thin film was studied by Gillinger *et al.* In their work [280], 100 nm and 500 nm AlN thin films were reported to demonstrate similar stress when

annealed up to 600 °C, separately in an N₂ and O₂ environment. The c-axis orientation of the AlN film was stable up to 1000 °C, except in one case when annealed in O₂ atmosphere. At that high temperature, AlN film gets oxidized and forms an amorphous microstructure. Another surface micromachining process to fabricate AlN micro-cantilever, was reported in [281] where SiO₂ was used as a sacrificial layer and AlN was deposited at temperature < 400 °C. Isotropic etching technique was used to release the sacrificial layer followed by freeze-drying process. Cr was utilized as the electrodes and the thickness of the cantilever was 2 μm. Molybdenum (Mo) can also serve as an electrode for an AlN cantilever as demonstrated in [282]. A 900 nm thick AlN layer, sandwiched between two Mo electrodes having thickness of 120 nm each, was deposited using DC sputtering technique at an elevated temperature of 120 °C. Cantilevers may suffer from initial bending due to tensile stress developed at the surface. The bending can be modified by changing the residual stress from tensile to compressive by reducing the DC sputtering power [283] [284]. This offers the opportunity to fabricate cantilevers without bending which is also adopted in [6]. The 500 μm long AlN cantilever was bent upward instead of downward by lowering the sputtering power. Kapton® sheet was utilized by Petroni *et al.* [285] as a flexible substrate for AlN cantilever structures deposited at 250-300 °C. The cantilevers were patterned and suspended using O₂ plasma etching of the polyimide sacrificial layer. Larger AlN cantilevers with dimensions of 1500 μm × 1000 μm × 2 μm, fabricated by Tomimatsu *et al.* [286], demonstrated a sensitivity of 8.2 mV/Pa.

Bulk micromachining technology was deployed for fabrication of thinner AlN cantilevers down to 50 nm [287]. Cantilevers with Pt electrodes were used for high resolution gas detection. Si substrate was isotropically etched by XeF₂ and the cantilevers were released.

In this work, ultra-thin 60 μm × 12 μm AlN cantilevers with a thickness of 250 nm were formed on a flexible polyimide substrate using sputter deposition at room temperature. Ti layer, used as the electrode, was deposited using e-beam evaporation. Lift-off technique was utilized to pattern the cantilevers and O₂ plasma ashing to remove the sacrificial polyimide layer. After ashing, the cantilevers

were annealed at 380 °C to increase the piezoelectric response of AlN. The measured sensitivity of the cantilevers varied between 1.90×10^{-4} V/kPa and 2.04×10^{-4} V/kPa. The cantilevers also demonstrated excellent responses to sinusoidal changes of incoming pressure. The frequency of the pressure was varied between 3 Hz and 15 Hz.

7.3 Design

The pressure detection range was aimed in between 100 kPa and 1 MPa which covers various tactile pressures from everyday human interactions. Tactile pressure from the contact of a glove ranges from 100 kPa to 325 kPa [288]. Pressure on the finger is between 100 kPa - 800 kPa [289] while grasping a cylinder and 50 kPa - 900 kPa while working with screwdriver [302]. The pressure from a hand fist punch of human is 500 kPa [290]. Simulations were completed in CoventorWare® software to measure the pressure limit as well as the maximum stress at each layer.

Figure 7-1 shows the process flow for AlN cantilever fabrication. A 50 µm thick flexible substrate and 0.5 µm thick Si₃N₄ insulation layer were first deposited on a Si wafer following the same fabrication steps of a MEMS capacitive flexible accelerometer. Ti was used as the bottom electrode in the process flow. Ti, Al or Pt can also be utilized as the bottom electrode. However, Ti was chosen for the following reasons:

Step Name	Layer Name	Material Name	Thickness	Mask Name	Photoresist
Substrate	Substrate	POLYIMIDE	50	GND	
Stack Material	Nitride	SI3N4	0.5		
Stack Material	Titanium_layer	TITANIUM	0.2		
Stack Material	Sacrifice	POLYIMIDE	2		
Straight Cut				anchor	-
Conformal Shell	bottom_electrode	TITANIUM	0.2		
Conformal Shell	piezoelectric_layer	AlN	0.25		
Conformal Shell	top_electrode	TITANIUM	0.2		
Straight Cut				bottom_electrode	+
Straight Cut				piezoelectric_layer	+
Straight Cut				top_electrode	+
Delete		POLYIMIDE			
Stack Material	square_patch	ALUMINUM	0.005		
Straight Cut				patch	+

Figure 7-1 Process flow for AlN cantilever fabrication

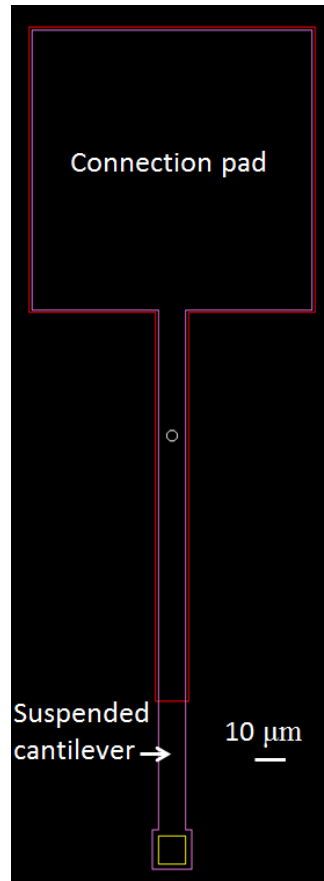


Figure 7-2 Cantilever layout in CoventorWare®

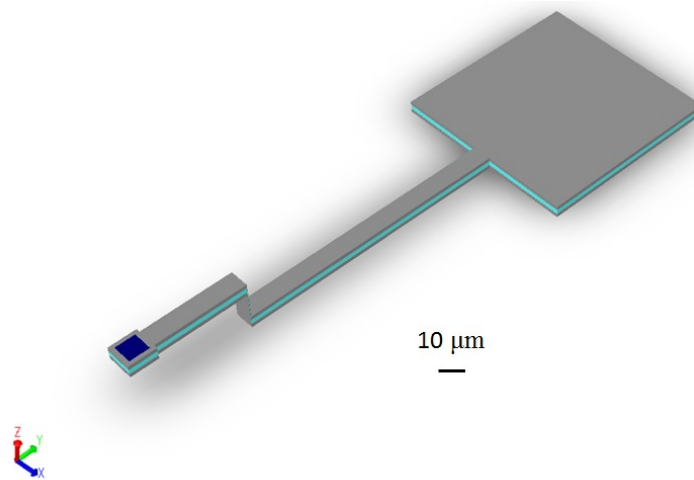


Figure 7-3 Cantilever solid model in CoventorWare®

- Pt is more expensive than Al or Ti
- Pt and Ti have comparable lattice mismatch of 5% with AlN [291]
- Al has lattice mismatch of 23% with AlN [7]
- Ti can reduce the stress near film surface because of its similar CTE to that of AlN [292]

The thickness of Ti was set at 0.2 μm . X-ray diffraction (XRD) analysis [293] showed that thinner electrode thickness ($< 0.2 \mu\text{m}$) results in wider full width at half maximum (FWHM) of XRD peak located at the diffraction angle of the film material. Since the crystallinity of AlN strongly depends on the crystal orientation of the underlying bottom electrode [294], the thickness of 0.2 μm for bottom electrode was chosen to make it highly c-axis oriented with a smaller FWHM value. Afterwards, a 2 μm thick sacrificial polyimide was patterned on Ti to form the islands on top of which the cantilevers will be suspended. The step was followed by the deposition of another 0.2 μm Ti and 0.25 μm AlN. AlN was sputtered at room temperature. After sputtering the AlN layer, the top Ti electrode was deposited which has a thickness of 0.2 μm too. Once the sacrificial layer is removed, the tri-layer stack of Ti-AlN-Ti becomes suspended. A patch of 10 $\mu\text{m} \times 10 \mu\text{m}$ was also defined on top the cantilever tip in the very last step of the process flow. The layout of the cantilever and the solid model built from the process flow are graphically shown in Figure 7-2 and Figure 7-3, respectively.

7.4 Simulation

Once the process flow is prepared, a solid model was built in CoventorWare[®]. A series of loads varying between 100 kPa to 1MPa were applied on the patch. The simulated displacement data is plotted against applied pressure in Figure 7-4. The slope of the curve indicates 2.32 μm of cantilever movement per 100 kPa applied pressure. For the applied pressure of 850 kPa, a displacement of 2.0 μm was observed. Since the sacrificial layer thickness is 2.0 μm , this limits the maximum applicable pressure on

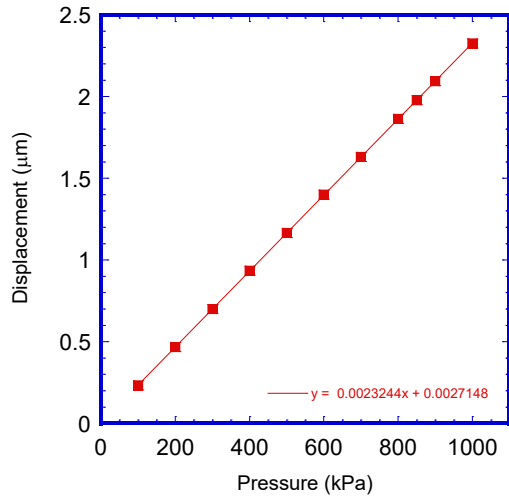


Figure 7-4 Simulated displacement vs pressure plot of the 60 μm × 12 μm × 0.25 μm cantilever

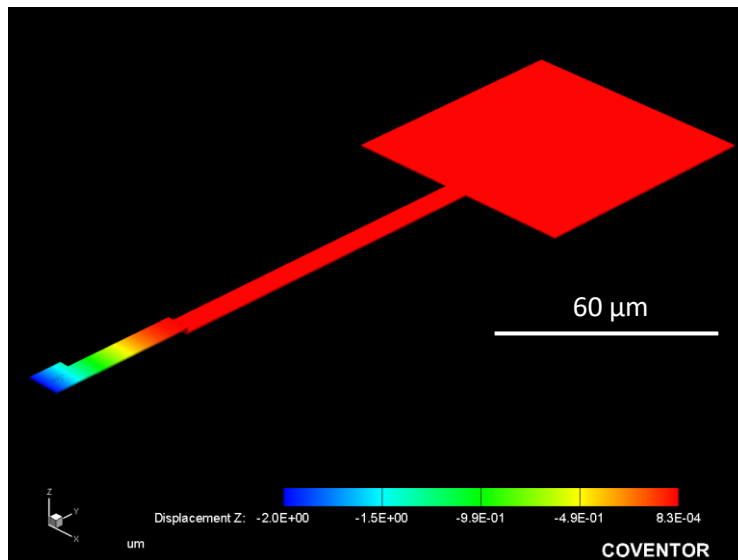


Figure 7-5 Simulated displacement upon application of 850 kPa pressure on cantilever tip. The tip displaced 2 μm downward which is equal to the sacrificial layer thickness.

the cantilever to 850 kPa. The displacement of the cantilever is graphically illustrated in Figure 7-5 for the applied pressure of 850 kPa. A further stress simulation was performed to ensure the stability of the structure under such pressure. Figure 7-6 shows the stress in the tri-layer of Ti-AlN-Ti stack. The stress at the bottom and top Ti layers is 120 MPa and 110 MPa, respectively whereas the stress at the AlN layer is 63 MPa. The yield strength of Ti and AlN are 800 MPa [295] and 300 MPa [296], respectively.

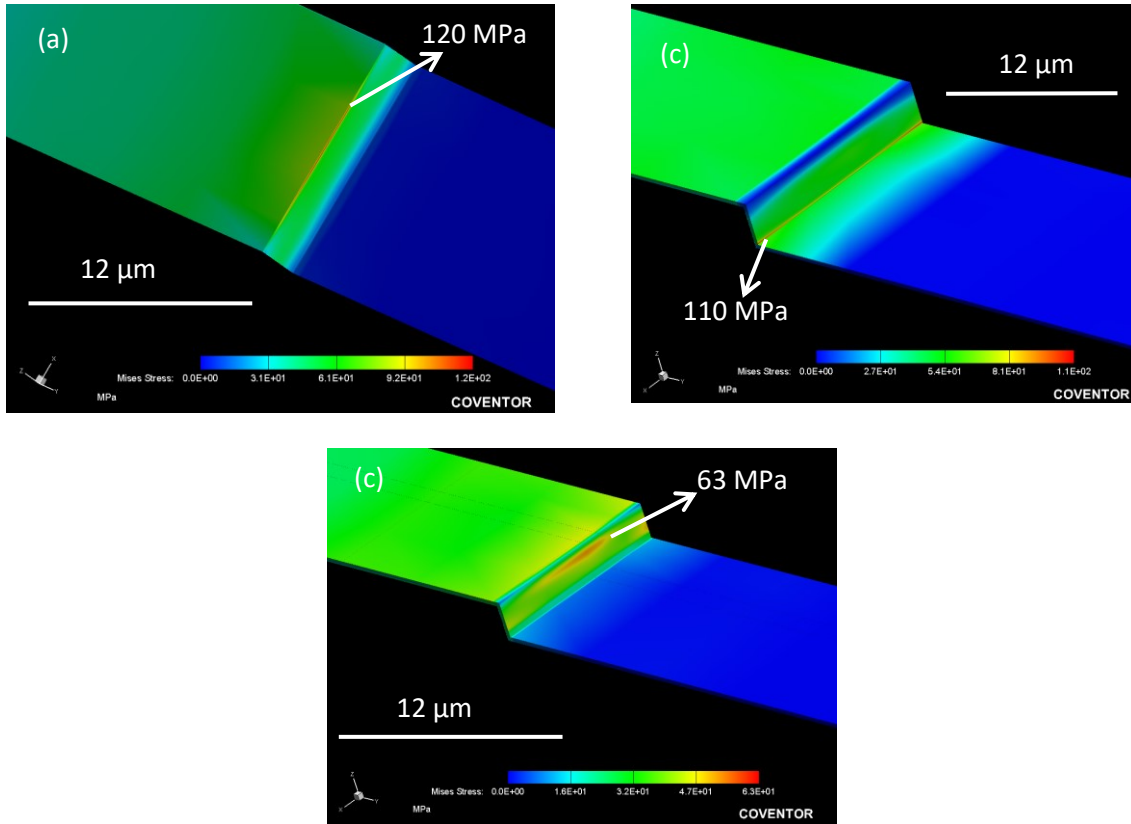


Figure 7-6 Simulated stress at (a) bottom Ti (b) top Ti and (c) AlN layer

7.5 Fabrication

The AlN cantilevers were fabricated on a flexible polyimide substrate. The same polyimide was utilized to form the substrate of the first project on MEMS accelerometer. Once the flexible substrate is formed, the following fabrication steps were followed.

- **Contact layer deposition**

200 nm thick Ti was sputtered using the home-built sputtering tool at room temperature. Sputtering pressure was set at 3.5 mTorr and power at 200 W to deposit Ti for 6.5 minutes.

- **Sacrificial layer deposition and patterning**

The polyimide used for sacrificial layer deposition is HD4104 which is the same polyimide used for deposition of the sacrificial layer in the project of flexible MEMS accelerometer. The same spin coating, developing and curing steps were followed to form this patterned polyimide.

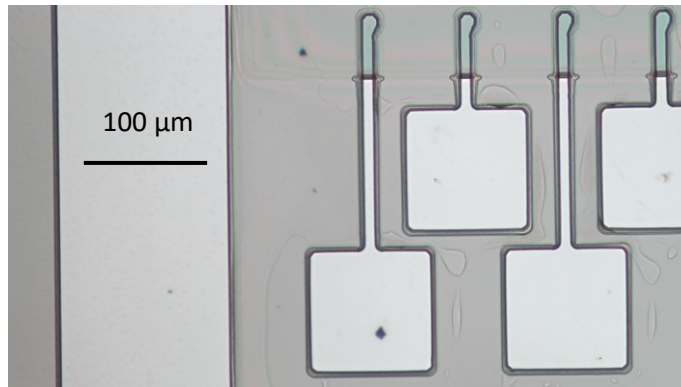


Figure 7-7 Connection pads are defined after developing the NR9-1500PY photoresist

- **Connection pad and cantilever locations patterning**

NR9-1500PY was spin coated in a two-step process. The resist was spin-coated at 500 rpm (100 rpm/second) for 5 seconds followed by 3000 rpm (800 rpm/second) for 40 seconds. It was then baked at 150 °C for 60 seconds and exposed in aligner for 14 seconds. Post bake was completed at 100 °C for 60 seconds and finally developed in RD6 developer for 10 seconds to define the connection pads as shown in Figure 7-7. Figure 7-8 shows the cantilever location ready for the tri-layer deposition.

- **Bottom electrode deposition**

The bottom electrode was deposited utilizing the similar process of the first layer of Ti deposition. The thickness of bottom Ti is also 200 nm. Ti got deposited everywhere on the wafer as shown in Figure 7-9.

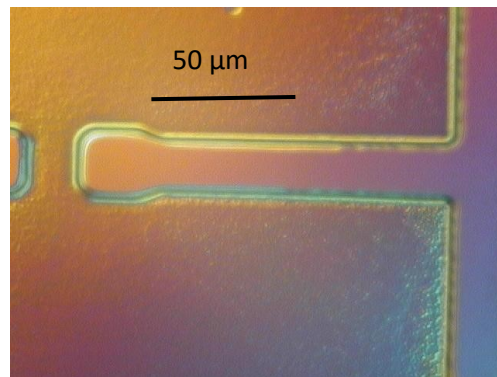


Figure 7-8 Cantilever locations are defined and ready for the tri-layer deposition

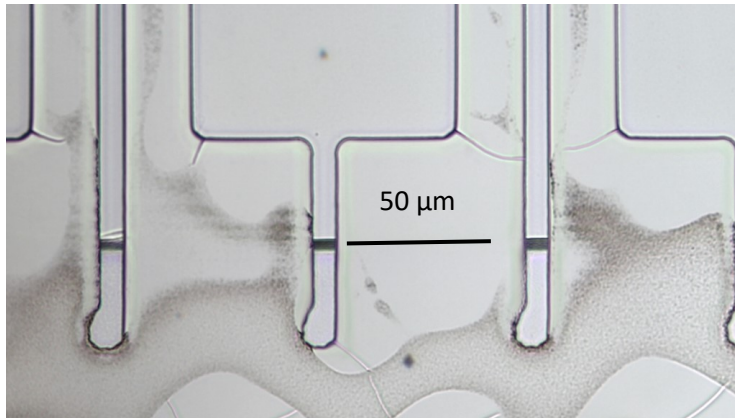


Figure 7-9 Bottom Ti layer deposition

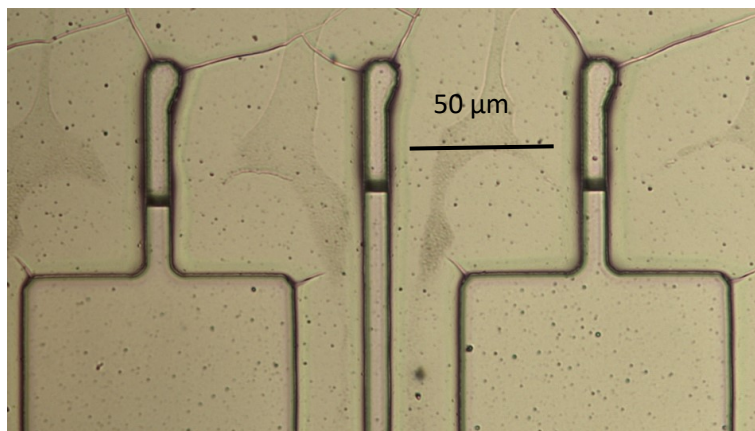


Figure 7-10 AlN and top Ti layer deposition

- **Piezoelectric layer deposition**

AJA sputtering tool was utilized to sputter 250 nm thick AlN at room temperature for 150 minutes. The sputtering pressure was set at 3.5 mTorr and power at 200 W. The chamber environment was composed of Ar and N₂.

- **Top electrode deposition**

The top electrode was also processed in the analogous way the bottom one was deposited. The electrode thickness was 200 nm. Figure 7-10 shows the patterns after the Ti-AlN-Ti tri layer deposition.

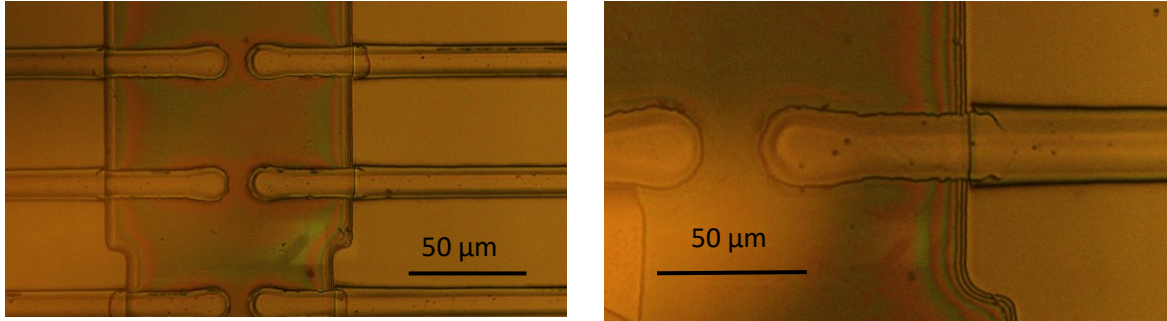


Figure 7-11 Tri layer lift-off

- **Lift-off, ashing and annealing**

The wafer was immersed in 1165 resist stripper and put in ultrasonic bath for lift-off. After the tri layer lift-off as shown in Figure 7-11, the wafer was put in Diener asher to remove the sacrificial layer and suspend the cantilever. The ashing process required 12 hours (Figure 7-12). The cantilevers were bent up after ashing due to the stress built up on the surfaces. Finally, the cantilevers were annealed by placing the wafer at 380° C for 2.5 hours in N₂ environment.

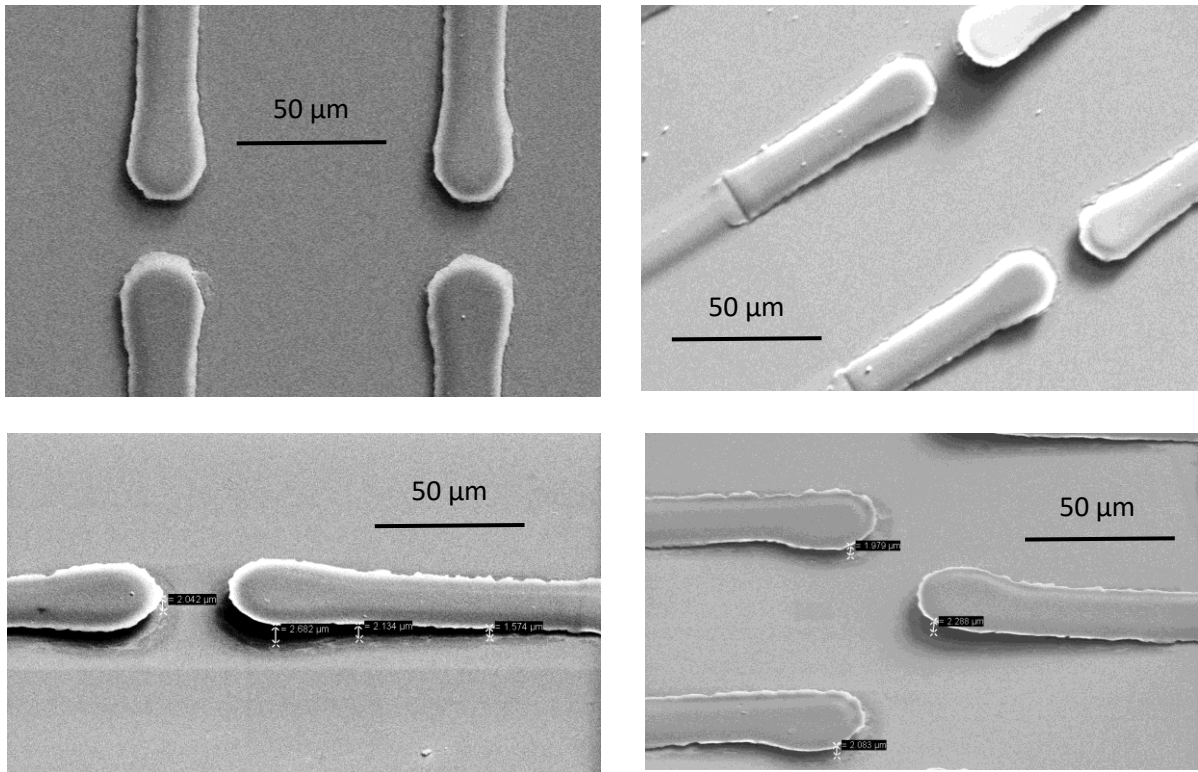


Figure 7-12 SEM images of completely ashed cantilevers

7.6 EDX and XRD

Once the fabrication of the cantilevers was complete, EDX was done on several cantilevers to detect the composition of the components. EDX result as shown in Figure 7-13 indicates the presence of AlN and Ti in the cantilever. The atomic ratio between Al:N:Si:Ti is 39.84: 47.42:8.56:4.18.

Later XRD was done on the cantilevers to detect the crystal orientation of the piezoelectric layer. Figure 7-14 shows the peak of AlN positioned at 36.54° and Ti peak at 38.51° . Several works on AlN thin film showed XRD peak at 36.02° [297], 36.10° [298] and 36° [294]. Ti peak was observed at 38.35° in [10]. The measured values of peak position of both AlN and Ti are very close to the literature values.

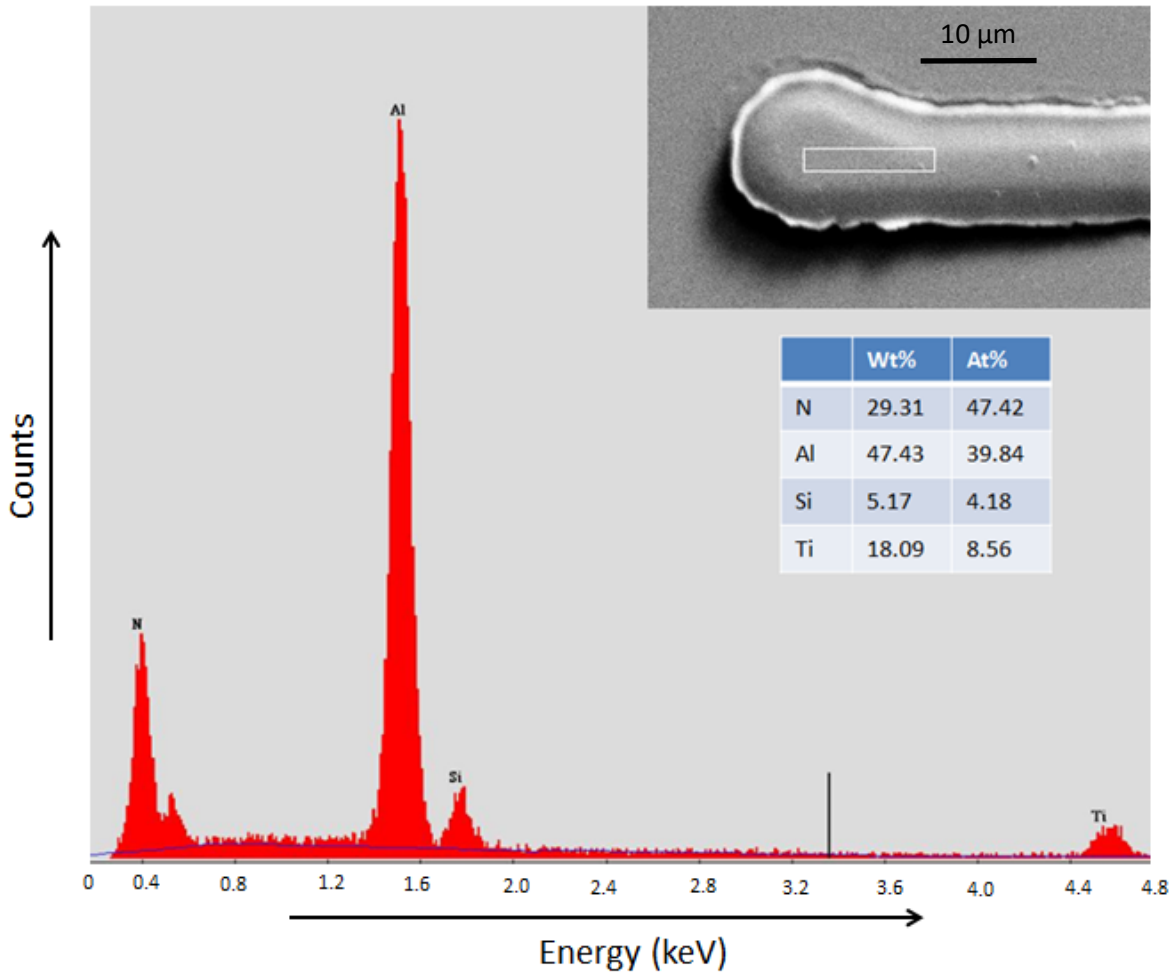


Figure 7-13 Results of the EDX analysis done on the fabricated cantilever

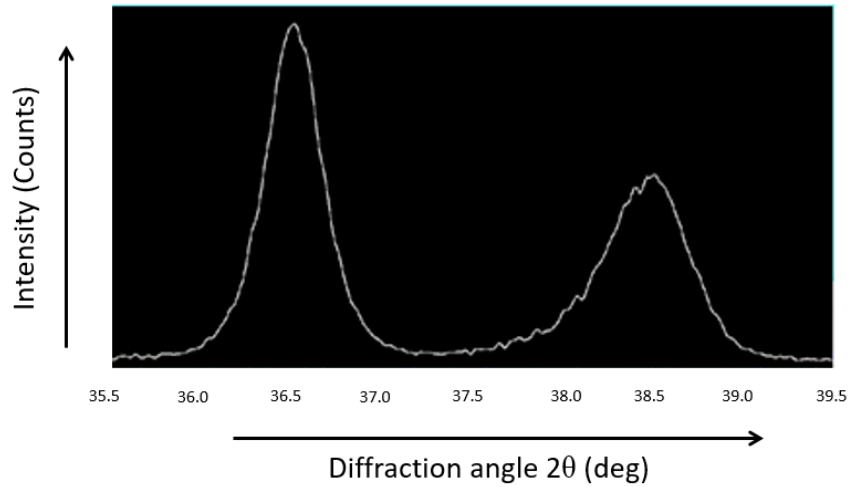


Figure 7-14 XRD on AlN cantilever revealing crystal orientation of AlN along 36.54° and Ti along 38.51°.

7.7 Characterization

7.7.1 Setup

The completely fabricated AlN cantilevers were characterized using the measurement setup shown in Figure 7-15. The signal generator LFG 1300S was connected with the PZT E665 controller which drives the nanopositioner. The load cell displays the applied force on the cantilever in grams. Micromanipulator probe model 7B-5 with a radius of 5 μm was used to apply a vertical force on the AlN cantilever. The applied pressure was calculated from the cross-sectional area of the probe and the applied

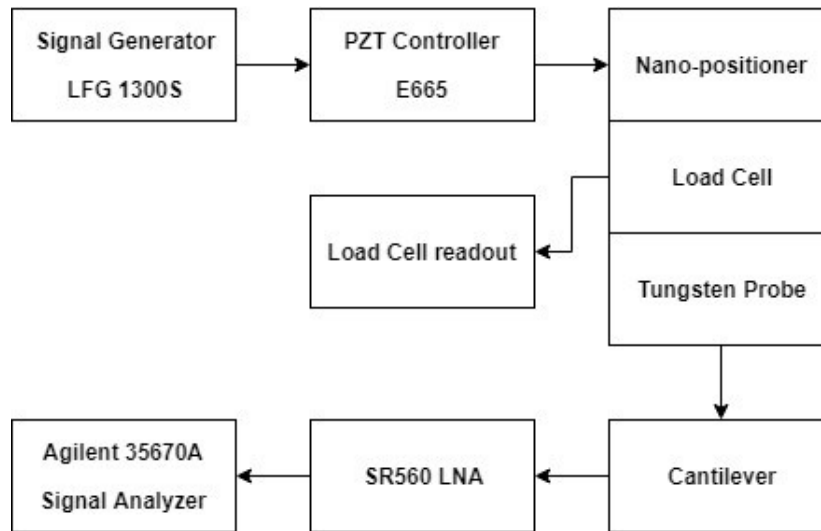


Figure 7-15 Block diagram of the measurement setup

force reading from the load cell readout display. The response from the cantilever was fed to a SR560 low noise amplifier and finally to an Agilent 35670A signal analyzer.

Before starting the characterization, zero-point adjustment in E-665 PZT controller was completed. This calibration ensures the full travel range of the nanopositioner. The generated signal from the signal generator was amplified 10 times and was displayed in the front panel of the E-665 PZT controller. The DC voltage amplified by the PZT E-665 controller for 2 μm displacement was 6.13 V as shown in Figure 7-16. Therefore, 0.613 V of input voltage into the PZT 665 controller results in 2 μm displacement. With a probe of 5 μm tip radius, the minimum resolution of applied pressure was calculated to be 103 kPa.

7.7.2 Sensitivity

For sensitivity analysis, various amounts of pressure were applied and the corresponding output voltages from the cantilevers were calculated. Figure 7-17 shows the output voltages vs displacements of three cantilevers of same size whereas, Figure 7-18 displays output voltages vs applied pressures for the same cantilevers. The sensitivities were calculated from the slope of the output voltage vs pressure curve. The calculated sensitivities were 2.04×10^{-4} V/kPa, 1.90×10^{-4} V/kPa and 1.98×10^{-4} V/kPa.



Figure 7-16 PZT E-665 front panel displaying the required voltage for 2 μm displacement

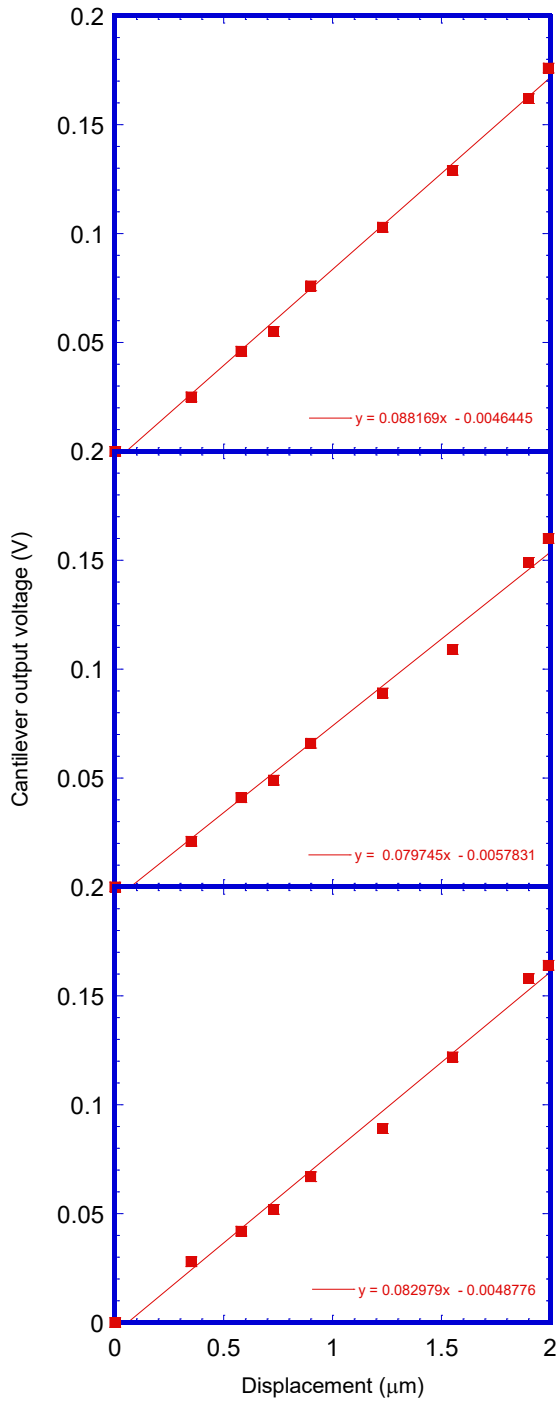


Figure 7-17 Cantilever output voltage plotted against cantilever displacement

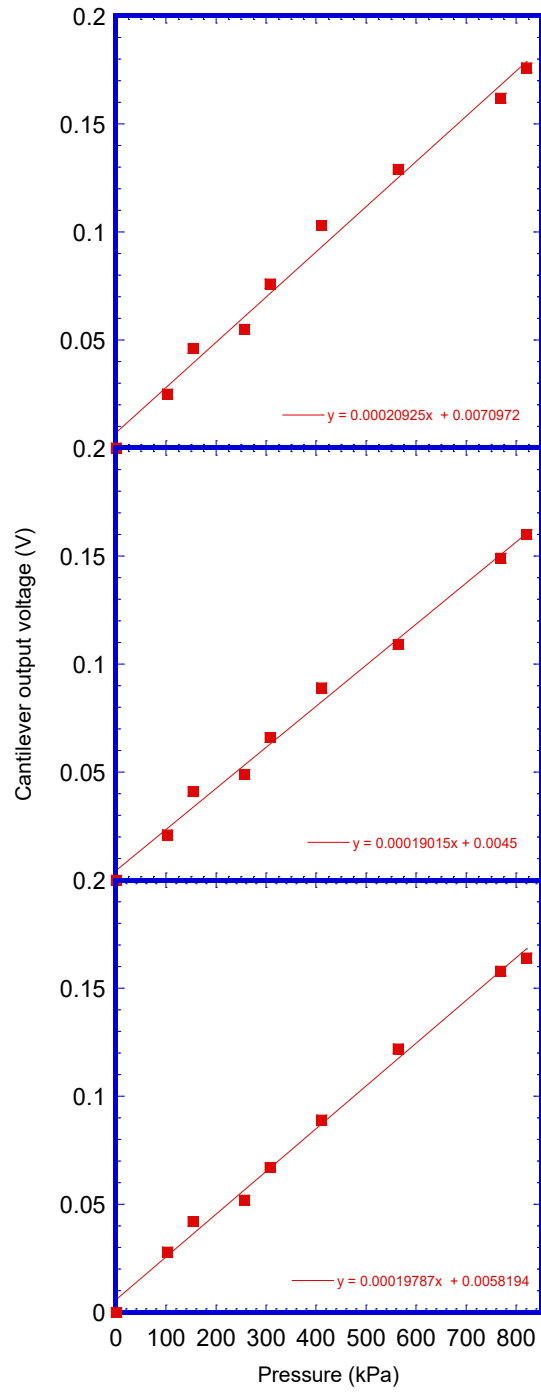


Figure 7-18 Cantilever output voltage plotted against applied pressure on cantilever

7.7.3 Frequency response

Sinusoidal voltages with amplitude of 0.613 V were applied with a frequency range between 3 Hz and 15 Hz. The output voltages from the cantilever at those frequencies were also measured. Figure 7-19 (a) and (b) show the sinusoidal input and the corresponding output at 3 Hz from the cantilever, respectively.

The power spectral density of the output voltage at 3 Hz is shown in Figure 7-20. A peak at 3 Hz and harmonics with smaller amplitude were observed but no low frequency noise was found. The output voltages from the cantilever for input voltages at 5 Hz, 8 Hz, 10 Hz and 15 Hz are shown in Figure 7-21.

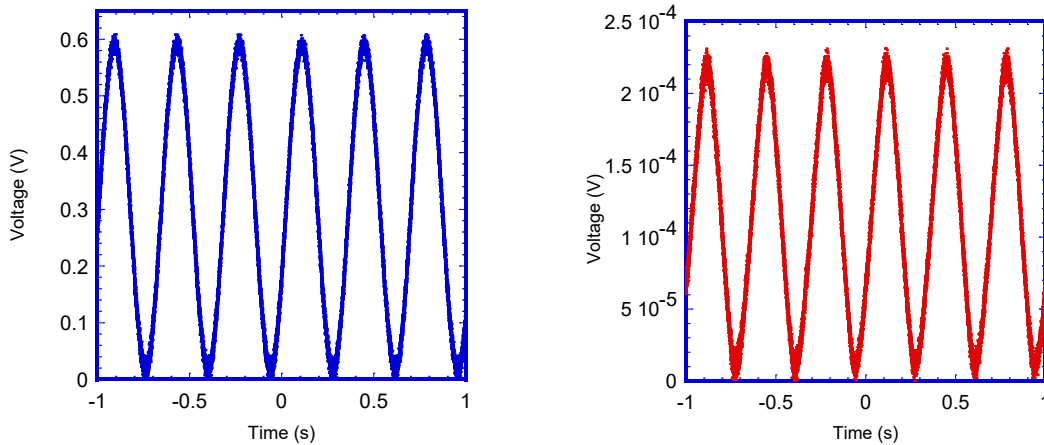


Figure 7-19 (a) Input voltage at the frequency of 3 Hz to E-665 PZT and (b) output voltage at the frequency of 3 Hz from cantilever

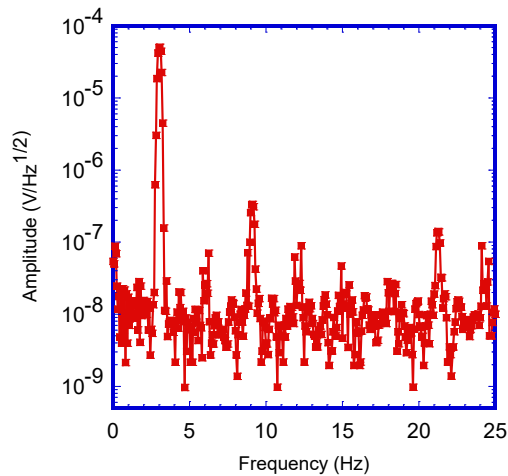


Figure 7-20 Power spectral density of the output voltage from Figure. 7-19 (b)

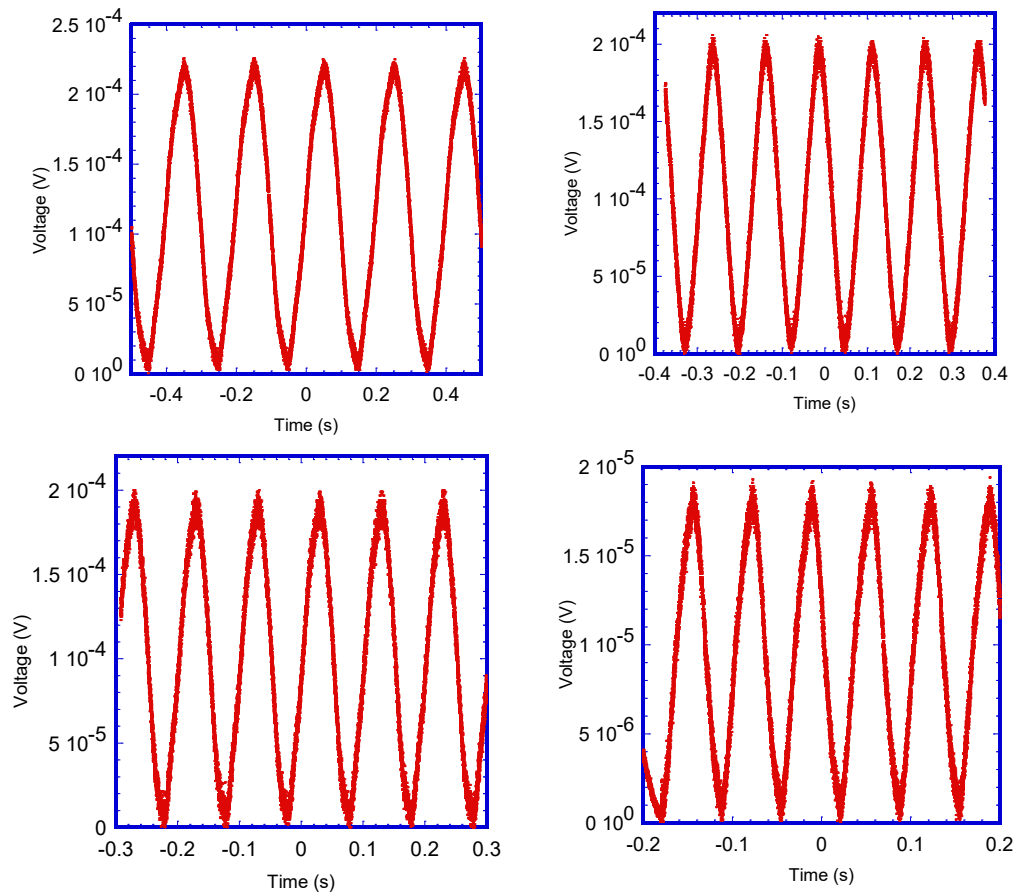


Figure 7-21 Output voltages from the cantilever for the input voltages of (a) 5 Hz, (b) 8 Hz, (c) 10 Hz and (d) 15 Hz

In all the cases, the output followed the incoming vibrations. The peak value of the output voltage from the cantilever dropped when the input vibration is at 15 Hz as shown in Table 7-1. The output at 15 Hz is a little distorted as well. For the ultra-thin AlN layer, the dipoles can quickly change the direction of polarization in response to the incoming vibration at 10 Hz or below. At higher frequency, the dipoles therefore do not get enough time to rearrange. Typically, the frequency of the activities performed by human motions is less than 5 Hz [299]. The excellent low frequency responses from the cantilevers make them suitable for tactile sensing and pressure measurement from everyday human activities.

Table 7-1 Comparison among peak output voltages from the cantilever at different frequencies

Frequency (Hz)	Peak output voltage (V)
3	2.31×10^{-4} V
5	2.24×10^{-4} V
8	2.04×10^{-4} V
10	1.98×10^{-4} V
15	1.92×10^{-5} V

7.8 Summary

This Chapter provided the details of design, fabrication and characterization of ultra-thin AlN cantilever on flexible substrate. The AlN was deposited at room temperature and annealed after ashing the sacrificial layer. The glass transition temperature of the flexible substrate (400 °C) was the highest processing temperature. The annealing temperature in the final step of the fabrication was therefore set at 380 °C. XRD on the annealed cantilevers showed perfect orientation angle of the dipoles of the piezoelectric layer as well as the contact layer. The sensitivity of the cantilever was measured to be 2.04×10^{-4} V/kPa for the cantilever size of $60 \mu\text{m} \times 12 \mu\text{m} \times 0.25 \mu\text{m}$. This work has demonstrated that for ultra-thin AlN cantilevers, annealing can be done after suspending the cantilevers and retain the piezoelectric property at the same time.

Chapter 8

Conclusion

8.1 Choice of flexible substrate

MEMS researchers have developed microsensors over the past few decades, for a variety of sensing applications including inertial force, temperature, pressure, chemical species and radiation. Introduction of flexibility in MEMS devices has enhanced their features by adding the capability to bend which is not realizable with the rigid counterparts. Wearable devices are often required to be mounted on curved surfaces like human body. Utilizing flexible polyimides as a substrate can help with bendability of MEMS devices. Low T_g exhibited by many polyimides was one of the main drawbacks of previous fabrication processes for flexible substrates. Moreover, releasing the substrate using liquid solvents like acetone or methanol was common. Liquid solvents lead to stiction in miniature MEMS devices. To overcome these limitations, a polyimide having a high T_g and a process of dry ashing are essential. In this work, design, fabrication and characterization of MEMS capacitive accelerometers on a flexible polyimide are presented. A low adhesion strength release layer PI2611 was used under the substrate that eliminated the solvent requirement to release the substrate. It also possesses a low CTE value, very close to that of Si. As a flexible substrate, PI5878G was chosen considering the factors including T_g and CTE. High T_g (> 400 °C) and low CTE (20 ppm/°C) make PI5878G a very attractive polyimide for the fabrication of flexible accelerometers.

8.2 Novel design of flexible accelerometers

Design of the accelerometers was completed in CoventorWare[®] software. Capacitance simulations were done in CoSolveEM module and other simulations including stress and modal analyses, pull-in studies were completed in MemMech module. A novel UV-LIGA fabrication technique was developed to realize a thicker proof-mass (8 μm) compared to the spring (3 μm), thus decoupling the two important parameters: the stiffness and the proof-mass to achieve higher sensitivity. Optimization of

thicknesses of the spring and the proof mass, perforations and sacrificial layer were done to have the highest sensitivity and desired resonant frequency.

Accelerometers of three different sizes, tuned to frequencies ranging from 600 Hz to 1100 Hz, were fabricated. The perforated proof mass of the accelerometers aided the ashing process of the sacrificial polyimide. The perforations also reduce the damping force. The largest device, having the area of $960\ \mu\text{m} \times 960\ \mu\text{m}$, showed a sensitivity of 187 fF/g with an SNR of at least 100:1 when characterized at its resonance frequency of 800 Hz. The applied acceleration was $\pm 4\ \text{g}$ in addition to gravitation.

8.3 Flexible packaging of accelerometers

The MEMS capacitive micro accelerometers designed and fabricated in this work on flexible substrates were later packaged by a Kapton[®] superstrate. Kapton[®] was chosen because of several beneficial factors including similar T_g and CTE compared to substrate PI5878G, low outgassing in vacuum, high tensile strength and chemical inertness to numerous solvents. To form the sidewall between the substrate and the superstrate, HD4110 polyimide was utilized since its T_g and CTE values are close to those of PI5878G and Kapton[®].

All three types of accelerometers were characterized after encapsulation. The performance of the accelerometers was enhanced after packaging which is attributed to the fact that packaging creates a neutral stress plane in between the substrate and the superstrate and the accelerometers were placed close to that plane. After packaging, the largest accelerometer A960 demonstrated a sensitivity of 195 fF/g at its resonant frequency of 800 Hz. The characterization results from other accelerometers and a comparative study of sensitivity of all the three sizes of accelerometers before and after encapsulation are detailed.

8.4 AlN tactile sensors

Cantilever based AlN pressure sensors with a capability of detecting pressure from 100 kPa to 850 kPa were fabricated and characterized as part of the final project. The details of fabrication and

characterization process are described. The AlN cantilevers sandwiched between two Ti electrodes demonstrated excellent crystal orientation along 36.54° . The cantilevers were fabricated on a flexible PI5878G polyimide which limited the maximum annealing temperature at 400°C . These surface micromachined AlN cantilevers demonstrated a sensitivity ranging from 1.90×10^{-4} V/kPa to 2.04×10^{-4} V/kPa.

8.5 Applications

Flexible accelerometers fabricated in this work introduce several potential applications. The major advantages of the process demonstrated here are the bendability of the device, lightweight, low profile and low fabrication cost. The devices fabricated by double UV-LIGA process demonstrated six-fold increase in sensitivity compared to the state-of-the-art currently available. The accelerometers were characterized after bending down to 2.0 cm ROC. Therefore, these devices can be easily mounted on robotic or prosthetic fingertips. The possible applications of the encapsulated flexible MEMS capacitive accelerometer are:

- To provide feedback to the wearer of a prosthetic component for motion control
- To maintain and control robotic motion to ensure safety of human co-workers
- Nonintrusive measurement of exercise parameters on clothing (wearables)
- Integrated measurement system for physical therapy
- Navigation in defense and commercial aviation
- Control and stabilize unmanned vehicles by accurate inertial sensing
- Air bag deployment system and game controllers

AlN pressure sensors, on the other hand, can be used for tactile pressure sensing from human gloves, press by index finger or pressure from the grasping of a cylinder.

Appendix A

Accelerometer mask layouts

A.1 Introduction

Accelerometers of three different geometries were designed in this work. CoventorWare[®] requires a process flow and a layout to build a solid model. Here, mask layout of A640 is presented.

A.2 Mask layouts

After defining the process flow, the mask layout is prepared in CoventorWare[®] software. A total

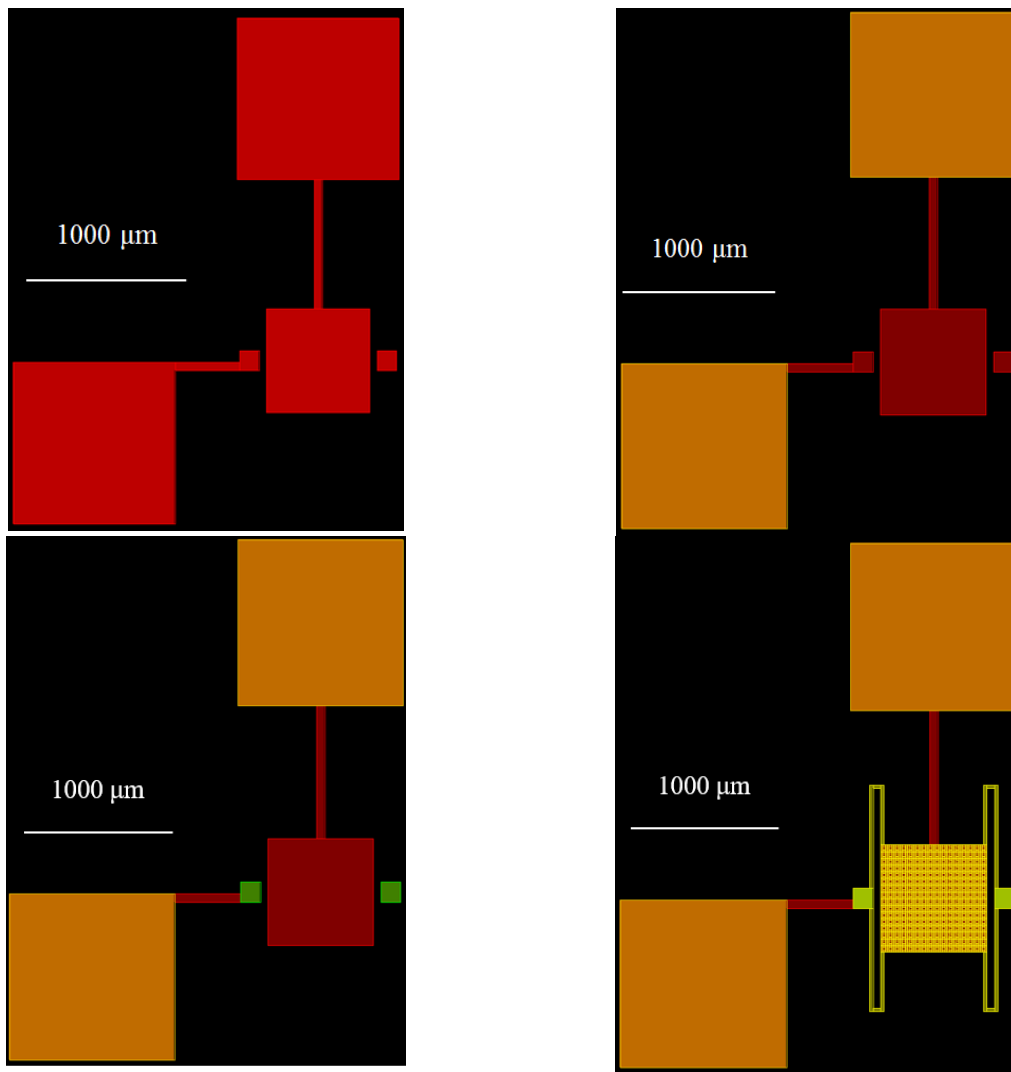


Figure A-1 Layout for A640 (a) bottom electrode, (b) bond pad, (c) sacrificial layer, (d) Au seed layer

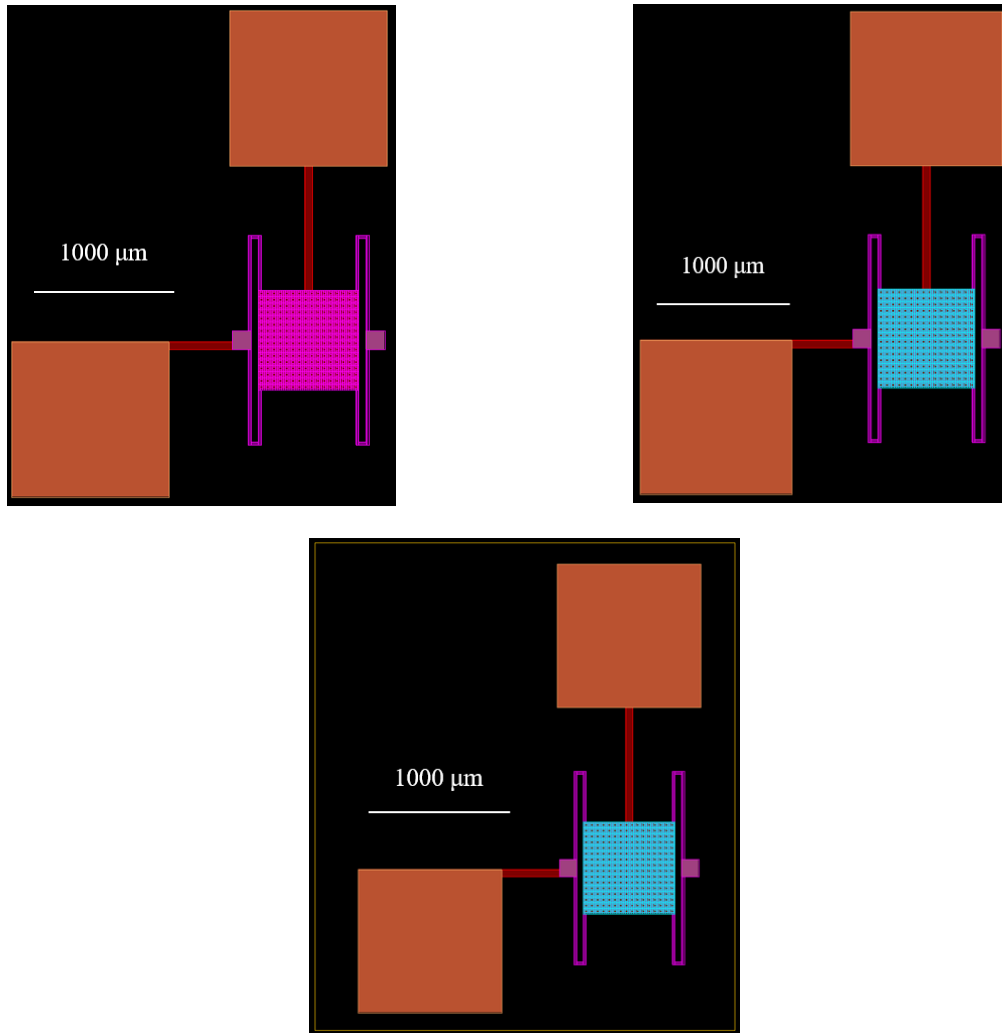


Figure A-1 (continued) Layout for A640 (e) 1st Ni layer (f) 2nd Ni layer (g) cavity

of 6 masks were used to design the accelerometers. The mask layouts are provided below. For Au seed layer and for 1st Ni layer, same mask was used. These layouts were converted to Graphic Data System (GDS) file and provided to the mask suppliers.

A.3 Summary

The layout files of the accelerometers were created to build the solid model and subsequently perform the simulations.

Appendix B

CoSolveEM settings for accelerometer capacitance simulation

B.1 Introduction

Simulations including capacitance change, modal analysis and stress study were performed on the three different sizes of accelerometers. The simulation settings are provided in this Appendix.

B.2 CoSolveEM settings

CoSolveEM is an individual module of CoventorWare® that has the capability of electromechanical analysis. MemElectro provides the electrostatic analysis, and MemMech provides the mechanical analysis. CoSolveEM uses an iterative procedure to maintain consistency between the two solutions. It checks the mechanical deformation for applied electrostatic force and direct towards convergence for a given set of settings. In this work, electrostatic force was applied between the electrodes and acceleration was applied on the proof mass. The combined effect is simulated in CoSolveEM module.

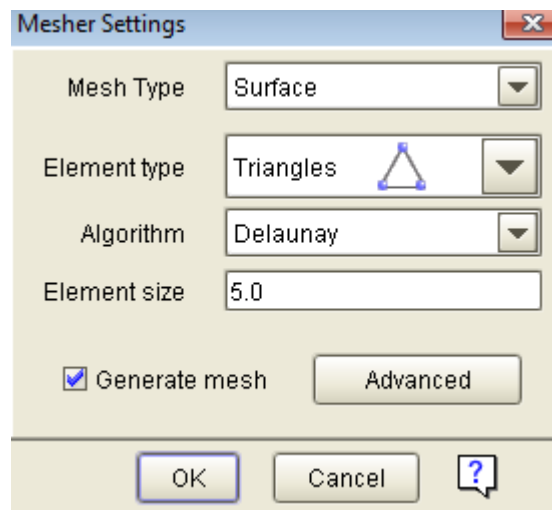


Figure B-1 Mesher settings for splitting planes

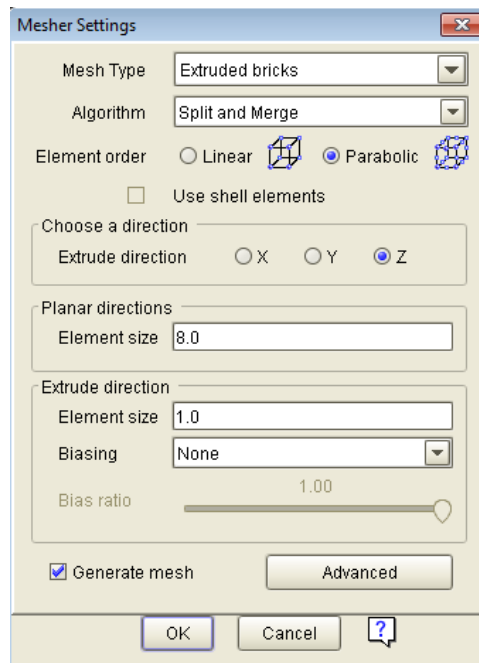


Figure B-2 Mesher settings for the accelerometers

Figures B-1 and B-2 show the mesh settings for the splitting planes and accelerometer solid model respectively. Planes can only be meshed with surface mesh type. Smaller 3-node triangles element was selected over quadrilateral element. Delaunay algorithm is the only available one for triangular element. It requires the satisfaction of the criterion that no node may be contained by the circumcircle of

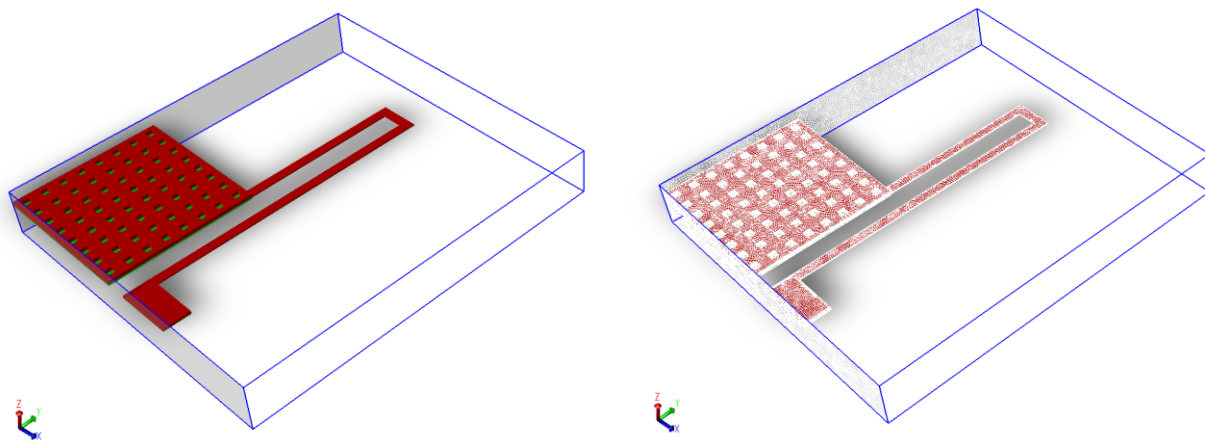


Figure B-3 (a) Solid model of quarter size of accelerometer A640 and (b) after generating mesh

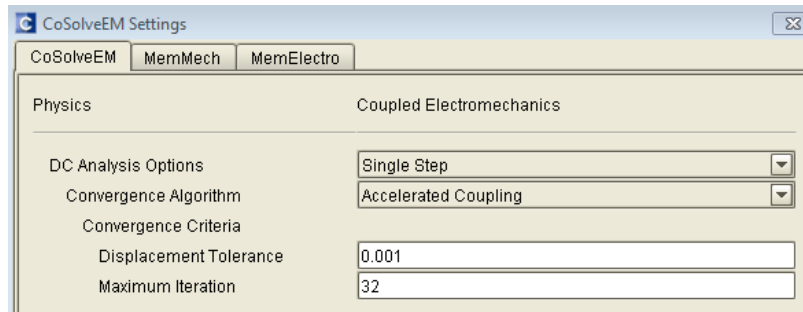


Figure B-4 CoSolveEM settings

any other triangle. Extruded brick meshing was applied to the whole accelerometer including the proof mass, the springs and the anchors. This mesh type automatically reduces the element size wherever it finds an interface. For example, at the interface between the proof mass and the springs, two layers of different thicknesses are connected. Extruded brick scheme makes quadrilateral meshes and then extrudes the meshes in the given extruded direction to form hexahedral bricks. Figure B-3 shows a quarter size of the solid model (a) before meshing and (b) after meshing. Split and merge algorithm was selected because it splits the quadrilaterals and merges them to produce the finest quality of mesh. Parabolic element order ensures that there is always three nodes along each mesh edge for greater accuracy than linear element which produces two nodes per mesh edge.

The simulation settings in CoSolveEM, MemMech and MemElectro are displayed in Figures B-4, B-5 and B-6 respectively. Since a small DC voltage is applied between the proof mass and the bottom electrode later, single step DC analysis was selected with accelerated coupling algorithm for faster convergence. The tolerance of displacement was set at 0.001 μm . CoSolveEM iterates the electrostatic and mechanical solutions until the difference between every corresponding pair of elements of the two displacement vectors, at the current iteration and the previous, is less than this setting. Maximum iteration of 32 or higher value result in same displacement of the proof mass. That is why the maximum iteration was set at 32.

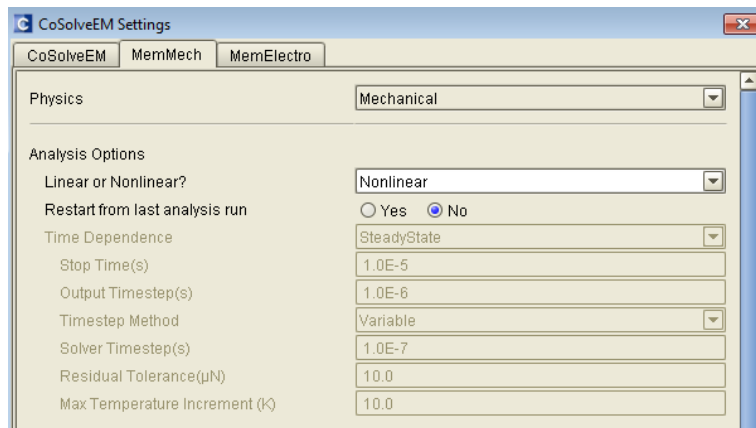


Figure B-5 MemMech settings

To include the geometric nonlinearity in the analysis, the analysis option was set as nonlinear as shown in the MemMech settings in Figure B-5. MemElectro setting (Figure B-6) includes electrostatics analysis with the option of force on conductor parts since acceleration is applied of the proof mass.

The boundary conditions are applied afterwards. CoSolveEM requires a potential difference between the electrodes for capacitance simulation. Figure B-7 shows that a small DC voltage of 50 mV was applied to the proof mass whereas the bottom electrode was grounded.

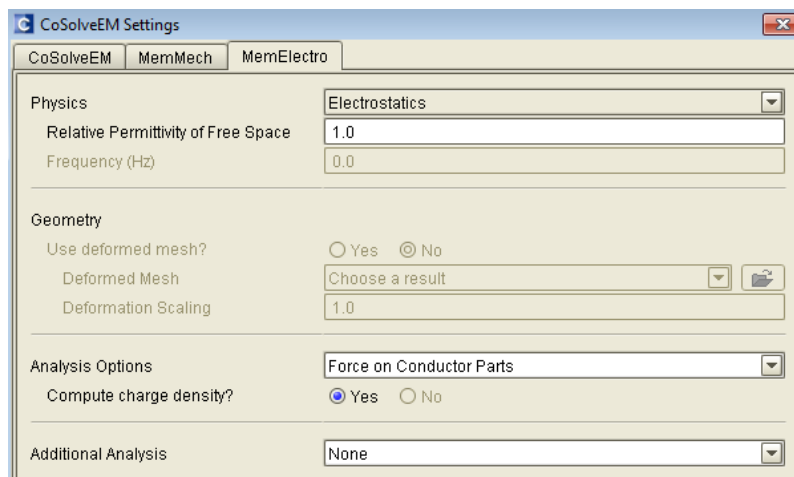


Figure B-6 MemElectro settings

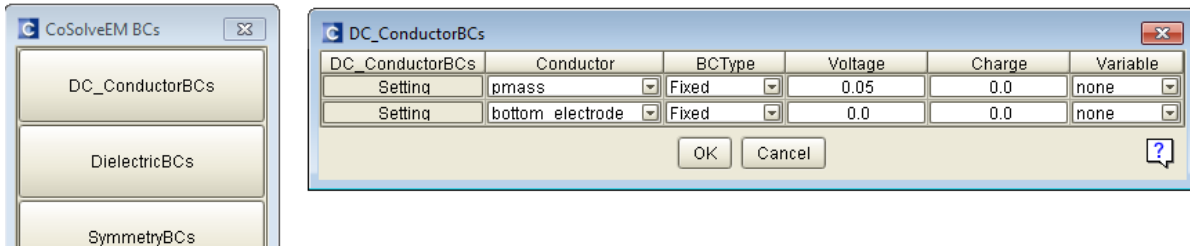


Figure B-7 50 mV applied to the proof mass with respect to the bottom electrode

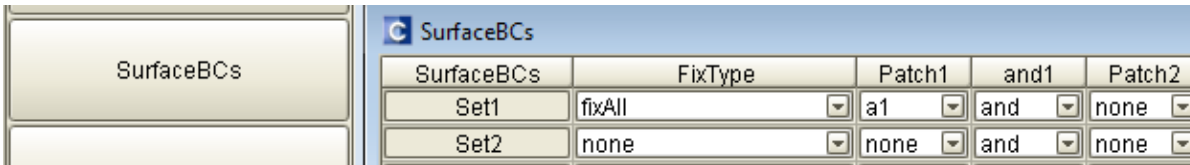


Figure B-8 The bottom surface of the anchor is fixed in all direction in SurfaceBCs settings box

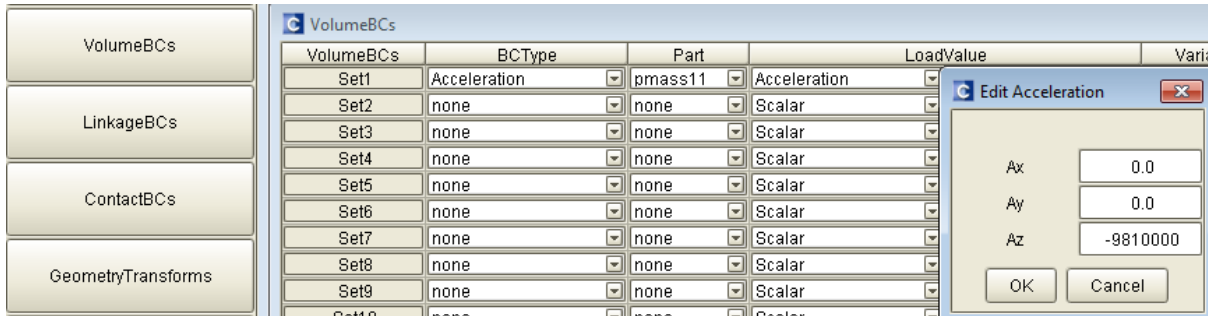


Figure B-9 Acceleration applied on the proof mass in VolumeBCs settings box

The surface and volume boundary conditions are presented in Figures B-8 and B-9 respectively. The bottom surface of the anchor was fixed in all direction and acceleration was applied on the proof mass.

B.3 Summary

The simulation settings in CoSolveEM have been described in this Appendix. CoSolveEM requires sufficient meshing for convergence and as well the boundary conditions for electrostatic and mechanical simulations.

Appendix C

Modal and pull-in simulation settings for accelerometers

C.1 Introduction

Modal simulation was carried out to find the resonant frequency and displacements at other modal frequencies. The pull-in analysis is also required to determine the applicable electrostatic force limit. The simulation settings for modal and pull-in analyses are shown in this Appendix.

C.2 Modal analysis settings

A total of 6 modes was selected as shown in the MemMech settings box as shown in Figure C-1. The Lanczos solution method was selected for faster convergence for a non-linear system.

C.3 Pull-in analysis settings

CosolveEM module was utilized to perform the pull-in analysis. The analysis option is shown in Figure C-2. Pull-in detection was selected for the analysis with relaxation iteration method. This method

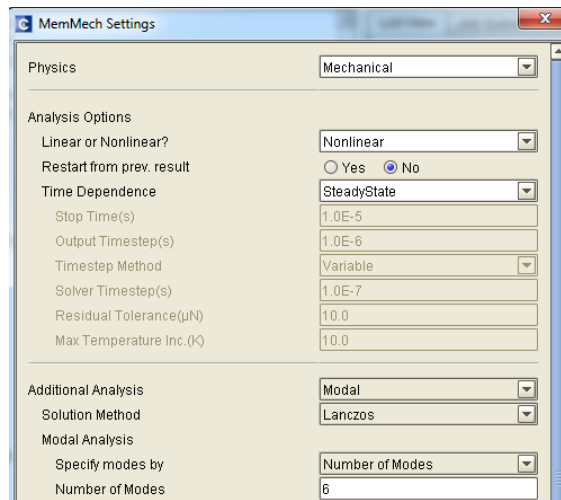


Figure C-1 MemMech settings for modal analysis

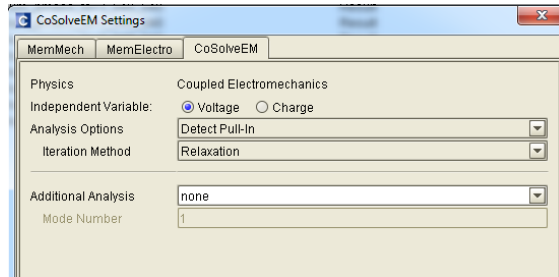


Figure C-2 CoSolveEM settings for pull-in analysis.

requires less computational resources and parametric tuning than Newton's method. Newton's method is only recommended for the rare cases when the relaxation method solver fails to converge.

The voltage was initiated from 10 V and the maximum limit was set at 40 V. The simulator will apply 10 V initially and find out whether this is the pull-in voltage or not. If not, it will increase 1 V in each step and redo the simulation again. Once the pull-in voltage is reached, it will stop. These settings are shown in Figure C-3.

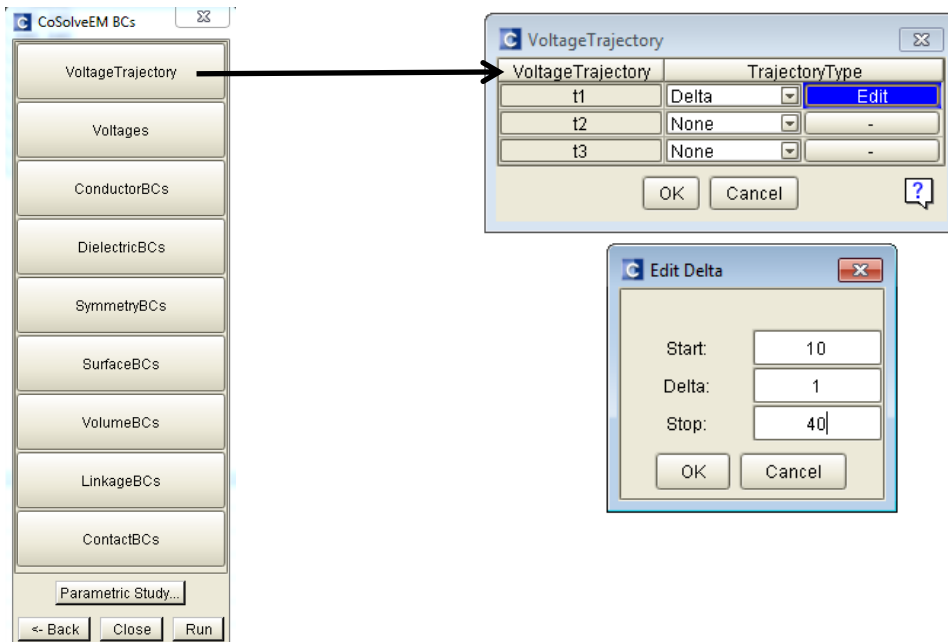


Figure C-3 Voltage trajectory settings box

C.4 Summary

The simulation settings for the modal and pull-in analysis have been described in this Appendix. Modal analysis is essential to determine the resonant frequency and confirm the movement of a structure in desired direction. For capacitive accelerometers, limiting the applied voltage below the pull-in voltage is necessary. Pull-in analysis helps to find out the pull-in point.

Appendix D

Simulation settings for bending of accelerometers

D.1 Introduction

The substrates of the accelerometers were bent to check the flexibility. This Appendix provides the simulation settings for bending the substrates.

D.2 Simulation settings

Figure D-1 shows the cross section of the solid model of A960 encapsulated by Kapton[®] superstrate. To simulate the bending, one end of the substrate as kept fixed and displacement was applied at the other end. In both ends, the surfaces include the polyimide substrate, the insulator, the sidewall and the Kapton[®] superstrate. Figures D-2 and D-3 displays the applied surface and volume boundary conditions.

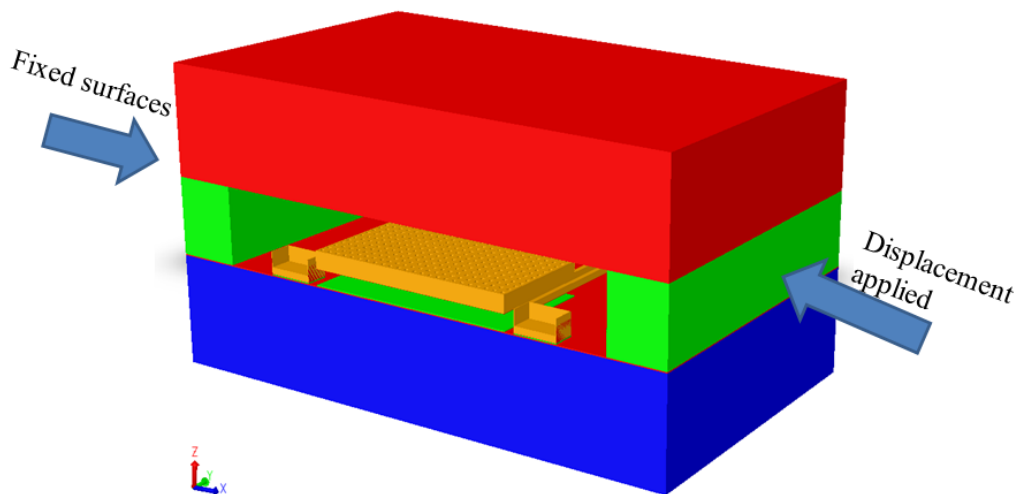


Figure D-1 Cross section of the solid model of A960 showing the fixed surfaces and the direction of applied displacement. Z-axis exaggerated 10 times.

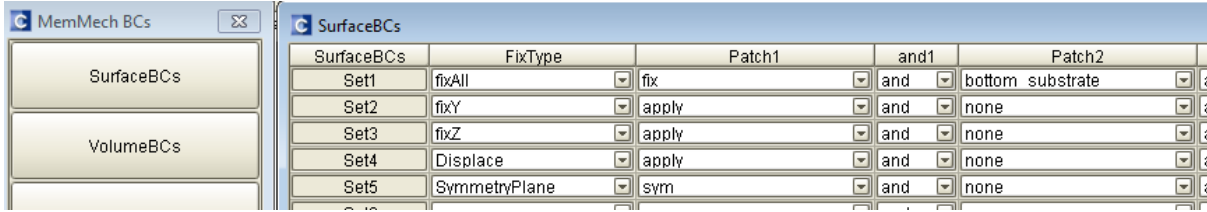


Figure D-2 Boundary conditions in SurfaceBCs settings box

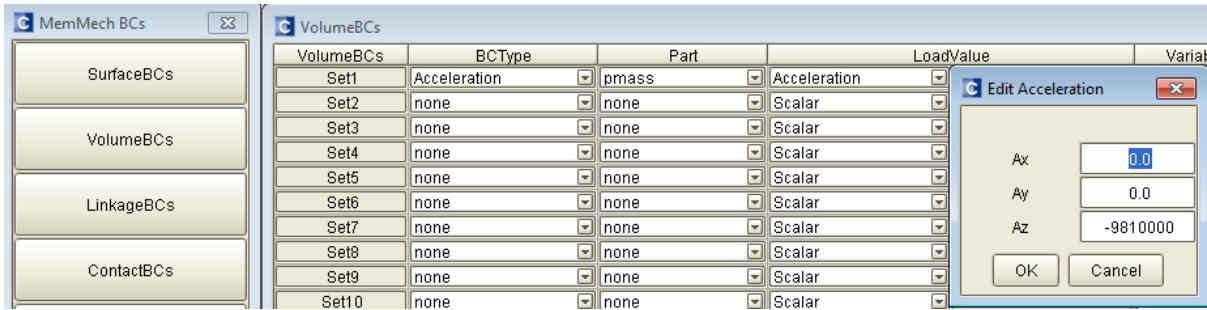


Figure D-3 Acceleration applied in VolumeBCs settings box

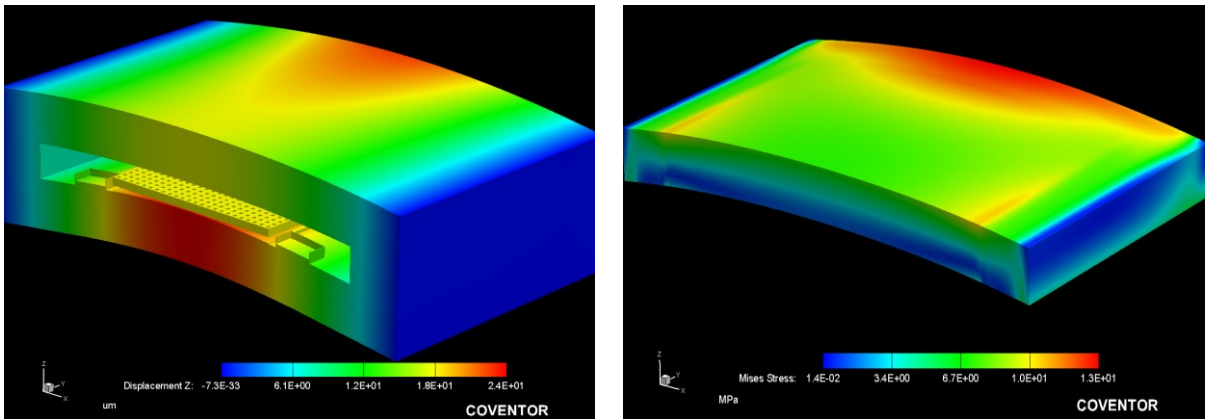


Figure D-4 (a) Displacement and (b) stress in visualizer

Once the simulation was completed, the displacement and stress at different layers were viewed in Visualizer as shown in Figure D-4 (a) and (b) respectively.

D.3 Summary

Stress at all layers upon bending must be below the yield strength. Therefore, stress simulation is essential to check the level of stress. This Appendix describes the required simulation settings.

Appendix E

Calculations of ROC

E.1 Introduction

The accelerometers were bent by applying displacement at one end and fixing the other end in all direction as described in Appendix C. Here, the calculations of determining the ROC from the bent proof mass is discussed.

E.2 Determining ROC

Figure E-1 shows accelerometer A960 bent when displacement is applied at one end. The bottom electrode comes very close to the proof mass so that both parts are almost touching each other. Once the structure is bent, x and y coordinated from the simulation were extracted. The radius of curvature was determined from Eq. (E-1) [300]

$$R = [1 + (y'(x))^2]^{3/2} / |y''(x)| \quad (\text{E-1})$$

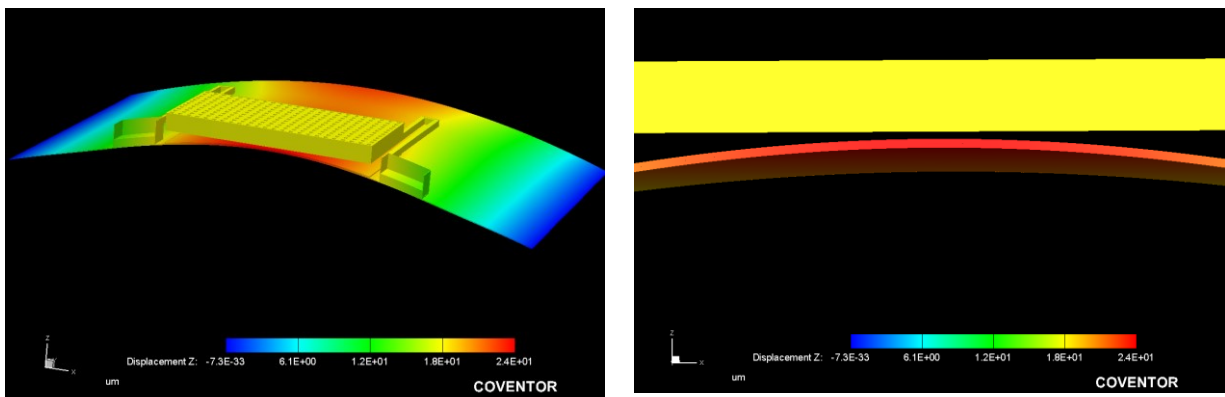


Figure E-1 (a) A960 bent down to 2.5 cm ROC and (b) the bottom electrode coming closer to the proof mass

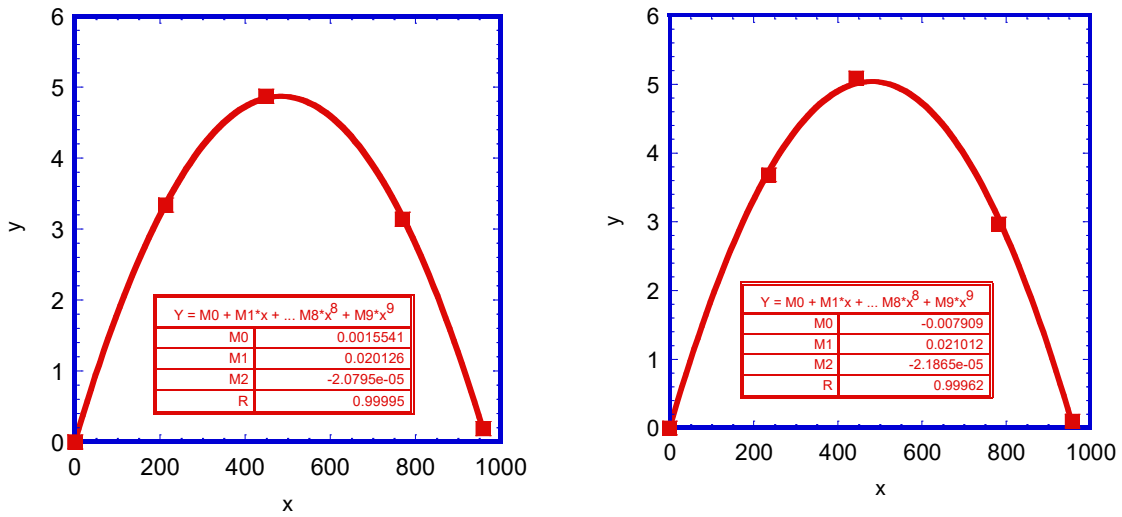


Figure E-2 ROC calculation (a) without Kapton[®] and (b) with Kapton[®]

where, x and y are the coordinate values, y' and y'' are the first and second derivative of the function that defines the curvature. The function was obtained by curve fitting on the simulated points. Two different sets of points were extracted; one with Kapton[®] and one without Kapton[®]. Figures D-2 and D-3 show the fitted curve for the two cases. Utilizing Eq. (D-1), the calculated ROCs in both cases are determined at 2.5 cm. Figure E-2 (a) and (b) show the curvature of the substrate before encapsulation and after encapsulation respectively.

E.3 Summary

The minimum ROC of the accelerometer was calculated to be 2.5 cm when the bottom electrode almost touches the proof mass. This indicates the minimum bendable ROC for the accelerometers when it can still stay functional.

Appendix F

AIN pressure sensor simulation settings

F.1 Introduction

Simulation was carried out to determine the maximum applicable load on the cantilevers. This Appendix describes the required simulation settings.

F.2 Simulation settings

Figure F-1 shows the mesher settings for the solid model of the cantilever. Since the cantilever is a rectilinear structure without a complex interface, Manhattan bricks were selected as the mesh type. Smaller mesh was applied in z-direction to confirm the availability of sufficient segments in z-direction.

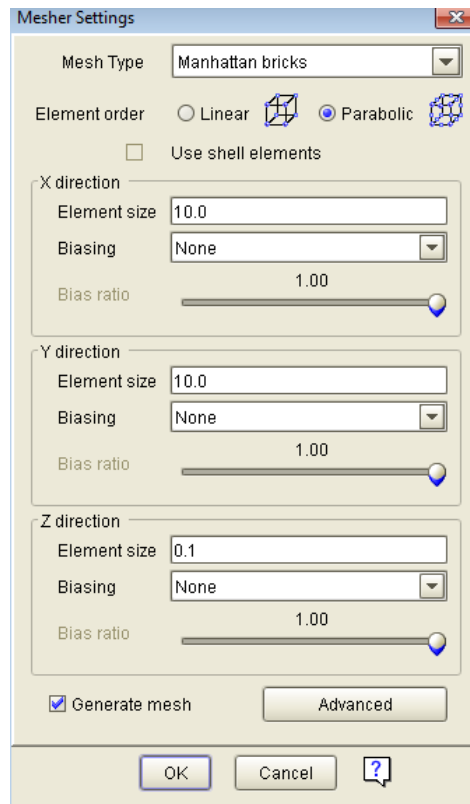


Figure F-1 Fixing the anchor of the cantilever in all directions and applying pressure on the cantilever tip

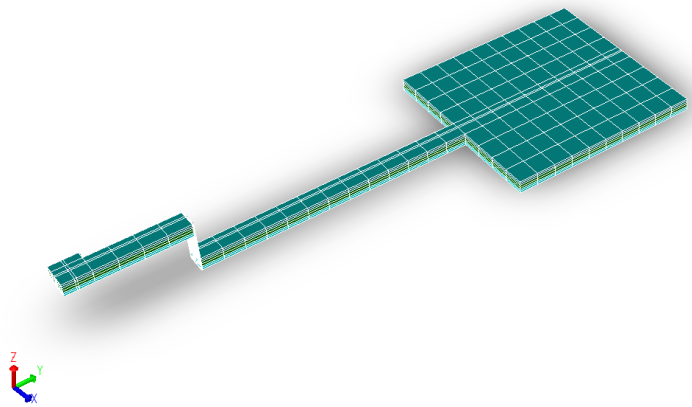


Figure F-2 Solid model after meshing. Z-axis exaggerated 5 times.

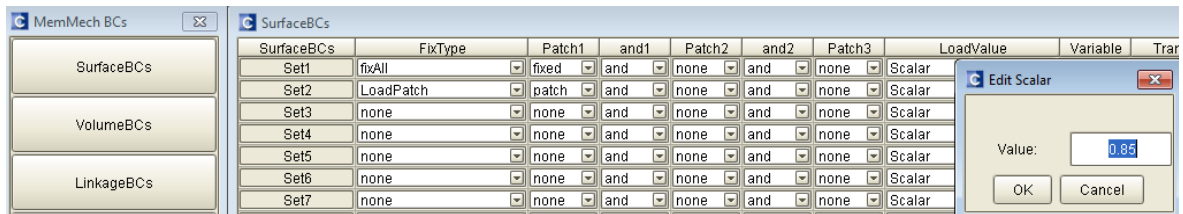


Figure F-3 Fixing the anchor of the cantilever in all directions and applying pressure on the cantilever tip

The solid model after meshing is shown in Figure F-2. MemMech surface boundary conditions are displayed in Figure F-3. After simulation, the displacement as well as the stress was observed in the Visualizer.

F.3 Summary

This Appendix has described the MemMech simulation settings for AlN cantilever. Upon bending of the cantilever, the stresses at different layers were observed.

References

-
- [1] K. Maenaka, "MEMS inertial sensors and their applications," *Int. Conf. on Netw. Sensing Syst.*, Kanazawa, pp. 71-73, 2008.
- [2] T. Xie, H. Xie, G. K. Fedder and Y. Pan, "Endoscopic optical coherence tomography with new MEMS mirror," *Electron. Lett.*, vol. 39, no. 21, pp. 1535-1536, 2003.
- [3] H. Zhang, M. D. Poliks, B. Sammakia, S. Garner, J. Miller and J. Lyon, "Micron-Sized Feature Overlay Alignment on Large Flexible Substrates for Electronic and Display Systems," *J. of Display Tech.*, vol. 7, no. 6, pp. 330-338, June 2011.
- [4] M. H. Iqbal, A. Aydin, O. Brunckhorst, P. Dasgupta and K. Ahmed, "A review of wearable technology in medicine," *J. of the Royal Society of Med.*, vol. 109, no. 10, pp. 372-380, 2016.
- [5] E. Cochran, J. Lawrence, C. Christensen and A. Chung, "A novel strong-motion seismic network for community participation in earthquake monitoring," *IEEE Instrum. & Meas. Mag.*, vol. 12, no. 6, pp. 8-15, 2009.
- [6] L. Țepelea, I. Gavriluț and A. Gacsádi, "Smartphone application to assist visually impaired people," *Int. Conf. on Eng. of Modern Electric Syst.*, Oradea, 2017, pp. 228-231.
- [7] J. Marek, "Automotive MEMS sensors — Trends and applications," *Int. Symp. on VLSI Technol., Syst. and Appl.*, Hsinchu, pp. 1-2, 2011.
- [8] M. S. Mahmood, Z. Celik-Butler and D. P. Butler, "Wafer-level packaged flexible and bendable MEMS accelerometer for robotics and prosthetics," *IEEE Sensors Appl. Symp.*, Glassboro, NJ, 2017, pp. 1-5.
- [9] B. Y. Ahn, E. B. Duoss, M. J. Motala, X. Guo, Sang-Il Park, Y. Xiong, J. Yoon, R. G. Nuzzo, J. A. Rogers and J. A. Lewis, "Omnidirectional printing of flexible, stretchable, and spanning silver microelectrodes," *Sci.*, vol. 323, no. 5921, pp. 1590-1593, 2009.
- [10] M. L. Hammock, A. Chortos, B. C. K. Tee, J. B. -H. Tok, and Z. Bao, "25th anniversary article: the evolution of electronic skin (e-skin): a brief history, design considerations, and recent progress," *Adv. Mater.*, vol. 25, pp. 5997–6038, 2013.
- [11] J. J. Wang, M. Y. Lin, H. Y. Liang, R. Chen and W. Fang, "Piezoresistive nanocomposite rubber elastomer for stretchable MEMS sensor," *IEEE Int. Conf. on Microelectromech. Syst.*, Shanghai, pp. 550-553, 2016.

-
- [12] A. Norrissa, M. Saafib and P. Rominec, "Temperature and moisture monitoring in concrete structures using embedded nanotechnology/microelectromechanical systems (MEMS) sensors," *Construction and Building Materials*, vol. 22, no 2, 2008, pp. 111-120, 2008.
- [13] S. Tung, S. R. Witherspoon, L. A. Roe, A. Silano, D. P. Maynard and N. Ferraro, "A MEMS-based flexible sensor and actuator system for space inflatable structures," *Smart Mater. and Structure*, vol. 10, pp. 1230–1239, 2001.
- [14] G. Kotzar, M. Freasa, P. Abel, A. Fleischman, S. Roy, C. Zorman, J. M. Moran and J. Melzak, "Evaluation of MEMS materials of construction for implantable medical devices," *Biomaterials*, vol. 23, no. 13, pp 2737-2750, 2002.
- [15] W. Cheng, J. Wang, Z. Ma, K. Yan, Y. Wang, H. Wang, S. Li, Y. Li, L. Pan and Y. Shi, "Flexible pressure sensor with high sensitivity and low hysteresis based on a hierarchically microstructured electrode," *IEEE Electron Device Lett.*, vol. 39, no. 2, pp. 288-291, 2018.
- [16] S. A. Hasan, S. A. Hasan, D. Gibson, S. Song, Q. Wu, W. P. Ng, G. McHale, J. Dean and Y. Q. Fu, "ZnO thin film based flexible temperature sensor," *IEEE Sensors Conf.*, Glasgow, pp. 1-3, 2017.
- [17] Y. Chen, B. Lu, Y. Chen and X. Feng, "Biocompatible and Ultra-Flexible Inorganic Strain Sensors Attached to Skin for Long-Term Vital Signs Monitoring," *IEEE Electron Device Lett.*, vol. 37, no. 4, pp. 496-499, 2016.
- [18] P. Cosseddu, S. Lai and A. Bonfiglio, "Highly flexible and low voltage organic thin film transistors for wearable electronics and e-skin applications," *IEEE 15th Int. Conf. on Nanotechnol.*, Rome, pp. 1317-1319, 2015.
- [19] M. Amjadi, A. Pichitpajongkit, S. Lee, S. Ryu and I. Park, "Highly stretchable and sensitive strain sensor based on silver nanowire/elastomer nanocomposite," *ACS Nano*, vol. 8, no. 5, pp. 5154–5163, 2004.
- [20] C. Pang, C. Lee and K. Suh, "Recent advances in flexible sensors for wearable and implantable devices," *J. Appl. Polymer. Sci.* vol. 130, no. 3, pp. 1429-1441, 2013,
- [21] T. Yamada, Y. Hayamizu, Y. Yamamoto, Y. Yomogida, A. Izadi-Najafabadi, D. N. Futaba and K. i Hata. "A stretchable carbon nanotube strain sensor for human-motion detection," *Nature Nanotechnol.*, vol. 6, pp. 296-301, 2011.

-
- [22] D. Y. Khang, H. Jiang, Y. Huang, and J. A. Rogers, "A stretchable form of single crystal silicon for high-performance electronics on rubber substrates," *Sci.*, vol. 311, pp. 208–212, 2006.
- [23] C. Mattmann, F. Clemens, and G. Tröster, "Sensor for measuring strain in textile," *Sensors*, vol. 8, no. 6, pp. 3719–3732, 2008.
- [24] S. P. Lacour, J. Jones, S. Wagner, T. Li, and Z. G. Suo, "Stretchable interconnects for elastic electronic surfaces," *Proc. IEEE*, vol. 93, no. 8, pp. 1459–1467, 2005.
- [25] J. A. Rogers, T. Someya and Y. Huang, "Materials and mechanics for stretchable electronics," *Sci.*, vol. 327, no. 5973, pp. 1603-1607, 2010.
- [26] T. Sekitani, T. Sekitani¹, Y. Noguchi¹, K. Hata, T. Fukushima, T. Aida and T. Someya¹, "A rubberlike stretchable active matrix using elastic conductors," *Sci.*, vol. 321, pp. 1468–1472, 2008.
- [27] T. Sekitani, Y. Noguchi, K. Hata, T. Fukushima, T. Aida and T. Someya, "Stretchable active-matrix organic light-emitting diode display using printable elastic conductors," *Nature Mater.*, vol. 8, pp. 494–499, 2009.
- [28] M. Amjadi, Y. J. Yoon and I. Park, "Ultra-stretchable and skin-mountable strain sensors using carbon nanotubes–Ecoflex nanocomposites," *Nanotechnol*, vol. 26, no. 37, p. 375501, 2015.
- [29] U. H. Shin, D. W. Jeong, S. M. Park, S. H. Kim, H. W. Lee and J. M. Kim, "Highly stretchable conductors and piezocapacitive strain gauges based on simple contact-transfer patterning of carbon nanotube forests," *Carbon*, vol. 80, pp.396-404, 2014.
- [30] X. Xiao, L. Yuan, J. Zhong, T. Ding, Y. Liu, Z. Cai, Y. Rong, H. Han, J. Zhou and Z. L. Wang, "High-strain sensors based on ZnO nanowire/polystyrene hybridized flexible films," *Adv. Mater.*, vol. 23, pp. 5440-5444, 2011.
- [31] C. S. Boland, U. Khan, C. Backes, A. O'Neill, J. McCauley, S. Duane, R. Shanker, Y. Liu, I. Jurewicz, A. B. Dalton, "Sensitive, high-strain, high-rate bodily motion sensors based on graphene–rubber composites," *ACS Nano*, vol. 8, no. 9, pp. 8819-8830, 2014.
- [32] D. Kang, P. V. Pikhitsa, Y. W. Choi, C. Lee, S. S. Shin, L. Piao, B. Park, K. Y. Suh, T. Kim and M. Choi, "Ultrasensitive mechanical crack-based sensor inspired by the spider sensory system," *Nature*, vol. 516, pp. 222-226, 2014.
- [33] S. Luo and T. Liu, "Structure–property–processing relationships of single-wall carbon nanotube thin film piezoresistive sensors," *Carbon*, vol. 59, pp. 315-324, 2013.

-
- [34] C. Mattmann, F. Clemens and G. Tröster, "Sensor for Measuring Strain in Textile," *Sensors*, vol. 8, no. 6, pp. 3719-3732, 2008.
- [35] S. Luo and T. Liu, "SWCNT/graphite nanoplatelet hybrid thin films for self-temperature-compensated, highly sensitive, and extensible piezoresistive sensors," *Adv. Mater.*, vol. 25, no. 39, pp. 5650-5657, 2013.
- [36] M. Amjadi, K. Kyung, I. Park, and M. Sitti, "Stretchable, Skin-Mountable, and Wearable Strain Sensors and Their Potential Applications: A Review," *Adv. Func. Mater.*, vol. 26, no. 11, pp. 1678-1698, 2016.
- [37] Y. Wang, L. Wang, T. Yang, X. Li, X. Zang, M. Zhu, K. Wang, D. Wu and H. Zhu, "Wearable and highly sensitive graphene strain sensors for human motion monitoring," *Adv. Func. Mater.*, vol. 24, no. 29, pp. 4666-4670, 2014.
- [38] D.-H. Kim, R. Ghaffari, N. Lu, J. A. Rogers, "Flexible and stretchable electronics for biointegrated devices," *Annu. Rev. Biomed. Eng.*, vol. 14, pp. 113-128, 2012.
- [39] N. Hu, H. Fukunaga, S. Atobe, Y. Liu and J. Li, "Piezoresistive Strain Sensors Made from Carbon Nanotubes Based Polymer Nanocomposites," *Sensors*, vol. 11, no. 11, pp. 10691-10723, 2011.
- [40] L. Cai, L. Song, P. Luan, Q. Zhang, N. Zhang, Q. Gao, D. Zhao, X. Zhang, M. Tu, F. Yang, W. Zhou, Q. Fan, J. Luo, W. Zhou, P. M. Ajayan and S. Xie, "Super-stretchable, Transparent Carbon Nanotube-Based Capacitive Strain Sensors for Human Motion Detection," *Sci. Rep.*, vol. 3, no. 3048, 2013.
- [41] S. Gong, D. T. H. Lai, B. Su, K. J. Si, Z. Ma, L. W. Yap, P. Guo and W. Chen, "Highly stretchy black gold e-skin nanopatches as highly sensitive wearable biomedical sensors," *Adv. Electronic Mater.*, vol. 1, no. 4, p. 1400063, 2015.
- [42] R. Rahimi, M. Ochoa, W. Yu and B. Ziaie, "Highly stretchable and sensitive unidirectional strain sensor via laser carbonization," *ACS Appl. Mater. Interfaces*, vol. 7, no. 8, pp. 4463-4470, 2015.
- [43] J. T. Muth, D. M. Vogt, R. L. Truby, Y. Mengüç, D. B. Kolesky, R. J. Wood and J. A. Lewis, "Embedded 3d printing of strain sensors within highly stretchable elastomers," *Adv. Mater.*, vol. 26, no. 36, pp. 6307-6312, 2014.
- [44] Z. Yu, X. Niu, Z. Liu and Q. Pei, "Intrinsically stretchable polymer light-emitting devices using carbon nanotube-polymer composite electrodes," *Adv. Mater.*, vol. 23, no. 34, pp. 3989-3994, 2011.

-
- [45] Q. Cao, S. H. Hur, Z. T. Zhu, Y. G. Sun, C. J. Wang, M. A. Meitl, M. Shim and J. A. Rogers, "Highly bendable, transparent thin-film transistors that use carbon-nanotube-based conductors and semiconductors with elastomeric dielectrics," *Adv. Mater.*, vol. 18, no. 3, pp. 304-309, 2006.
- [46] D. J. Lipomi and Z. Bao, "Stretchable, elastic materials and devices for solar energy conversion," *Energy Environ. Sci.*, vol. 4, no. 9, pp. 3314-3328, 2011.
- [47] S. P. Lacour, S. Wagner, Z. Y. Huang and Z. Suo, "Stretchable gold conductors on elastomeric substrates," *Appl. Phys. Lett.*, vol. 82, no. 15, pp. 2404-2406, 2003.
- [48] J. Jeong, S. Kim, J. Cho and Y. Hong, "Stable stretchable silver electrode directly deposited on wavy elastomeric substrate," *IEEE Electron Device Lett.*, vol.30, pp. 1284-1286, 2009.
- [49] V. Vijay, A. D. Rao and K. S. Narayan, "In situ studies of strain dependent transport properties of conducting polymers on elastomeric substrates," *J. Appl. Phys.*, vol. 109, p. 084525, 2011.
- [50] N. Bowden, S. Brittain, A. G. Evans, J. W. Hutchinson and G. M. Whitesides, "Spontaneous formation of ordered structures in thin films of metals supported on an elastomeric polymer," *Nature*, vol. 393, pp. 146-149, 1998.
- [51] S. H. Chae, W. J. Yu, J. J. Bae, D. L. Duong, D. Perello, H. Y. Jeong, Q. H. Ta, T. H. Ly, Q. A. Vu, M. Yun, X. Duan and Y. H. Lee, "Transferred wrinkled Al₂O₃ for highly stretchable and transparent graphene-carbon nanotube transistors," *Nat. Mater.*, vol. 12, no. 5, pp. 403-409, 2013.
- [52] K. Park, D.-K. Lee, B.-S. Kim, H. Jeon, N. E. Lee, D. Whang, H. J. Lee, Y. J. Kim and J.-H. Ahn, "Stretchable, transparent zinc oxide thin film transistors," *Adv. Func. Mater.*, vol. 20, no. 20, pp. 3577-3582, 2010.
- [53] S. P. Lacour, C. Tsay and S. Wagner, "An elastically stretchable TFT circuit," *IEEE Electron Device Lett.*, vol. 25, no. 12, pp. 792-794, 2004.
- [54] J. I. Lee, X. Huang and P. B. Chu, "Nanoprecision MEMS capacitive sensor for linear and rotational positioning," *J. of Microelectromech. Syst.*, vol. 18, no. 3, pp. 660-670, 2009.
- [55] V. Saxena, T. J. Plum, J. R. Jessing and R. J. Baker, "Design and fabrication of a MEMS capacitive chemical sensor system," *IEEE Workshop on Microelectron. and Electron Devices*, Boise, ID, 2006, pp. 17-18, 2006.
- [56] R. Puers, "Capacitive sensors: When and how to use them," *Sensors and Actuators, A*, vol. 37-38, pp. 93-105, 1993.

-
- [57] S. Sze, *Semiconductor Sensors*, John Wiley & Sons, Inc., New York, 1994.
- [58] S. Tez, U. Aykutlu, M. M. Torunbalci and T. Akin, "A Bulk-Micromachined Three-Axis Capacitive MEMS Accelerometer on a Single Die," *J. of Microelectromech. Syst.*, vol. 24, no. 5, pp. 1264-1274, 2015.
- [59] D. J. Lipomi, J. A. Lee, M. Vosgueritchian, B. C. K. Tee, J. A. Bolander and Z. Bao, "Electronic properties of transparent conductive films of pedot:pss on stretchable substrates," *Chem. Mater.*, vol. 24, no. 2, pp. 373-382, 2012.
- [60] N. Stuebler, J. Fritzsche and M. Klueppel, "Mechanical and electrical analysis of carbon black networking in elastomers under strain," *Polym. Eng. Sci.*, vol. 51, no. 6, pp. 1206-1217, 2011.
- [61] A. de la Vega, J. Sumfleth, H. Wittich and K. Schulte, "Time and temperature dependent piezoresistance of carbon nanofiller/polymer composites under dynamic load," *J. Mater. Sci.* vol. 47, no. 6, pp. 2648-2657, 2012.
- [62] I. E. Gonenli, "Failure assessment in aerospace systems via integrated multi-functional sensors", PhD Thesis, University of Texas at Arlington, USA, 2010.
- [63] G. M. A. Ashruf, "Thin flexible pressure sensors," *Sensor review*, vol. 22, no. 4, pp.322-327, 2002.
- [64] F. Sygulla, F. Ellensohn, A. Hildebrandt, D. Wahrmann and D. Rixen, "A flexible and low-cost tactile sensor for robotic applications," *IEEE Int. Conf. on Adv. Intell. Mechatron.*, Munich, Germany, pp. 58-63, 2017.
- [65] M. Johnsson and C. Balkenius, "Sense of touch in robots with self-organizing maps," *IEEE Trans. on Robot.*, vol. 27, no. 3, pp. 498-507, 2011.
- [66] R. S. Dahiya, M. Valle, G. Metta, and G. Sandini, "Tactile sensing—From human to humanoids," *IEEE Trans. on Robot.*, vol. 26, no. 1, pp. 1–20, 2010.
- [67] C. Bartolozzi, L. Natale, F. Nori and G. Metta, "Robots with a sense of touch," *Nature Materials*, vol. 15, pp. 921-925, 2016.
- [68] V. A. Ho, M. Makikawa and S. Hirai, "Flexible fabric Sensor toward a humanoid robot's skin: fabrication, characterization, and perceptions," *IEEE Sensors J.*, vol. 13, no. 10, pp. 4065-4080, 2013.
- [69] UN World Population Prospects, 2017 Revision.
- [70] A. Sato, Y. Funabora, S. Doki and K. Doki, "Contact force distribution predictive control system for wearable robot with tactile sensors," *Asian Control Conf.*, Gold Coast, Australia, pp. 1373-1378, 2017,

-
- [71] M. H. Rahman, M. Saad, J. P. Kenne and P. S. Archambault, "Robot-assisted rehabilitation for elbow and forearm movements," *Int. J. Biomechatron. Biomed. Robot.*, vol. 1, no. 4, p. 206218, 2011.
- [72] H. In, B. Kang, M. Sin and K. Cho, "A wearable robot for the hand with a soft tendon routing system," *IEEE Robot. and Autom. Mag.*, vol. 22, no. 1, 2015.
- [73] O. Chuy, Y. Hirata and K. Kosuge, "A new control approach for a robotic walking support system in adapting user characteristics," *IEEE Trans. Syst. Man Cybern. C Appl. Rev.*, vol. 36, no. 6, pp. 725-733, 2006.
- [74] S. Fukushima, H. Sekiguchi, Y. Saito, W. Iida, T. Nozaki and K. Ohnishi, "Artificial replacement of human sensation using haptic transplant technology," *IEEE Trans. on Ind. Electron.*, vol. 65, no. 5, pp. 3985-3994, 2018.
- [75] Z. Wu, C. Li, J. A. Hartings, R. Narayan and C. Ahn, "Polysilicon thin film developed on flexible polyimide for biomedical applications," *J. of Microelectromech. Syst.*, vol. 25, no. 4, pp. 585-592, 2016.
- [76] S. Kwon and J. park, "Kinesiology-based robot foot design for human-like walking," *Int. J. of Adv. Robot. Syst.*, vol. 9, p. 259, 2012.
- [77] J. Li, Q. Huang, W. Zhang, Z. Yu and K. Li, "Flexible foot design for a humanoid robot," *IEEE Int. Conf. on Autom. and Logistics*, pp. 1414-1419, 2008.
- [78] A. Damilano, P. M. Ros, A. Sanginario, A. Chiolerio, S. Bocchini, I. Roppolo, C. F. Pirri, S. Carrara, D. Demarchi and M. Crepaldi, "A robust capacitive digital read-out circuit for a scalable tactile skin," *IEEE Sensors J.*, vol. 17, no. 9, pp. 2682-2695, 2017.
- [79] H. Nakamoto, H. Ootaka, M. Tada, I. Hirata, F. Kobayashi and F. Kojima, "Stretchable strain sensor with anisotropy and application for joint angle measurement," *IEEE Sensors J.*, vol. 16, no. 10, pp. 3572-3579, 2016.
- [80] C. Tudor-Locke and D. R. Bassett, "How many steps/day are enough?," *Sports Med.*, vol. 34, no. 1, pp. 1-8, 2004.
- [81] C. Cummins, R. Orr, H. O'Connor and C. West "Global positioning systems (GPS) and microtechnology sensors in team sports: a systematic review," *Sports Med.*, vol. 43, no. 10., pp. 1025-1042, 2013.
- [82] P. S. Freedson and K. Miller, "Objective monitoring of physical activity using motion sensors and heart rate," *Research Quart. for Exercise and Sport*, vol. 71, no. 2, pp. 21-29, 2015.

-
- [83] H. Ghasemzadeh, V. Loseu, E. Guenterberg and R. Jafari, "Sport training using body sensor networks: a statistical approach to measure wrist rotation for golf swing," *Int. Conf. on Body Area Net.*, Los Angeles, 2009.
- [84] M. R. Endsley, "Autonomous Driving Systems: A Preliminary Naturalistic Study of the Tesla Model S," *J. of Cognitive Eng. and Decision Making*, vol. 11, no. 3, pp. 225-238, 2017.
- [85] R. Matsuzaki and A. Todoroki, "Wireless flexible capacitive sensor based on ultra-flexible epoxy resin for strain measurement of automobile tires," *Sensors and Actuators A*, vol. 140, no. 1, pp. 32-42, 2007.
- [86] J. Hu, "Overview of Flexible Electronics from ITRI's Viewpoint," *IEEE VLSI Test Symp.*, p. 84, 2010.
- [87] IHS Markit, "Wearable Sensor Market to Expand Sevenfold in Five Years", Internet: <http://press.ihs.com/press-release/technology/wearable-sensor-market-expand-sevenfold-five-years>, Oct 16, 2014 [Accessed on Mar 5, 2018].
- [88] H. H. Asada, Hong-Hui Jiang and P. Gibbs, "Active noise cancellation using MEMS accelerometers for motion-tolerant wearable bio-sensors," *Annual Int. Conf. of the IEEE Eng. in Med. and Bio. Society*, San Francisco, CA, pp. 2157-2160, 2004.
- [89] S. Yun, S. Park, B. Park, S. K. Park, H. Prahlad, P. V. Guggenberg and K. U. Kyung, "Polymer-Based Flexible Visuo-Haptic Display," *IEEE Trans. on Mechatron.*, vol. 19, no. 4, pp. 1463-1469, 2014.
- [90] L. Menon, H. Yang, S. J. Cho, S. Mikael, Z. Ma and W. Zhou, "Transferred Flexible Three-Color Silicon Membrane Photodetector Arrays," *IEEE Photon. J.*, vol. 7, no. 1, pp. 1-6, 2015.
- [91] J. T. Smith, E. Bawolek, J. Trujillo, G. Raupp, D. R. Allee and J. B. Christen, "Adapting large-area flexible hybrid TFT/CMOS electronics and display technology to create an optical sensor array architecture," *IEEE Int. Symp. on Circuits and Syst.*, Baltimore, MD, pp. 1-4, 2017.
- [92] L. M. Goncalves, J. G. Rocha and S. Lanceros-Mendez, "Flexible X-Ray Detector Based on the Seebeck Effect," *IEEE Int. Sym. on Ind. Electron.*, Vigo, pp. 1525-1529, 2007.
- [93] M. Marengo, G. Marinaro and J. Kosel, "Flexible temperature and flow sensor from laser-induced graphene," *IEEE Sensors Conf.*, Glasgow, pp. 1-3, 2017.
- [94] Z. D. Lin, S. J. Young and S. J. Chang, "Carbon Nanotube Thin Films Functionalized via Loading of Au Nanoclusters for Flexible Gas Sensors Devices," *IEEE Trans. on Electron Dev.*, vol. 63, no. 1, pp. 476-480, 2016.

-
- [95] B. Y. Majlis, K. Sooriakumar, S. Najdu, and B. Patmon, "Use of micro-machined accelerometer in today's world", *IEEE Conf. Semicon. Electron.*, pp. 9-14, 2002.
- [96] J. Bernstein, "An overview of mems inertial sensing technology", *Sensors Online*, Feb 2003.
- [97] A. Albarbar, A. Badri, J. K. Sinha and A. Starr, "Performance evaluation of MEMS accelerometers", *Measurement*, vol. 42, pp. 790-795, 2009.
- [98] M. S. Mahmood, Z. Celik-Butler and D. P. Butler, "Design and fabrication of self-packaged, flexible MEMS accelerometer," *IEEE Sensors Conf.*, Busan, pp. 2-4, 2015.
- [99] F. A. Levinzon, "Ultra-low-noise seismic piezoelectric accelerometer with integral FET amplifier", *IEEE Sensors J.*, vol. 12, no. 6, pp. 2262-2268, 2012.
- [100] Y. Li, Q. Zheng, Y. Hu and Y. Xu, "Micromachined piezoresistive accelerometers based on an asymmetrically gapped cantilever", *J. of Microelectromech. Syst.*, vol. 20, no. 1, pp. 83-94, 2011.
- [101] H. Tavakkoli, H. G. Momen, E. A. Sani and M. Yazgi, "An inductive MEMS accelerometer," *Int. Conf. on Elect. and Electron. Eng.*, Turkey, pp. 459-463, 2017,
- [102] S. Aoyagi, S. Kumagai, D. Yoshikawa and Y. Isono, "Surface micromachined accelerometer using ferroelectric substrate", *Sensors and Actuators A*, vol. 139, pp. 88-94, 2007.
- [103] P. F. d. C. Antunes, H. F. T. Lima, N. J. Alberto, H. Rodrigues, P. M. F. Pinto, J. d. L. Pinto, R. N. Nogueira, H. Varum, A. G. Costa and P. S. d. B. Andre, "Optical fiber accelerometer system for structural dynamic monitoring", *IEEE Sensors J.*, vol. 9, no. 11, pp. 1347-1354, 2009.
- [104] C. H. Liu and T. W. Kenny, "A high-precision, wide-bandwidth micromachined tunneling accelerometer," *J. of Microelectromech. Syst.*, vol. 10, no. 3, pp. 425-433, 2001.
- [105] K. Sanyal and K. Biswas, "Structural design and optimization of MEMS based capacitive accelerometer", *Dev. for Integr. Circuit*, Kalyani, pp. 294-298, 2017.
- [106] J. Bernstein, R. Miller, W. Kelley and P. Ward, "Low noise MEMS vibration sensor for geophysical applications", *J. of microelectromech. Syst.*, vol.8, no. 4, pp 433-438, 1999.
- [107] B. E. Boser and R. T. Howe, "Surface Micromachined Accelerometers", *IEEE J. of Solid State Circuits*, vol. 31, no. 3, pp. 366-375, 1996.
- [108] W. Wai-Chi, A. A. Azid, and B. Y. Majlis, "Formulation of stiffness constant and effective mass for a folded beam," *Archives of Mechanics*, vol. 62, pp. 405-418, 2010.

-
- [109] Chae, H. Kulah and K. Najafi, "A hybrid Silicon-On-Glass (SOG) lateral micro-accelerometer with CMOS readout circuitry", *IEEE Int. Conf. on Microelectromech. Syst.*, pp. 623-626, 2002.
- [110] S.Kal, S.Das, D. K. Maurya, K. Biswas, A.R. Sankar and S. K. Lahiri, "CMOS compatible bulk micromachined silicon piezoresistive accelerometer with low off-axis sensitivity," *Microelectron. J.*, vol. 37, no. 1, pp. 22-30, 2006.
- [111] M. Bao, *Analysis and Design Principles of MEMS Devices*, Elsevier, 2005
- [112] S. K. Vemuri, "Behavioral Damping of Viscous Damping in MEMS", M.S. Thesis, Carnegie Mellon University, 2000.
- [113] J. J. Blech, "On isothermal squeeze films," *J. of Lubrication Tech.*, vol. 105, no. 4, pp.615-620, 1983.
- [114] W. A. Gross, *Fluid Film Lubrication*, New York, Wiley, 1980.
- [115] T. Veijola, H. Kuisma, J. Lahdenpera and T. Ryhanen, "Equivalent-circuit model of the squeezed gas film in a silicon accelerometer," *Sensors Actuators A*, vol. 48, pp.239-248, 1995.
- [116] S. Fukui and R. Kaneko, "Analysis of ultra-thin gas film lubrication based on linearized Boltzmann equation: first report-derivation of a generalized lubrication equation including thermal creep flow," *J. Tribol.*, vol. 110, no. 2, pp.253-262, 1988.
- [117] R. A. Dias and L. A. Rocha, "Improving capacitance/damping ratio in a capacitive MEMS transducer", *J. of Micromech. and Microeng.*, vol.24, 015008, 2013.
- [118] W. E. Langlois, "Isothermal squeeze films," *Quarterly of Appl. Mathematics*, vol. 20, no. 2, pp. 131-150, 1962.
- [119] T. Veijola, A. Pursula and P. Raback P, "Extending the validity of squeezed-film damper models with elongations of surface dimensions," *J. Micromech. Microeng.*, vol. 15, pp.1624-1636, 2005.
- [120] P. Zwahlen, A. M. Nguyen, Y. Dong, F. Rudolf, M. Pastre and H. Schmid, "Navigation grade MEMS accelerometer," *IEEE Int. Conf. on Microelectromech. Syst.*, Hong Kong, pp. 631-634, 2010.
- [121] C. M. Sun, M. H. Tsai, Y. C. Liu and W. Fang, "Implementation of a monolithic single proof-mass tri-axis accelerometer using CMOS-MEMS technique," *IEEE Trans. on Electron Devices*, vol. 57, no. 7, pp. 1670-1679, 2010.

-
- [122] H. H. Asada, Hong-Hui Jiang and P. Gibbs, "Active noise cancellation using MEMS accelerometers for motion-tolerant wearable bio-sensors," *26th Annual Int. Conf. of the IEEE Eng. in Med. and Biol. Society*, San Francisco, CA, pp. 2157-2160, 2004.
- [123] J. Chen, K. Kwong, D. Chang, J. Luk and R. Bajcsy, "Wearable sensors for reliable fall Detection," *IEEE Eng. in Med. Biol., Annual Conf.*, Shanghai, 2005, pp. 3551-3554, 2005.
- [124] M. S. Mahmood, Z. Celik-Butler and D. P. Butler, "Design, fabrication and characterization of flexible MEMS accelerometer using multi-Level UV-LIGA," *Sensors and Actuators A: Physical*, vol. 263, no. 15, pp. 530-541, 2017.
- [125] B.V. Amini and F. Ayazi, "Micro-cavity capacitive silicon-on-insulator accelerometers", *J. of Micromech. and Microeng.*, vol. 15, pp. 2113–2120, 2005.
- [126] R.A. Dias, F.S. Alves, M. Costa, H. Fonseca, J. Cabral, J. Gaspar and L.A. Rocha, "Real-time operation and characterization of high-performance time-based accelerometer", *J. of Microelectromech. Syst.*, vol. 24, no. 6, pp. 1703–1711, 2015.
- [127] P. Monajemi and F. Ayazi, "Design optimization and implementation of a microgravity capacitive HAROSS accelerometer", *IEEE Sensors J.*, vol. 6, no. 1, pp.39–46, 2006.
- [128] O. Aydin and T. Akin, "A bulk-micromachined fully differential MEMS accelerometer with split interdigitated fingers", *IEEE Sensors J.* vol. 13, no. 8, pp. 2914–2921, 2013.
- [129] M. Despont, N. Lorenz, J. Fahrni, P. Brugger and P. Vettiger, "High-aspect ratio, ultra-thick, negative-tone near-uv photoresist for MEMS applications," *IEEE Annual Int. Workshop on Microelectromech. Syst.*, pp. 518–522, 1997.
- [130] İ. E. Gonenli, Z. Celik-Butler and D. P. Butler, "Surface micromachined MEMS accelerometers on flexible polyimide substrate," *IEEE Sensors J.*, vol. 11, no. 10, pp. 2318 -2326, 2011
- [131] Y. Konaka and M. G. Allen, "Single- and multi-layer electroplated microaccelerometers," *Int. Workshop on Microelectromech. Syst.*, San Diego, CA, pp. 168-173, 1996.
- [132] D. Yamane, T. Matsushima, T. Konishi, H. Toshiyoshi, K. Machida and K. Masu, "A dual-axis MEMS inertial sensor using multi-layered high-density metal for an arrayed CMOS-MEMS accelerometer," *Symp. on Design, Test, Integr. and Packag. of MEMS/MOEMS*, Cannes, pp. 1-4, 2014.

-
- [133] G. A. Cohen, F. G. Tseng Zhang, U. Frodis and F. Mansfeld, "EFAB: rapid, low-cost desktop micromachining of high aspect ratio true 3-D MEMS", *IEEE Int. Conf. on Micro Electro Mechanical Syst.*, pp. 244-251, 1999.
- [134] EFAB, Instant Masking and Instant Mask are trademarks of MEMGen Corp, now Microfabrica Inc.
- [135] P. B. Zantye, Processing, Reliability and Integration Issues in Chemical Mechanical Planarization, Ph.D. Dissertation, Dept. Mech. Eng., University of South Florida, FL, 2005.
- [136] W. T. Park, R. N. Candler, V. Ayanoor-Vitikkate, M. Lutz, A. Partridge, G. Yama and T. W. Kenny, "Fully encapsulated sub-millimeter accelerometers," *IEEE Int. Conf. on Microelectromech. Syst.*, pp. 347-350, 2005.
- [137] J. C. Souriau, L. Castagné, G. Parat, G. Simon, K. Amara, P. D'hiver and R. D. Molin, "Implantable device including a MEMS accelerometer and an ASIC chip encapsulated in a hermetic silicon box for measurement of cardiac physiological parameter," *IEEE Electronic Compon. and Technol. Conf.*, pp. 1198-1203, 2014.
- [138] G. Wu, D. Xu, B. Xiong, Y. Wang, Y. Wang and Y. Ma, "Wafer-level vacuum packaging for MEMS resonators using glass frit bonding," *J. of Microelectromech. Syst.*, vol. 21, no. 6, pp. 1484-1491, Dec. 2012.
- [139] W. Christiaens, T. Loehner, B. Pahl, M. Feil, B. Vandeveldel and J. Vanfleteren, "Embedding and assembly of ultrathin chips in multilayer flex boards," *Circuit World*, vol. 34, no. 3, pp. 3-8, 2008.
- [140] L. Wang, T. Sterken, M. Cauwe, D. Cuypers and J. Vanfleteren, "Fabrication and characterization of flexible ultrathin chip package using photosensitive polyimide," *IEEE Trans. on Compon., Packag. and Manuf. Technol.*, vol. 2, no. 7, pp. 1099-1106, July 2012.
- [141] W. Christiaens, E. Bosman and J. Vanfleteren, "UTCP: A novel polyimide-based ultra-thin chip packaging technology," *IEEE Trans. on Compon. and Packag. Technol.*, vol. 33, no. 4, pp. 754-760, Dec. 2010.
- [142] M. S. Rahman, M. M. Chitteboyina, D. P. Butler, Z. Celik-Butler, S. P. Pacheco and R. V. McBean, "Device-level vacuum packaging for RF MEMS," *J. of Microelectromech. Syst.*, vol. 19, no. 4, pp. 911-918, Aug. 2010.
- [143] C. P. Hsu, M. C. Yip and W. Fang, "Implementation of a gap-closing differential capacitive sensing Z-axis accelerometer on an SOI wafer", *J. Micromech. Microeng.*, vol. 19, p. 075006, 2009.
- [144] G. Langfelfer, A. Caspani, A. Tocchio, S. Zerbin and A. Longoni, "High-sensitivity differential fringe-field MEMS accelerometers", *Int. Conf on Solid-State Sensors, Actuators and Microsyst.*, pp. 1823-1826, 2013.

-
- [145] S. Katzir, "The Discovery of the Piezoelectric Effect," *Arch. Hist. Exact Sci.*, vol. 57, pp. 61–91, 2003.
- [146] T. Kim, J. Kim, R. Dalmau, R. Schlessler, E. Preble and X. Jiang, "High-temperature electromechanical characterization of AlN single crystals," *IEEE Trans. on Ultrason., Ferroelec., and Freq. Control*, vol. 62, no. 10, pp. 1880-1887, 2015.
- [147] J. Holterman and P. Groen, "An introduction to piezoelectric materials and applications," 1st Ed., Apeldoorn The Netherlands, 2013.
- [148] Q. Xu, "Continuous integral terminal third-order sliding mode motion control for piezoelectric nanopositioning system," *IEEE/ASME Trans. on Mechatron.*, vol. 22, no. 4, pp. 1828-1838, 2017.
- [149] J. Fialka and P. Beneš, "Comparison of methods of piezoelectric coefficient measurement," *IEEE Int. Instrum. and Meas. Technol. Conf.*, Graz, pp. 37-42, 2012.
- [150] H. F. Tiersten, "Linear piezoelectric plate vibrations," New York, Plenum Press, 1969.
- [151] Piezoelectric Ceramics: Principles and Applications, APC International Ltd., 2011.
- [152] Y. Kusano, Q. Wang, R. Q. Rudy, R. G. Polcawich and D. A. Horsley, "Wideband air-coupled PZT piezoelectric micromachined ultrasonic transducer through DC bias tuning," *IEEE Int. Conf. on Microelectromech. Syst.*, Las Vegas, NV, 2017, pp. 1204-1207.
- [153] P. Norgard and S. D. Kovalski, "A Lithium Niobate Piezoelectric Transformer Resonant High-Voltage Power Source," *IEEE Trans. on Plasma Sci.*, vol. 44, no. 5, pp. 808-815, 2016.
- [154] C. Oshman, C. Opoku, A. S. Dahiya, D. Alquier, N. Camara and G. Poulin-Vittrant, "Measurement of Spurious Voltages in ZnO Piezoelectric Nanogenerators," *J. of Microelectromech. Syst.*, vol. 25, no. 3, pp. 533-541, 2016.
- [155] R. J. Przybyla, S. E. Shelton, A. Guedes, I. I. Izyumin, M. H. Kline, D. A. Horsley and B. E. Boser, "In-Air Ranging With an AlN Piezoelectric Micromachined Ultrasound Transducer," *IEEE Sensors J.*, vol. 11, no. 11, pp. 2690-2697, Nov. 2011.
- [156] M. Benetti, D. Cannata, F. Di Pictrantonio and E. Verona, "Growth of AlN piezoelectric film on diamond for high-frequency surface acoustic wave devices," *IEEE Trans. on Ultrason., Ferroelect., and Freq. Control*, vol. 52, no. 10, pp. 1806-1811, 2005.

-
- [157] M. Akiyama T. Kamohara, K. Kano, A. Teshigahara, Y. Takeuchi and N. Kawahara, “Enhancement of piezoelectric response in scandium aluminum nitride alloy thin films prepared by dual reactive cosputtering”, *Adv. Mater.*, vol. 21, pp. 593–596, 2009.
- [158] Registration, evaluation, authorization and restriction of chemicals (REACH) as regards Lead and its compounds, Commission Regulation (EU), 2015.
- [159] C. Hong, H. Kim, B. Choi, H. Han, J. S. Son, C. W. Ahn and W. Jo, “Lead-free piezoceramics – Where to move on?”, *J. of Materiomics*, vol. 2, no. 1, pp. 1-24, 2016.
- [160] D. Nishijima, T. Tabaru and M. Akiyama, “Cracking of aluminium nitride film on stainless steel substrate at elevated temperature”, *Material Science Forum*, vol. 561-565, pp. 1221-1224, 2007.
- [161] S. Zhang and F. Yu, “Piezoelectric materials for high temperature sensors”, *J. of Amer. Ceram. Soc.*, vol. 94, no. 10, pp 3153–3170, 2011.
- [162] S. Zhang, Y. Fei, B. H. T. Chai, E. Frantz, D. W. Snyder, X. Jiang and T. R. Shrout, “Characterization of piezoelectric single crystal $\text{YCa}_4\text{O}(\text{BO}_3)_3$ for high temperature applications,” *Appl. Phys. Lett.*, vol. 92, p. 202905, 2008.
- [163] K. Kim, S. Zhang, G. Salazar, and X. Jiang, “Design, fabrication and characterization of high temperature piezoelectric vibration sensor using YCOB crystals,” *Sensors & Actuators A Phys.*, vol. 178, pp. 40–48, 2012.
- [164] Y. Hu, B. D. B. Klein, Y. Su, S. Niu, Y. Liu, and Z. L. Wang, “Temperature dependence of the piezotronic effect in ZnO nanowires,” *Nano Letters*, vol. 13, no. 11, pp. 5026-5032, 2013.
- [165] W. Zhou and B. Chu, “Strong electromechanical response in lead zirconate titanate metamaterials” *J. of Amer. Ceram. Soc.*, vol. 99, no, 10, pp.3317-3324, 2016.
- [166] P. M. Martin, M. S. Good, J. W. Johnston, G. J. Posakony, L. J. Bond and S. L. Crawford, “Piezoelectric films for 100-MHz ultrasonic transducers”, *Thin Solid Films*, vol. 379, pp. 253-258, 2000.
- [167] S. Tadigadapa and K. Mateti, “Piezoelectric MEMS sensors: state-of-the-art and perspectives,” *Meas. Sci. Technol.*, vol. 20, pp. 1-30, 2009.
- [168] R. Hou, D. Hutson and K. J. Kirk, “Development of sputtered AlN thin film ultrasonic transducers for durable high temperature applications,” *Insight - Non-Destructive Testing and Condition Monitoring*, vol. 55, no. 6, pp. 302-307, 2013.

-
- [169] M. H. S. Alrashdan, A. A. Hamzah, B. Y. Majlis and M. F. Aziz, "Aluminum nitride thin film deposition using DC sputtering," 2014 IEEE International Conference on Semiconductor Electronics (ICSE2014), Kuala Lumpur, pp. 72-75, 2014.
- [170] M. Dwivedi, J. Bhargava, A. Sharma, V. Vyas and G. Eranna, "CO Sensor Using ZnO Thin Film Derived by RF Magnetron Sputtering Technique," *IEEE Sensors J.*, vol. 14, no. 5, pp. 1577-1582, 2014.
- [171] D. Nakahira, T. Kanda, K. Suzumori, M. Kabuto, Y. Michihiro and M. Ueno, "Hydrothermal deposition of the PZT film and applications of piezoelectric actuators," *Int. Conf. on Mechatron. and Machine Vision in Practice*, pp. 501-506. Auckland, 2012.
- [172] D. A. Stubbs and R. E. Dutton, "An ultrasonic sensor for high-temperature materials processing," *JOM*, vol. 48, no. 9, pp 29-31, 1996.
- [173] E. Ruiz, S. Alvarez, and P. Alemany, "Electronic structure and properties of AlN," *Phys. Rev. B Condens. Matter*, vol. 49, no. 11, pp. 7115–7123, 1994.
- [174] D. A. Parks, B. R. Tittmann, and M. M. Kropf, "Aluminum nitride as a high temperature transducer," *AIP Conf. Proc.*, vol. 1211, pp. 1029–1034, 2010.
- [175] A. Sotnikov, H. Schmidt, M. Weihnacht, E. Smirnova, T. Chemekova, and Y. Makarov, "Elastic and piezoelectric properties of AlN and LiAlO₂ single crystals," *IEEE Trans. Ultrason. Ferroelectr. Freq. Control*, vol. 57, no. 4, pp. 808–811, 2010.
- [176] Q. Guo and A. Yoshida, "Temperature dependence of band gap change in InN and AlN," *Jpn. J. Appl. Phys.*, vol. 33, pp. 2453-2456, 1994.
- [177] V. Srikant and D. R. Clarke, "On the optical band gap of zinc oxide," *J. of Appl. Phys.*, vol. 83, p. 5447, 1998.
- [178] S. Trolier-Mckinstry and P. Muralt, "Thin Film Piezoelectrics for MEMS", *J. of Electroceram.*, vol 12, pp. 7–17, 2004.
- [179] R. Ruby, P. Bradley, J. D. Larson, and Y. Oshmyansky, "PCS 1900 MHz duplexer using thin film bulk acoustic resonators (FBARs)," *Electron. Lett.*, vol. 35, no. 10, pp. 794–795, 1999.
- [180] R. Aigner, J. Kaitila, J. Ella, L. Elbrecht, W. Nessler, M. Handtmann, T. R. Herzog and S. Marksteiner., "Bulk-acoustic-wave filters: performance optimization and volume manufacturing," *IEEE Int. Micro. Symp. Digest*, vol. 3, pp. 2001–2004, 2003.

-
- [181] Y. Lu, H. Tang, S. Fung¹, Q. Wang, J. M. Tsai, M. Daneman, B. E. Boser, and D. A. Horsley, "Ultrasonic fingerprint sensor using a piezoelectric micromachined ultrasonic transducer array integrated with complementary metal oxide semiconductor electronics," *Appl. Phys. Lett.*, vol. 106, no. 26, p. 263503, 2015.
- [182] J. Segovia-Fernandez, S. Sonmezoglu, S. T. Block, Y. Kusano, J. M. Tsai, R. Amirtharajah and D. A. Horsley., "Monolithic piezoelectric Aluminum Nitride MEMS-CMOS microphone," *Int. Conf. on Solid-State Sensors, Actuators and Microsyst.*, Kaohsiung, pp. 414-417, 2017,
- [183] L. Van Minh and H. Kuwano, "Highly efficient piezoelectric micro-energy harvesters with AlN thin films grown directly on flexible Ti foils," *Int. Conf. on Microelectromech. Syst.*, pp. 833-836, Las Vegas, NV, 2017.
- [184] R. Matloub, M. Hadad, A. Mazzalai, N. Chidambaram, G. Moulard, C. S. Sandu, T. Metzger, and P. Mural^t., "Piezoelectric Al_{1-x}Sc_xN thin films: A semiconductor compatible solution for mechanical energy harvesting and sensors," *Appl. Phys. Lett.*, vol. 102, no. 15, p. 152903, 2013.
- [185] M. Moreira, J. Bjurström, I. Katardjev, and V. Yantchev, "Aluminum scandium nitride thin-film bulk acoustic resonators for wide band applications," *Vacuum*, vol. 86, no. 1, pp. 23–26, 2011.
- [186] P. W. Barth and J. B. Angell, "Flexible Circuit and Sensor Arrays Fabricated by Monolithic Silicon Technology", *IEEE Trans. on Electron Dev.*, vol. 32, no. 7, pp. 1202-1205, 1985.
- [187] F. Jiang, G. Lee, Y. Tai, and C. Ho, "A flexible micromachine-based shear-stress sensor array and its application to separation-point detection", *Sensors and Actuators*, vol. 79, pp. 194–203, 2000.
- [188] D. H. Kim, J. Ahn, W. M. Choi, H. Kim, T. Kim, J. Song, Y. Y. Huang, Z. Liu, C. Lu, and J. A. Rogers, "Stretchable and Foldable Silicon Integrated Circuits", *Science*, vol. 320, pp. 507-511, 2008.
- [189] Q. Cao, H. Kim, N. Pimparkar, J. P. Kulkarni, C. Wang, M. Shim, K. Roy, M. A. Alam, and J. A. Rogers, "Medium-scale carbon nanotube thin-film integrated circuits on flexible plastic substrates", *Nature*, vol. 454, pp. 495-500, 2008.
- [190] H. Kim and K. Najafi, "Characterization of Aligned Wafer-Level Transfer of Thin and Flexible Parylene Membranes", *J. of Microelectromech. Syst.*, vol. 16, no. 6, pp. 1386-1396, 2007.
- [191] A. C. Siegel, S. T. Phillips, M. D. Dickey, N. Lu, Z. Suo, and G. M. Whitesides, "Foldable Printed Circuit Boards on Paper Substrates", *Adv. Functional Mater.*, vol. 20, pp. 28-35, 2010.

-
- [192] V. Mulloni, F. Giacomozzi and B. Margesin, "Controlling stress and stress gradient during the release process in gold suspended micro-structures," *Sensors and Actuators A*, vol. 162, pp. 93–99, 2010.
- [193] M. L. Hammock, A. Chortos, B. C. K. Tee, J. B. H. Tok, and Z. Bao, "25th anniversary article: the evolution of electronic skin (e-skin): a brief history, design considerations, and recent progress," *Adv. Mater.*, vol. 25, pp. 5997-6038, 2013.
- [194] A.Liu, M, Guo, J. Gao and M. Zhao, "Influence of bond coat on shear adhesion strength of erosion and thermal resistant coating for carbon fiber reinforced thermosetting polyimide," *Surface and Coatings Technology*, vol. 201, no. 6, 2006, pp. 2696-2700, 2006.
- [195] J. A. Forrest, K. Dalnoki-Veress, J. R. Stevens and J. R. Dutcher, "Effect of Free Surfaces on the Glass Transition Temperature of Thin Polymer Films," *Phys Rev Lett.*, vol. 77, no. 10, pp. 2002-2005, 1996.
- [196] T. S. Chow, "Molecular Interpretation of the Glass Transition Temperature of Polymer-Diluent Systems," *Macromolecules*, vol. 13, no. 2, pp. 362–364, 1980.
- [197] J. L. Keddie, R. A. L. Jones and R. A. Cory, "Size-Dependent Depression of the Glass Transition Temperature in Polymer Films," *Europhys. Lett.*, vol. 27, no. 1, pp. 59-64, 1994.
- [198] J. L. Keddie, R. A. L. Jones and R. A. Cory, "Interface and surface effects on the glass-transition temperature in thin polymer films," *Faraday Discussions*, vol. 98, pp. 219-230, 1994.
- [199] M. Ahmed, M. M. Chitteboyina, D. Butler, and Z. Celik-Butler, "Temperature Sensor in a Flexible Substrate", *IEEE Sensors J.*, vol. 12, no. 5, pp. 864-869, 2012.
- [200] PI5878G product bulletin, HD Microsystems (2009).
- [201] PI2600 series product bulletin, HD Microsystems (2009).
- [202] H. S. Shin, Y. M. Jung, T. Y. Oh, T. Chang, S. B. Kim, D. H. Lee, and I. Noda, "Glass Transition Temperature and Conformational Changes of Poly(methyl methacrylate) Thin Films Determined by a Two-Dimensional Map Representation of Temperature-Dependent Reflection- Absorption FTIR Spectra", *Langmuir*, vol. 18, pp. 5953-5958, 2002.
- [203] B. Yang, W.M. Huang, C. Li, L. Li, and J.H. Chor, "Qualitative separation of the effects of carbon nano-powder and moisture on the glass transition temperature of polyurethane shape memory polymer", *Scripta Materialia*, vol. 53, pp. 105-107, 2005.

-
- [204] H. Noh, Y. Huang, and P. J. Hesketh, "Parylene micromolding, a rapid and low-cost fabrication method for parylene microchannel", *Sensors and Actuators B*, 102, pp. 78-85, 2004.
- [205] Kapton HN polyimide film product specifications, Dupont (2016).
- [206] G. Wu, Y.Cheng, Z. Wang, K. Wang and A. Feng, "In situ polymerization of modified graphene/polyimide composite with improved mechanical and thermal properties," *J. of Mater. Sci.: Mater. in Electron.*, vol. 28, no. 1, pp. 576–581, 2017.
- [207] S. Mallakpour and M. Dinari, "Fabrication of polyimide/titania nanocomposites containing benzimidazole side groups via sol-gel process," *Prog. Org. Coat.*, vol. 75, pp. 373-378, 2012.
- [208] M. H. Tsai, H. Y. Wang, H. T. Lu, I. H. Tseng, H. H. Lu, S. L. Huang and J. M. Yeh, "Properties of polyimide/Al₂O₃ and Si₃N₄ deposited thin films," *Thin Solid Films*, vol. 519, no. 15, pp. 4969-4973, 2011.
- [209] I. H. Tseng, Y. F. Liao, J. C. Chiang and M. H. Chiang, "Transparent polyimide/graphene oxide nanocomposite with improved moisture barrier property," *Mater. Chem. Phys.*, vol. 136, no.1, pp. 247-253, 2012,
- [210] T. L. Li and S. L. C. Hsu, "Enhanced Thermal Conductivity of Polyimide Films via a Hybrid of Micro- and Nano-Sized Boron Nitride," *J. Phys. Chem. B*, vol. 114, no. 20, pp. 6825-6829, 2010.
- [211] S. Mallakpour and M. Dinari, "Polymer/organosilica nanocomposites based on polyimide with benzimidazole linkages and reactive organoclay containing isoleucine amino acid: Synthesis, characterization and morphology properties," *Mater. Res. Bull.*, vol. 47, no. 9, pp. 2336-2343, 2012.
- [212] B. Z.Jang, "Control of interfacial adhesion in continuous carbon and Kevlar fiber reinforced polymer composites," *Composites Sci. Technol.*, vol. 44, no. 4, pp. 333-349, 1992.
- [213] M. Hasegawa, Y. Watanabe, S. Tsukuda and J. Ishii, "Solution-processable colorless polyimides with ultralow coefficients of thermal expansion for optoelectronic applications," *Polym. Int*, vol. 65, pp. 1063–1073, 2016.
- [214] M. Ahmed and D. Butler, "Flexible substrate and release layer for flexible MEMS devices", *J. of Vacuum Sci. Technol. B*, vol. 31, no. 5, p. 050602, 2013.
- [215] HD-4100 series product bulletin, HD Microsystems (2009).

-
- [216] W. He, P. Goudeau, E. R. Bourhis, P. Renault and J. C. Dupre, "Study on Young's modulus of thin films on Kapton by microtensile testing combined with dual DIC system", *Surface and Coatings Technol.*, vol. 308, pp. 273–279, 2016.
- [217] K. Battes, C. Day, and V. Hauer, "Outgassing behavior of different high-temperature resistant polymers," *J. Vac. Sci. Technol. A*, vol. 36, no. 2, p. 021602, 2018.
- [218] A. Murari and A. Barzon, "Ultra high vacuum properties of some engineering polymers," *IEEE Trans. on Dielectr. and Electr. Insul.*, vol. 11, no. 4, pp. 613-619, 2004.
- [219] X. Guo, X. Liu, J. Luo, Z. Gan, Z. Meng and N. Zhang, "Silver nanowire/polyimide composite transparent electrodes for reliable flexible polymer solar cells operating at high and ultra-low temperature," *RSC Adv.*, vol. 5, pp. 24953-24959, 2015.
- [220] W. Dai, J. Yu, Z. Liu Y. Wang, Y. Song, J. Lyu, H. Bai, K. Nishimura, N. Jiang, "Enhanced thermal conductivity and retained electrical insulation for polyimide composites with SiC nanowires grown on graphene hybrid fillers," *Composites Part A: Appl. Sci. and Manuf.*, vol. 76, pp. 73-81, 2015.
- [221] J. Yu, X. Huang, L. Wang, P. Peng, C. Wu, X. Wua and P. Jiang, "Preparation of hyperbranched aromatic polyamide grafted nanoparticles for thermal properties reinforcement of epoxy composites," *Polym. Chem.*, vol. 2, no. 6, pp. 1380–1388, 2011.
- [222] Z. Yuan, J. Yu, B. Rao, H. Bai, N. Jiang, J. Gao and S. Lu, "Enhanced thermal properties of epoxy composites by using hyperbranched aromatic polyamide grafted silicon carbide whiskers," *Macromol. Res.*, vol. 22, no. 4, pp.405-411, 2014.
- [223] C. P. Wong and R. S. Bollampally, "Thermal conductivity, elastic modulus, and coefficient of thermal expansion of polymer composites filled with ceramic particles for electronic packaging," *J. Appl. Polym. Sci.*, vol. 74, no. 14, pp. 3396–403, 1999.
- [224] Y. Xu, D. Chung and C. Mroz, "Thermally conducting aluminum nitride polymermatrix composites," *Composites Part A: Appl. Sci. Manuf.*, vol.32, no.12, pp. 1749–1757, 2001.
- [225] T. Paulmier, B. Dirassen, M. Arnaout, D. Payan and N. Balcon, "Radiation induced conductivity of space used polymers under high energy electron irradiation," *Spacecraft Charging Technol. Conf.*, Pasadena, United States., Jun 2014,

-
- [226] H. Kim and K. Najafi, "Characterization of Aligned Wafer-Level Transfer of Thin and Flexible Parylene Membranes", *J. of Microelectromech. Syst.*, vol. 16, no. 6, pp. 1386-1396, 2007.
- [227] H. Bae, S. Arimoto, M. Yoshida and R. Ozawa, "Generation of fingering motions by robotic fingers using morphological characteristics of human thumb," *IEEE/RSJ Int. Conf. on Intell. Robots and Syst.*, pp. 1677-168, 2005.
- [228] D. Mallick, A. Amann and S. Roy, "Analysis of nonlinear spring arm for improved performance of vibrational energy harvesting devices," *J. of Physics*, 476 (2013).
- [229] A. Takada, S. Nakamura, Y. Yamanishi, S. Hashimura, S. Nagasawa, T. Kogure and S. Maeda, "Design of electrostatic adhesion device using the flexible electrodes", *Int. Symp. on Micro-NanoMechatronics and Human Sci.*, pp. 1-4, 2014.
- [230] L. Wang, "Investigation of the mechanical behavior of freestanding polycrystalline Au films deposited by evaporation and sputtering methods, PhD thesis," Auburn University, Auburn, Alabama, USA (2007).
- [231] W. N. Sharpe Jr. and A. McAleavey, "Tensile properties of LIGA Ni," *SPIE Conf. on Mater. and Dev. Character. in Micromachining*, vol. 3512. pp. 130-137, 1998.
- [232] T. Fritz, H. S. Cho, K. J. Hemker, W. Mokwa and U. Schnakenberg, "Characterization of electroplated Ni," *Microsyst. Technol.*, vol. 9, pp. 87-91, 2002.
- [233] S. Pamidighantam, R. Puers, K. Baert, and H. A. C. Tilmans, "Pull-in voltage analysis of Electrostatically actuated beam structures with fixed-fixed and fixed-free end conditions", *J. of Micromech. and Microeng.*, p 458-464, 2002.
- [234] Irvine Sensors, MS3110 Universal Capacitive Readout IC. Datasheet (2012)
- [235] M. Bao, "Handbook of Sensors and Actuators, Micro Mechanical Transducers- Pressure Sensors, Accelerometers, and Gyroscopes", *Elsevier*, Amsterdam, 2000.
- [236] H. Nyquist, Thermal agitation of electric charge in conductors, *Phys. Rev.*, vol. 32, pp. 110-113, 1928.
- [237] T. Fritza, M. Griepentrogb, W. Mokwaa and U. Schnakenberga, "Determination of Young's modulus of electroplated Ni", *Electrochimica Acta*, vol. 48, pp. 3029-3035, 2003.
- [238] E.W. Lemmon, R.T. Jacobsen, "Viscosity and thermal conductivity equations for nitrogen, oxygen, argon, and air", *Int. J. Thermophys.*, vol. 25, no. 1, pp. 21-69, 2004.
- [239] Model SR560 low-noise preamplifier, Stanford Research Systems, 2013.

-
- [240] L. A. Rocha, E. Cretu, R. F. Wolffenbuttel, "Analysis and analytical modeling of static pull-in with application to MEMS-based voltage reference and process monitoring," *J. of Microelectromech. Syst.*, vol. 13, no. 2, pp. 342-354, 2004.
- [241] S. Chowdhury, M. Ahmadi and W. C. Miller, "Pull-in voltage study of electrostatically actuated fixed-fixed beams using a VLSI on-chip interconnect capacitance model," *J. of Microelectromechanical Syst.*, vol. 15, no. 3, pp. 639-651, 2006.
- [242] T. Lin, S. Paul, S. Lu and H. Lu, "A study on the performance and reliability of magnetostatic actuated RF MEMS switches," *Microelect. Rel.*, vol. 49, pp. 59-65, 2009.
- [243] S. Kim, Y. Kim, J. Yang, S. Kwon and S. Park, "Degradation level monitoring sensor for insulating oil of power transformer using capacitive high aspect ratio of electrodes," *13th Int. Conf. on Solid-State Sensors, Actuators and Microsyst.*, pp. 613-616, 2005.
- [244] X. Xu, B. Li, Y. and J. Chu, "Design, fabrication and characterization of a bulk-PZT-actuated MEMS deformable mirror," *J. of Micromech. And Microeng.*, vol. 17, pp. 2439-2446, Oct 2007.
- [245] S. R. Vutla, P. K. Patnaik, K. Ramaswamy, S. P. Regalla and M. B. Srinivas, "Effect of particles and contaminants on the static response of a rectangular MEMS diaphragm due to adverse clean room environment — Simulation studies," *IEEE Asia Pacific Conf. on Postgraduate Research in Microelectronics and Electronics (PrimeAsia)*, Visakhapatnam, 2013, pp. 111-113, 2013.
- [246] Y. C. Lee, B. Amir Parviz, J. A. Chiou and Shaochen Chen, "Packaging for microelectromechanical and nanoelectromechanical systems," *IEEE Trans. on Adv. Packag.*, vol. 26, no. 3, pp. 217-226, Aug. 2003.
- [247] S. S. Walwadkar and J. Cho, "Evaluation of die stress in MEMS packaging: experimental and theoretical approaches," *IEEE Trans. on Compon. and Packag. Technol.*, vol. 29, no. 4, pp. 735-742, Dec. 2006.
- [248] F. Giacomozzi, V. Mulloni, S. Colpo, A. Faes, G. Sordo and S. Girardi, "RF-MEMS devices packaging by using quartz caps and epoxy polymer sealing rings," *Symp. on Design, Test, Integr. and Packag. of MEMS/MOEMS*, Barcelona, pp. 1-6, 2013.
- [249] E. S. Topalli, K. Topalli, S. E. Alper, T. Serin and T. Akin, "Pirani vacuum gauges using silicon-on-glass and dissolved-wafer processes for the characterization of MEMS vacuum packaging," *IEEE Sensors J.*, vol. 9, no. 3, pp. 263-270, March 2009.

-
- [250] K. D. Leedy, R. E. Strawser, R. Cortez and J. L. Ebel, "Thin-film encapsulated RF MEMS switches," *J. of Microelectromech. Syst.*, vol. 16, no. 2, pp. 304-309, April 2007
- [251] F. Barriere, A. Crunteanu, A. Bessaudou, A. Pothier, F. Cosset, D. Mardivirin and P. Blondy, "Zero level metal thin film package for RF MEMS," *Topical Meeting on Silicon Monolithic Integr. Circuits in RF Syst. (SiRF)*, New Orleans, LA, pp. 148-151, 2010.
- [252] A. Hilton and D. S. Temple, "Wafer-level vacuum packaging of smart sensors," *Sensors*, vol. 16, no. 11, p. 1819, 2016.
- [253] B. V. Amini and F. Ayazi, "Micro-cavity capacitive silicon on-insulator accelerometers," *J. Micromech. Microeng.*, vol. 15, no. 11, pp. 2113-2120, 2005.
- [254] P. Monajemi and F. Ayazi, "Design optimization and implementation of a microgravity capacitive HARPS accelerometer," *IEEE Sensors J.*, vol. 6, no. 1, pp. 39-46, 2006.
- [255] S. Tez, U. Aykutlu, M. M. Torunbalci and T. Akin, "A bulk-micromachined three-axis capacitive MEMS accelerometer on a single die," *J. of Microelectromech. Syst.*, vol. 24, no. 5, pp. 1264-1274, Oct. 2015.
- [256] Y. Jeong, D. E. Serrano, V. Keesara, W. K. Sung and F. Ayazi, "Wafer-level vacuum-packaged tri-axial accelerometer with nano airgaps," *IEEE MEMS Conf.*, pp. 33-36, 2013.
- [257] T. Aono, K. Suzuki, M. Kanamaru, R. Okada, D. Maeda, M. Hayashi and Y. Isono, "Development of wafer-level packaging technology for simultaneous sealing of accelerometer and gyroscopes under different pressures," *J. of Micromech. and Microeng.*, vol. 26, p. 105007, Aug. 2016.
- [258] H. Ko, S. Park, B. Choi, A. Lee and D. Cho, "Wafer-level hermetic packaged microaccelerometer with fully differential BiCMOS interface circuit," *Sensors and Actuators A Physical*, vol. 137, pp. 25-33, 2007.
- [259] W. Park, R. Candler, V. Ayanoor-Vitikkate, M. Lutz, A. Partridge, G. Yama and T. Kenny, "Fully encapsulated sub-millimeter accelerometers," *IEEE Int. Conf. on Micro Electro Mech. Syst.*, pp. 347-350, 2005.
- [260] S. Amaya, D. V. Dao and S. Sugiyama, "PMMA high sensitive capacitive microaccelerometer fabricated based on hot embossing", *IEEE Sensors Conf.*, pp. 1301-1304, 2012.
- [261] Y. Qin, M. M. R. Howlader, M. J. Deen, Y. M. Haddara, P. R. Selvaganapathy, "Polymer integration for packaging of implantable sensors," *Sensors and Actuators B Chemical*, vol. 202, pp. 758-778, 2014.

-
- [262] B. J. Kim, and E. Meng, "Review of polymer MEMS micromachining," *J. of Micromech. and Microeng.*, vol. 26, p. 013001, 2016.
- [263] I. Comart, K. Topalli, S. Demir and T.Akin, "Microwave characterization of a wafer-level packaging approach for RF MEMS devices using glass frit bonding," *IEEE Sensors J.*, vol. 14, no. 6, pp. 2006-2011, 2014.
- [264] L. Wang, T. Sterken, M. Cauwe, D. Cuypers and J. Vanfleteren, "Fabrication and characterization of flexible ultrathin chip package using photosensitive polyimide," *IEEE Trans. on Compon., Packag. and Manuf. Technol.*, vol. 2, no. 7, pp. 1099-1106, 2012.
- [265] G. Langfelder, A. Caspani, A. Tocchio, S. Zerbini, and A. Longoni, "High-sensitivity differential fringe-field MEMS accelerometers", *Int. Conf. on Solid-State Sensors, Actuators and Microsyst.*, pp. 1823-1826, 2013.
- [266] J. M. Darmanin, I. Grech, J. Micallef, E. Gatt, O. Casha, and A. Briffa, "Design consideration for three-axis MEMS accelerometer using an asymmetric proof mass," *IEEE EUROCON*, pp. 2100-2105, 2013.
- [267] A. Briffa, E. gatt, J. Micallef, I. Grech, O. Casha, and J. M. Darmanin, "Area minimization of a three-axis separate mass capacitive accelerometer using the Thelma process," *IEEE EUROCON*, pp. 2094-2099, 2013.
- [268] H. Bae, S. Arimoto, M. Yoshida and R. Ozawa, "Generation of fingering motions by robotic fingers using morphological characteristics of human thumb," *IEEE/RSJ Int. Conf. on Intell. Robots and Syst.*, pp. 1677-1683, 2005.
- [269] W. N. Sharpe Jr. and A. McAleavey, "Tensile properties of LIGA nickel," *SPIE Conf. on Mater. and Device Characterization in Micromachining*, vol. 3512. pp. 130-137, 1998.
- [270] T. Fritz, H. S. Cho, K. J. Hemker, W. Mokwa and U. Schnakenberg, "Characterization of electroplated nickel," *Microsyst. Technol.*, vol. 9, pp. 87-91, 2002.
- [271] HD-4100 series product bulletin, HD Microsyst. (2009).
- [272] Kapton HN datasheet, Dupont, (2016).
- [273] Z. Suo, E. Y. Ma, H. Gleskova and S. Wagner, "Mechanics of rollable and foldable film-on-foil electronics," *Appl. Phys. Lett.*, vol. 74, no. 8, pp. 1177-1179, 1999.
- [274] F. Gerfers, P. M. Kohlstadt, E. Ginsburg, M. Y. He, D. S. Rubio, Y. Manoli and L. PengWang, "Sputtered AlN Thin Films for Piezoelectric MEMS Devices - FBAR Resonators and Accelerometers," *Solid State Circuits Technol.*, InTech, 2010.

-
- [275] M. Akiyama, T. Kamohara, K. Kano, A. Teshigahara, Y. Takeuchi and N. Kawahara, "Enhancement of Piezoelectric Response in Scandium Aluminum Nitride Alloy Thin Films Prepared by Dual Reactive Cosputtering," *Adv. Mater.*, vol. 21, pp. 593–596, 2009.
- [276] E. Ghafar-Zadeh, G. Ayala-Charca, B. Gholamzadeh, S. Ghasemi and S. Magierowski, "Towards scalable capacitive cantilever arrays for emerging biomedical applications," *Sensor and Actuators A: Phys.*, vol. 260, pp. 90–98, 2017.
- [277] V. A. Kolchuzhin, E. Sheremet, K. Bhattacharya, R. D. Rodriguez, S. D. Paul, J. Mehner, M. Hietschold and D. R.T.Zahnc, "Mechanical properties and applications of custom-built gold AFM cantilevers," *Mechatron.*, vol. 40, pp. 281–286, 2016.
- [278] I. Dufour, F. Josse, S. Heinrich, C. Lucata, C. Ayela, F. Ménil and O. Brand, "Unconventional uses of cantilevers for chemical sensing in gas and liquid environments," *Procedia Eng.*, vol. 5, pp. 1021–1026, 2010.
- [279] M. S. Rayhan, D. P. Butler and Z. Çelik-Butler, "Ultra-thin film piezoelectric AlN cantilevers for flexible MEMS sensors," *IEEE Sensors Conf.*, Busan, pp. 1-4, 2015.
- [280] M. Gillinger, M. Schneider, A. Bittner, P. Nicolay, and U. Schmid, "Impact of annealing temperature on the mechanical and electrical properties of sputtered aluminum nitride thin films," *J. of Appl. Physics*, vol. 117, p. 065303, 2015.
- [281] S. Saravanan, E. Berenschot, G. Krijnen and M. Elwenspoek, "Surface Micromachining Process for the Integration of AlN Piezoelectric Microstructures," *Annual Workshop on Semicon. Adv. for Future Electron.*, pp. 676-681, 2004.
- [282] C. Giordano, I. Ingrosso, M. T. Todaro, G. Maruccio, S. D. Guido, R. Cingolani, A. Passaseo and M. D. Vittorio, "AlN on polysilicon piezoelectric cantilevers for sensors/actuators," *Microelectron. Eng.*, vol. 86, pp. 1204-1207, 2009.
- [283] F. Martin, P. Muralt, M. A. Dubois, and A. Pezous, "Thickness dependence of the properties of highly c-axis textured AlN thin films," *J. of Vacuum Sci. and Technol. A: Vacuum, Surfaces, and Films*, vol. 22, pp. 361-365, 2004.

-
- [284] E. Iborra, J. Olivares, M. Clement, L. Vergara, A. Sanz-Hervás and J. Sangrador, "Piezoelectric properties and residual stress of sputtered AlN thin films for MEMS applications," *Sensors and Actuators A: Physical*, vol. 115, no. 2–3, pp. 501-507, 2004.
- [285] S. Petroni, G. Maruccio, F. Guido, M. Amato, A. Campa, A. Passaseo, M. T. Todaro and M. D. Vittorio, "Flexible piezoelectric cantilevers fabricated on polyimide substrate," *Microelectron. Eng.*, vol. 98, pp. 603–606, 2012.
- [286] Y. Tomimatsu, H. Takahashe, T. Kobayashil, K. Matsumoto, I. Shimoyama, T. Itoh and R. Maeda, "AlN cantilever for differential pressure sensor," *Joint IEEE Int. Symp. on Appl. of Ferroelectric and Workshop on Piezoresponse Force Microscopy*, Prague, pp. 336-339, 2013.
- [287] P. Ivaldi, J. Abergel, M. H. Matheny, L. G. Villanueva, R. B. Karabalin, M. L. Roukes, P. Andreucci, S. Hentz and E. Defay, "50 nm thick AlN film-based piezoelectric cantilevers for gravimetric detection," *J. Micromech. Microeng.*, vol. 21, no. 8, p. 085023, 2011.
- [288] F. L. Hammond, Y. Mengüç and R. J. Wood, "Toward a modular soft sensor-embedded glove for human hand motion and tactile pressure measurement," *IEEE/RSJ Int. Conf. on Intell. Robots and Syst.*, Chicago, IL, pp. 4000-4007, 2014.
- [289] C. Hall, "External pressure at the hand during object handling and work with tools," *Int. J. of Ind. Ergonomics*, vol. 20, no. 3, pp 191-206, 1997.
- [290] A. D. Astin, "Finger force capability: Measurement and prediction using anthropomorphic and myoelectric measures," M.S. thesis, Dept. Ind. Syst. Eng., Virginia Polytechnic Inst. State Univ., Blacksburg, VA, USA, 1999.
- [291] J. C. Doll, B. C. Petzold, B. Ninan, R. Mullanpudi, and B. Pruitt, "Aluminum nitride on titanium for CMOS compatible piezoelectric transducers," *J. Micromech. Microeng.*, vol. 20, p. 025008, 2010.
- [292] D. Low, T. Sumii and M. Swain, "Thermal expansion coefficient of titanium casting," *J. of Oral Rehabilitation*, vol. 28, pp. 239-242, 2001.
- [293] V. V. Felmetgera, P. N. Laptev and R. J. Graham, "Deposition of ultrathin AlN films for high frequency electroacoustic devices," *J. Vac. Sci. Technol. A*, vol. 29, no. 2, p. 021014, 2011.
- [294] M. Akiyama, K. Nagao, N. Ueno, H. Tateyama and T. Yamada, "Influence of metal electrodes on crystal orientation of aluminum nitride thin films," *Vacuum*, vol. 74, no. 3–4, pp. 699-703, 2004.

-
- [295] T. Tsuchiyaa, M. Hiratab and N. Chibab, "Young's modulus, fracture strain, and tensile strength of sputtered titanium thin films," *Thin Solid Films*, vol. 484, no 1–2, pp. 245-250, 2005.
- [296] D. G. Zong, C. W. Ong, M. Aravind, M. P. Tsang, C. L. Choy, D. Lu and D. Ma, "Tensile strength of aluminium nitride films," *Philisophical Mag.*, vol. 84, no. 31, p.3353-3373, 2004.
- [297] S. Khan, M. Shahid, A. Mahmood, A. Shah, I. Ahmed, M. Mehmood, U. Aziz, Q. Raza and M. Alam, "Texture of the nano-crystalline AlN thin films and the growth conditions in DC magnetron sputtering," *Progress in Natural Sci.: Mater. Int.*, vol. 25, pp. 282–290, 2015.
- [298] M. A. Dubois and P. Muralt, "Stress and piezoelectric properties of aluminum nitride thin films deposited onto metal electrodes by pulsed direct current reactive sputtering," *J. of Appl. Physics.* , vol . 89, no. 11, pp. 6389-6395, 2001.
- [299] B. Najafi, K. Aminian, A. Paraschiv-Ionescu, F. Loew, C. J. Bula and P. Robert, "Ambulatory system for human motion analysis using a kinematic sensor: monitoring of daily physical activity in the elderly," *IEEE Trans. on Biomed. Eng.*, vol. 50, no. 6, pp. 711-723, 2003.
- [300] E. W. Weisstein, "Radius of Curvature," MathWorld--A Wolfram Web Resource. <http://mathworld.wolfram.com/RadiusofCurvature.html> [Accessed on Mar 21, 2018].

Biographical information

Md Sohel Mahmood received his B.Sc. in Electrical and Electronic Engineering from Bangladesh University of Engineering and Technology in 2011. He joined the University of Texas at Arlington as a research and teaching assistant in 2013. His primary research focus is bendable MEMS accelerometer fabricated on flexible substrates and encapsulated by flexible superstrate. He has published four conference presentations and two journals. As a recognition of his work, Md Sohel Mahmood received the best paper award in IEEE Sensor Application Symposium (SAS) 2017 and Office of Research Outstanding Poster Presentation award in Annual Celebration of Excellence by Students (ACES) 2017 at University of Texas at Arlington. He is also the receiver of N. M. Stelmakh Outstanding Student Research Award which is given annually to an Electrical Engineering student in recognition of excellence in research demonstrated at the University of Texas at Arlington in 2018.